Forsteritic marble and Mg-Skarn from the Coober Pedy Ridge Subdomain, Gawler Craton, South Australia

Thesis submitted in accordance with the requirements of the University of Adelaide for an Honours Degree in Geology

George Nicholas Symonds

November 2019

FORSTERITIC MARBLE AND MG-SKARN FROM THE COOBER PEDY RIDGE SUBDOMAIN, GAWLER CRATON, SOUTH AUSTRALIA

OBSERVATIONS FROM THE COOBER PEDY RIDGE

ABSTRACT

The Olympic Dam iron oxide-copper-gold province is a world-class copper-gold belt which lies on the eastern margin of the Gawler Craton in South Australia. The Olympic dam province mineralised around ~1590 Ma during the emplacement of voluminous felsic Hiltaba Suite granites and co-genetic mafic Gawler Range Volcanics. Currently, the Cairn Hill deposit in the Mount Woods domain represents the northern extent of the Olympic Dam province. This study examines the geochemistry and age of thermal events at the Mount Brady Prospect, a weakly mineralised copper-bearing sub-economic magnesian skarn system, in the Coober Pedy Ridge domain of the Gawler Craton. Geochronological work completed via LA-ICP-MS U-Pb analyses on apatite and zircon taken from the identified 'coarse-grained' magnesian skarn assemblage and nearby intermediate intrusive rocks are shown to record felsic magmatism at 1584.08 ± 4.97 Ma, regional cooling between ~1450-1400 Ma, and three enigmatic apatite samples which yield ages between 1300 Ma and 1085 Ma. The broad range of ages obtained in this study reveal a complex post-Hiltaba age thermal history in this region of the Gawler Craton. Original drilling records from 1987 identify an olivine-bearing carbonate lithology as being of either carbonatitic or metasedimentary origin. There are numerous occurrences in the northern Gawler Craton that have been provisionally linked with potential carbonatite complexes but no occurrence to date has been confirmed to be of carbonatitic origin. Correct discrimination between carbonatitic lithologies and high-grade marbles is difficult based on mineralogy due to strong mineralogical similarities. LA-ICP-MS analysis of representative mineral phases from the Mount Brady samples show characteristic metamorphic mineral compositions and trace element trends which prove the Mount Brady prospect is not of carbonatitic origin.

KEYWORDS

Mount Brady, Forsteritic-marble, Magnesian-skarn, Carbonatite, Coober Pedy Ridge, Gawler Craton

TABLE OF CONTENTS

LIST OF FIGURES

LIST OF TABLES

1. INTRODUCTION AND BACKGROUND

1.1 MINERAL EXPLORATION IN THE EASTERN GAWLER CRATON

Much of the mineral exploration in the eastern Gawler Craton targets iron-oxide copper gold or 'IOCG' mineralised systems. Iron oxide-copper-gold deposits are of substantial importance due to their potential for hosting large concentrations of base and precious metals. The South Australian Olympic Dam IOCG province is a world-class IOCG belt containing a number of significant deposits including Olympic Dam (10.1 Gt @ 0.78% Cu, 0.25 kg/t U_3O_8, 0.33 g/t Au, and 1 g/t Ag), Carrapateena (79 Mt @ 1.8% Cu, 0.7 g/t Au, and 8.5 g/t Ag), and Prominent Hill (69 Mt @ 1.3% Cu, 0.6 g/t Au, and 3 g/t Ag) (BHP, 2018; Oz Minerals Ltd., 2017-2018). The main mineralising event in the Olympic Dam Province is related to a craton-scale thermal event at ~1590 Ma which led to the emplacement of the Hiltaba Suite granites and co-magmatic Gawler Range Volcanics (Hand, Reid, & Jagodzinski, 2007). This major thermal event is known as the 'Hiltaba Event' and is associated with the timing of mineralisation of South Australia's largest IOCG deposits. As such, areas that were thermally active around the Hiltaba Event are considered highly prospective. However, currently there have been no discoveries of economic Olympic Dam aged IOCG mineralisation north of Cairn Hill in the Mount Woods domain. This study is based on a coincident magnetic and gravitational anomaly within the Coober Pedy Ridge (Figure 1; Figure 2) approximately 40 kilometers north of the Cairn Hill deposit. We examined the geochronology, mineralogy and geochemistry of the dominant mineral phases to identify the origin of an olivine-bearing carbonate and coarse-grained lithology at the Mount Brady prospect, which represent a rare mineral assemblage with multiple models for genesis.

1.2 REGIONAL TECTONOTHERMAL HISTORY

Early thermal events in the Gawler Craton began *ca.* 2560 Ma with distributed arc-like magmatism and basin development (Swain *et al.,* 2005). Early tectonism ceased when the compressional Sleafordian Orogeny initiated (2500-2400 Ma). This event consolidated the Proto-Gawler Craton and is geologically represented by the Sleaford (>2600 Ma) and Mulgathing (2560-2400 Ma) complexes (Tong, Wilson, & Vassallo, 2004; Swain *et al.,* 2005). The Sleafordian orogeny was followed by a four hundred-million-year period of tectonic quiescence (Ferris, Schwarz, & Heithersay*,* 2002). Tectonism restarted *ca.* 1900 Ma, resulting in 400 Ma of episodic granitic magmatism, high-grade regional deformation, and basin development. Deformation related to the Kimban Orogeny (1720-1680 Ma) is recorded on the eastern margin of the Gawler Craton (Dutch, Hand, & Kinny, 2008). At ~1650 Ma an ultra-high temperature (UHT) event was recorded in the Nawa domain of the north eastern Gawler Craton with peak metamorphic conditions of >950°C and >9.5 kbar (Swain *et al.,* 2005). UHT events are uncommon regional events linked to large-scale dynamic tectonic collisional regimes such as orogenies and subduction zones (Cutts, Hand, & Kelsey, 2011). Further UHT events were recorded in the Mabel Creek Ridge (~850°C at 6.5 kbar *ca.* 1600 Ma) and in the Coober Pedy Ridge (~925°C and 6.5 kbar *ca.* 1585 Ma) (Cutts *et al.* 2011; Reid *et al.,* 2014; Kelsey, & Hand, 2014). The younger UHT event is thought to have been long-lived and overlap with the Kararan Orogeny (1570-1540 Ma). Regions affected by the Kararan Orogeny are separated from the main Gawler Craton by the craton-scale Karari Fault Zone. The northern fault zone bifurcates into splays which bind the Coober Pedy subdomain to the north and south (Armit *et al.,* 2017). The presence of major crustal scale fault zones in the Gawler Craton allowed for substantial strain accommodation during the various tectonic regimes. The strain was partitioned into lateral and vertical crustal block translation. Fraser, Reid, and Stern (2012) identify a minimum of four stages of movement along the Karari Fault

Zone, with contrasting sense of movement at different times. The fault system is thought to have developed due to a period of extension *ca.* 1750-1720 Ma and was reactivated during the Kimban Orogeny (1720-1680 Ma). The fault zone was reactivated a second time with a thrust sense of movement between 1580 and 1560 Ma during the Kararan Orogeny. Fault reactivation led to substantial exhumation of the Coober Pedy Ridge and neighbouring Mabel Creek Ridge (Fraser *et al.,* 2012; Figure 1). Forbes *et al.* (2012) suggest that the exhumation of these eastern sub-domains was only made possible following cooling after the Hiltaba Event. The rocks would have experienced a degree of thermal weakening during the high-temperature period. Thus, deformation through the crustal pile would have been accommodated by lateral block translation and crustal thickening. Following post-Hiltaba Event cooling, further deformation was partitioned into existing shear zones, resulting in vertical displacement of 18-35km, which took place due to reactivation of the Karari Fault Zone during the Kararan Orogeny ca. 1570-1540 Ma (Swain *et al.,* 2005; Teasdale, 1997; Hand *et al.,* 2007). The final major episode of movement along the Karari Fault Zone took place around 1450 Ma and was mainly comprised of strike-slip displacement (Fraser *et al.,* 2012). Morrissey, Barovich, Hand, Howard, and Payne (2019) detail a thermal event in the northern Gawler Craton comprised of magmatism and metamorphism at ~1450 Ma. This younger event is associated with peak conditions of 3.2-5.4 kbar at 775-815°C and is interpreted to indicate an extensional regime around that time.

1.3 GEOLOGY OF THE MOUNT BRADY PROSPECT

The Mount Brady prospect is located within the Coober Pedy Ridge (CPR), situated to the north north-east of the Gawler Craton (Figure 1; Figure 2). The CPR is a granulite facies sub-domain. The regional Karari fault system separates the CPR from the northern Nawa domain and Mabel Creek Ridge (MCR), and southern Christie domain and Mount Woods domain (Cutts *et al.,* 2011; Reid *et al.,* 2014). The depth of cover to crystalline basement around the

Mount Brady prospect ranges from ~50 to ~75 meters and consists of intervals of Neoproterozoic to Phanerozoic sedimentary rocks and undifferentiated surficial Cenozoic sediments (Cutts *et al.,* 2011). The crystalline basement in the CPR consists of 1750 – 1730 Ma metasediments (affected by *ca.* 1720-1690 Ma and ~1590 Ma metamorphism), metabasites, and weakly deformed metagabbro lithologies showing emplacement at ~1730 Ma and metamorphism at 1566 ± 9 Ma (Fanning *et al.,* 2007; Hand *et al.,* 2007; Payne, Barovich, & Hand, 2006). Regional granulite facies metamorphism affected the Mount Brady prospect at *ca.* 1600-1580 Ma. It is thought that this event was prolonged with a minimum duration of 19 ± 12 Ma (Cutts *et al.,* 2011). Basement rocks sampled at the Mount Brady prospect consist of heavily altered carbonate rich lithologies, thin intervals (<10m) of felsic to intermediate monzonites and granitoids, and mafic gabbroic intrusives. The geophysical response of the prospect is characterised by a large, circular, reversely polarised mafic body. The reversely polarised mass is surrounded by a variable positive magnetic response with a strong coincident magnetic and gravitational anomaly to the south-west and strong linear magnetic signal to the south (Figure 2). Exploratory drilling intersected two unusual lithologies; a heavily altered marble with a carbonate-phlogopite-olivine/serpentine ± spinel ± pyroxene ± magnetite assemblage; and a coarse-grained magnetite-phlogopite-pyroxene-carbonate ± apatite ± chalcopyrite ± pyrite assemblage. All intersected mineralisation at the Mount Brady prospect is sub-economic. Mineralised areas are part of the coarse assemblage and are characterised by magnetite and trace quantities of late chalcopyrite. The timing of fluid flow, felsic magmatism and hydrothermal alteration is unconstrained at the Mount Brady prospect.

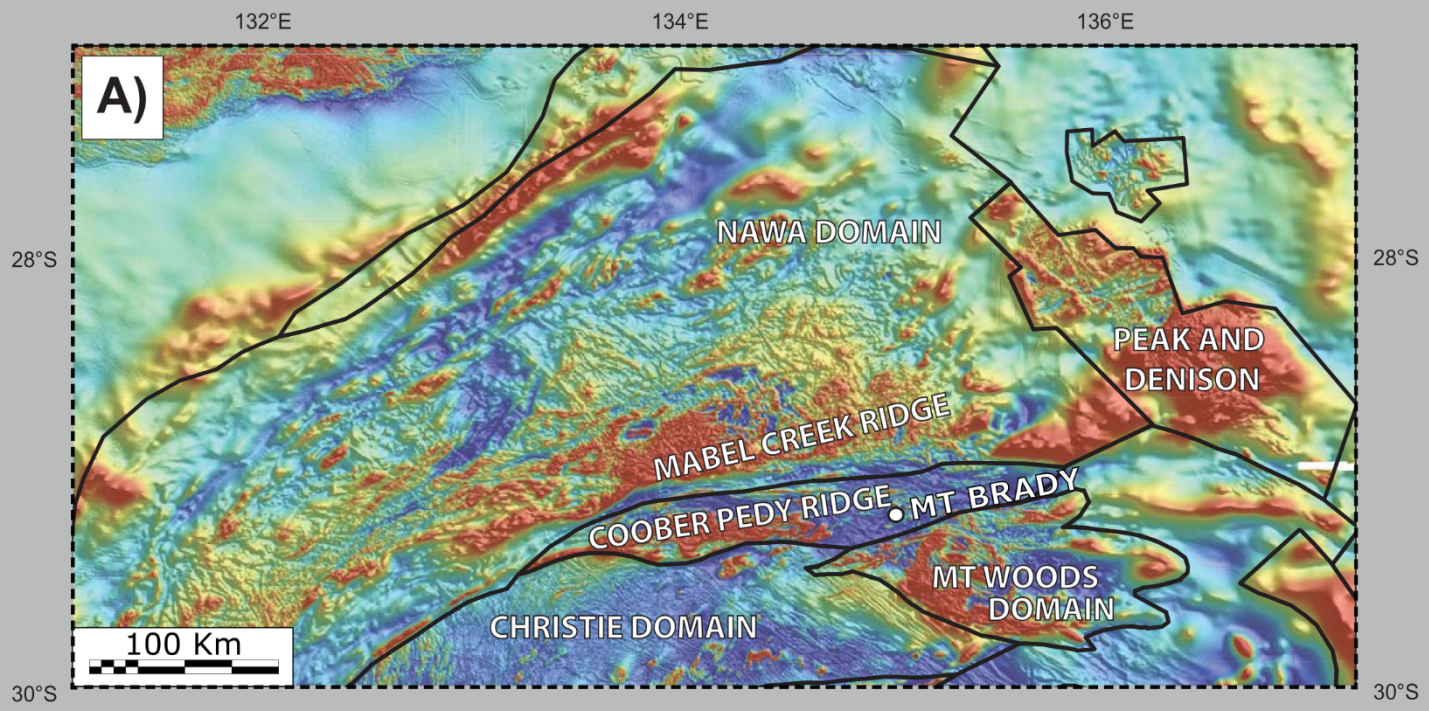

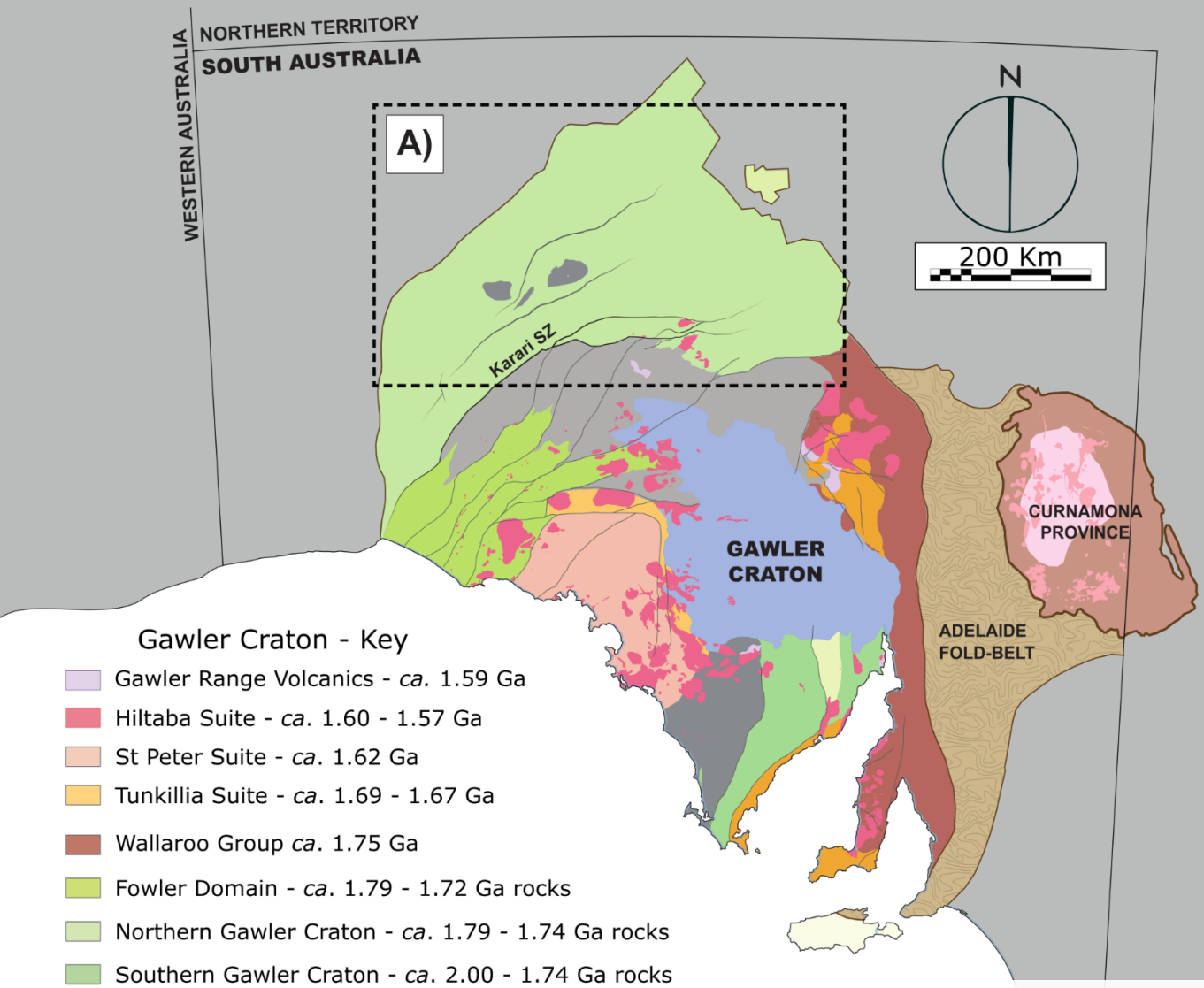

Figure 1: Regional interpreted simplified solid geology of the Gawler Craton after Morrissey *et al.,* (2019) and Reid *et al.,* (2014). **A)** shows the TMI RTP geophysical response of the Northern Gawler Craton with overlaid major domain boundaries and location of the Mount Brady Prospect (further detailed in Figure 2).

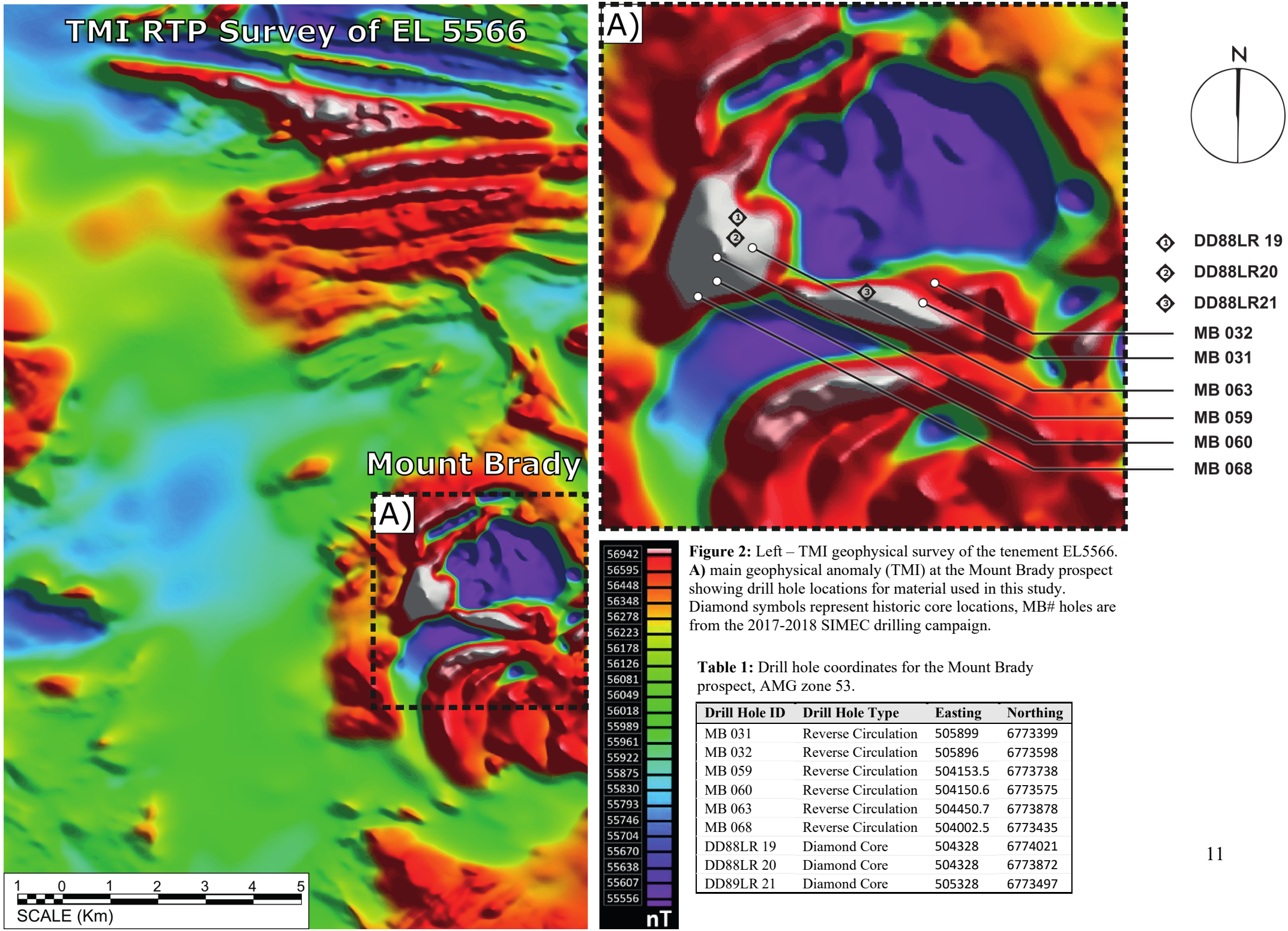

Figure 2: Left – TMI geophysical survey of the tenement EL5566. **A)** main geophysical anomaly (TMI) at the Mount Brady prospect showing drill hole locations for material used in this study. Diamond symbols represent historic core locations, MB# holes are from the 2017-2018 SIMEC drilling campaign.

Table 1: Drill hole coordinates for the Mount Brady prospect, AMG zone 53.

Drill Hole ID	Drill Hole Type	Easting	Northing
MB 031	Reverse Circulation	505899	6773399
MB 032	Reverse Circulation	505896	6773598
MB 059	Reverse Circulation	504153.5	6773738
MB 060	Reverse Circulation	504150.6	6773575
MB 063	Reverse Circulation	504450.7	6773878
MB 068	Reverse Circulation	504002.5	6773435
DD88LR 19	Diamond Core	504328	6774021
DD88LR 20	Diamond Core	504328	6773872
DD89LR 21	Diamond Core	505328	6773497

2. METHODS

2.1 SAMPLING

Samples were obtained from reverse-circulation (RC) drill chips from the Mount Brady RC drilling program (drill hole locations shown in Figure 2). Original sampling procedure combined material into two-meter composite intervals of reverse-circulation (RC) drill chips. The material was classified using a coarse mesh (-5mm) to isolate large fragments of recovered lithologies. Rock chips were hand-picked and subdivided into RC chip trays; aliquots containing identical lithologies were combined to form composite samples of up to six metres. Eight samples from representative rock units were selected for processing into 30µm polished thin sections at Adelaide Petrographics. Taylor (2019) completed a supplementary paragenetic report on nine historic thin sections from the Mount Brady prospect. This report focuses on describing the coarse mineral assemblage of the area (Appendix 3). Four historic diamond drill cores (DD88LR19-20 and DD89LR21-22), from the Mount Brady Prospect were examined at the Tonsley Core Library, two samples of coarse-grained apatite (>5cm) were taken for uranium-lead and trace element analysis. An epoxy grain mount was created for zircons obtained from a single felsic interval for cathodoluminescence imaging and LA-ICP-MS U-Pb analysis. Sample descriptions are reported in Appendix 1.

2.2 PETROGRAPHIC ANALYSIS

Petrographic analysis and mineral identification were carried out at the University of Adelaide on an Olympus BX51 polarising microscope to identify dominant mineral phases and petrographic relationships.

2.2 SCANNING ELECTRON MICROSCOPE AND CATHODOLUMINESCENCE

The FEI Quanta-600 Scanning Electron Microscope (SEM) at Adelaide Microscopy was used to map five thin sections using both electron backscatter (EBS) and mineral liberation analysis (MLA) to locate apatite grains. EBS photomicrographs were taken from two thin sections containing the forsteritic marble assemblage. Finally, zircons were imaged with cathodoluminescence. Instrument parameters for the SEM and cathodoluminescence are presented in Appendix 1.

2.3 LA-ICP-MS

U-Pb zircon and apatite geochronology, and trace element compositions for calcite, phlogopite, magnetite, spinel and olivine were collected by Laser Ablation Inductively Coupled Plasma Mass Spectrometry (LA-ICP-MS) at Adelaide Microscopy, University of Adelaide, Australia. The LA-ICP-MS analyses were carried out on an Agilent 7900x with an attached RESOlution LR 193 nm Excimer laser system. Each geochronological analysis included simultaneous measurements of various trace element suites detailed in Appendix 1. Apatite, calcite, phlogopite, magnetite, spinel and olivine analyses were ablated at a laser frequency of 5 Hz with a fluence of 3.5 J/cm^2. Zircon analyses were ablated with a laser frequency of 5 Hz and a fluence of 2 J/cm^2. Each analysis had a 5-pulse cleaning period to remove surficial contamination followed by a 20 second rest period, 30 second background collection, and 30 second ablation period. Grain targets and sample descriptions, instrument parameters, ablation sequences, and monitored masses are presented in Appendix 1.

2.4 DATA REDUCTION

2.4.1 Geochronology

LA-ICP-MS uranium-lead data was reduced in the program Iolite version 3.0 (Paton, Hellstrom, Paul, Woodhead, & Hergt, 2011) using the VizualAge_UcomPBine data reduction scheme and native Andersen Routine ^{207}Pb correction for apatite, and

U_Pb_Geochron4 DRS for zircon (Petrus and Kramber, 2012; Chew, Petrus, & Kamber, 2014; Paton *et al.,* 2011). Resulting signals were manually bracketed to exclude inclusions, host-rock contamination, and large ^{204}Pb peaks. Data was plotted using IsoplotR (Vermeesch, 2018) on Terra-Wasserburg or Wetherill concordia diagrams. Standard correction was applied using apatite standard MAD (reference age: 473.5 ± 0.7 Ma; Chew *et al.,* 2014), and zircon standard GJ (reference age: 610-590 Ma; Jackson, Pearson, Griffin, & Belousova, 2004) as primary standard material. Data accuracy was monitored using secondary reference standards Plešovice (reference age: 337.27 ± 0.11 Ma; Sláma *et al.,* 2008) and 91500 (reference age: 1061 Ma; Wiedenbeck *et al.,* 1995) for zircon and OD306 (reference age: 1596.7 ± 7.1 Ma; Thompson *et al.,* 2016), and 401 apatite (reference age: 530.3 ± 1.5 Ma; Thompson *et al.,* 2016; Andersen 2002) for apatite analyses. Throughout the analytical sessions zircon standards Plešovice and 91500 demonstrated mean ages of 338.53 ± 0.38 Ma (n = 12, MSWD = 1.5), and 1056.47 ± 1.65 Ma (n = 12, MSWD = 2.1) and apatite standards OD306 and 401 apatite demonstrated mean ages of 1602.81 ± 1.84 Ma (n = 39, MSWD = 1.77) and 527.19 ± 0.84 Ma (n = 63, MSWD = 0.90). Calibration ages fall within allowable error suggesting the geochronology obtained in this study is reliable. For zircon analyses, propagated errors were anomalously high (140-160 Ma) due to low counts of ^{207}Pb in zircons samples and co-measurement of trace element concentrations with U/Pb analyses. U-Pb Analyses are presented in Appendix 5.

2.4.2 Trace Elements

LA-ICP-MS trace element data was processed in Iolite using Trace_Element_X DRS (Paton *et al.,* 2011); the international standard glasses NIST612 and NIST610 were used as primary reference material for elemental concentration calculations and to correct for instrumental drift. Assumptions for internal calibration of individual minerals were made based on ideal mineral stoichiometry (Table 2). Analyses were corrected for different spot sizes and to 100% major oxides for final reporting.

Table 2: Minerals were assumed to possess ideal stoichiometric abundances, elements least likely to have experienced significant matrix substitution were used for internal calibration.

Mineral	Internal Elemental Standard	Concentration (wt%)
Apatite	^{43}Ca	39.36
Zircon	^{91}Zr	43.14
Magnetite	^{57}Fe	72.36
Calcite	^{43}Ca	40.04
Phlogopite	^{39}K	9.33
Olivine	^{28}Si	19.96
Spinel	^{27}Al	37.93

3. RESULTS

3.1 PETROGRAPHIC SUMMARY

Further petrographic details and photomicrographs are included in Appendix 2. A petrographic and paragenetic report of the weakly mineralised coarse-grained assemblage is included in Appendix 3.

3.1.1 MB068 94-104m - Phlogopite-Pyroxene rock

MB068 94-104m consists of a largely monomineralic rock type consisting of >95% phlogopite, the remaining mineralogy consists of magnetite, minor pyroxene, and trace amounts of pyrite (Figure 3.a; 3.b). Phlogopite grain size is typically coarse (400 to >600 µm), but varies between chips, ranging to sub-20µm flakes in some instances. The phlogopite is unoriented and appears to have formed in at least two stages. The early stage is characterised by coarse grain size and pyroxene growth whereas the secondary stage is characterised by small grain size, chloritisation, minor cross-cutting veins, and vuggy infill textures. Veining and vug infill consist of magnetite, carbonate and pyrite. Veins are between 1mm and <50µm. Vugs are small (~1mm) and contain large magnetite grains (<1mm) surrounded by anhedral pyrite (Figure 3.a; 3.b).

3.1.2 Monzonites

Three samples of felsic material (MB063 154-160m, MB031 (1) 74-76m, and M031 70-72m) were examined. Their modal mineralogies are consistent with a monzonite classification.

MB063 154-160m: An altered potassium feldspar and clinopyroxene rich rock with numerous red-grey apatite crystals. Feldspar grains range between 200 and 400µm. Grain boundaries are intergrown and poorly defined. Clinopyroxene is fine grained between ~50µm and ~200µm,

fractured, and pervasively chloritised with poikiloblastic quartz inclusions and poorly preserved grain boundaries. Apatite is present as 50-200µm grains with red-grey colouration. (Figure 3.c; 3.d).

MB031 (1) 74-76m: This sample is comprised of ~50% plagioclase feldspar, 35% potassium feldspar, 10% magnetite, and 5% pyroxene. Feldspars are medium to coarse grained (500 - >2mm) with well-preserved grain boundaries. Pyroxenes are medium to fine grained (<500µm) and are often in contact with magnetite spots. Magnetite alteration is pervasive as disseminated anhedral masses, often with feldspar or pyroxene inclusions. Euhedral, typically unfractured and inclusion free apatite grains in this sample range from ~20 to >200 µm. This rock does not record deformation. (Figure 3.g; 3.h).

M031 70-72m: A fine grained heavily altered felsic rock containing plagioclase, potassium feldspar, biotite, and minor apatite. Potassium feldspar and plagioclase are approximately equigranular and exhibit poorly preserved grain boundaries and strongly perthitic textures. Quartz is present as poikiloblastic inclusions in heavily chloritised and altered pyroxene grains. Biotite is present as rare lathes growing without orientation. There are numerous apatite grains between ~50 and 400µm. Apatite is euhedral and only rarely fractured. A single late-stage carbonate vein (~50µm wide) is observed in this sample. Figure 3.i; 3.j)

3.1.3 MB032 64-74m - Gabbro

A gabbro with variable grain size from coarse (>2mm) to very fine (<50µm). Approximately equal concentrations of plagioclase and pyroxene are visible. Grain boundaries and minerals are well preserved. Magnetite is present as pervasive disseminated spots. This lithology is crosscut by narrow late stage carbonate veins (~10-50µm wide). No deformation is recorded in this lithology. (Figure 3.e; 3.f).

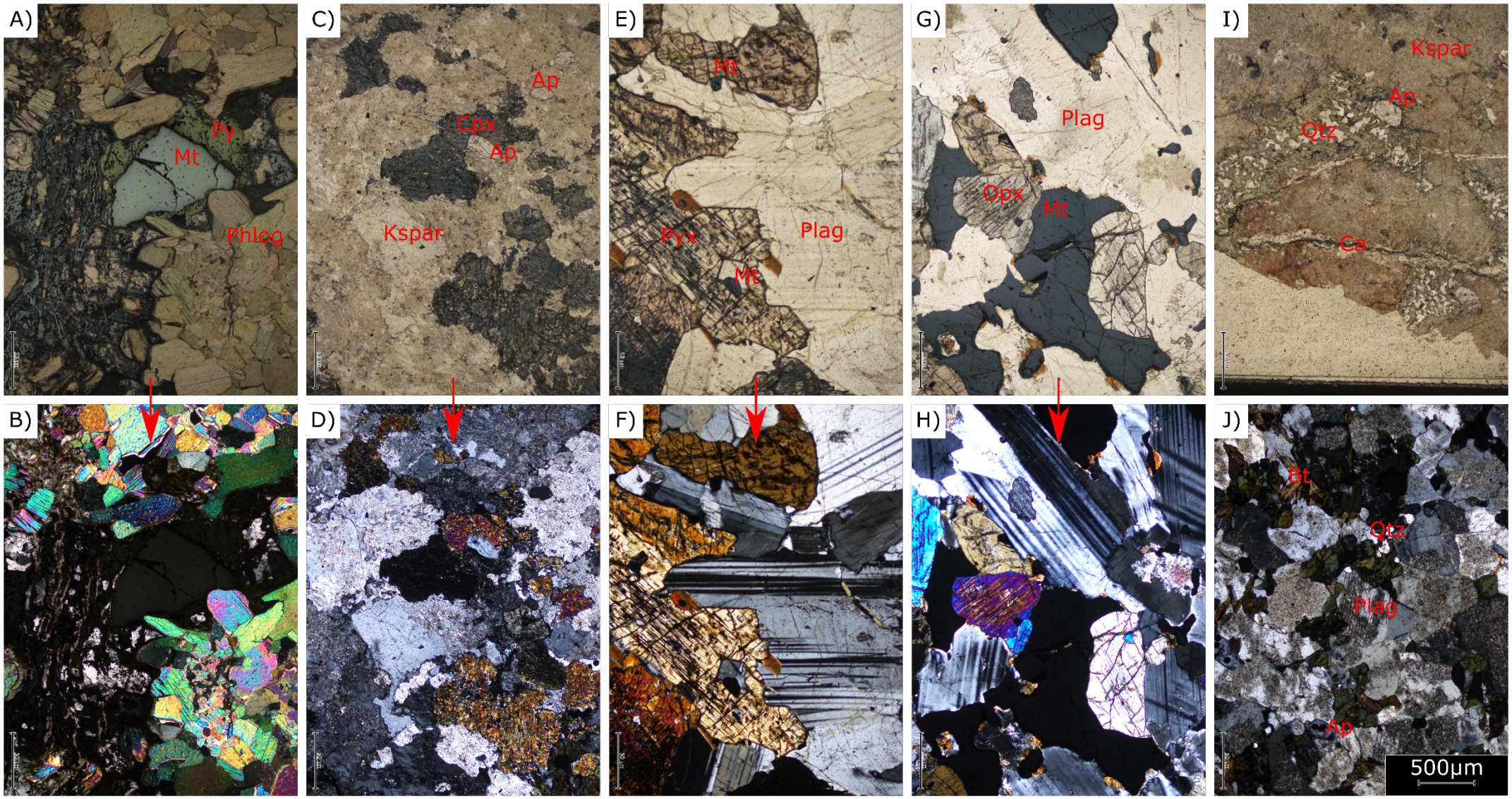

Figure 3: Photomicrographs of selected igneous lithologies. **(A, B)** MB068 94-104m showing a late magnetite vein with a coarse magnetite grain surrounded by pyrite, the rock matrix is mainly phlogopite with minor pyroxenes. **(C, D)** MB063 154-160m showing an altered kspar and pyroxene rock. **(E, F)** MB032 64-74m showing a coarse-grained gabbro with magnetite alteration spotting. **(G, H)** MB031 (1) 74-76m showing a monzonite with magnetite spotting. **(I, J)** MB031 70-72m showing an altered monzonite with large apatite crystals and a cross-cutting carbonate vein.

3.1.6 DD88LR 20 165.2 m – Coarse Magnetite-Phlogopite-Carbonate Assemblage

There are two main distinct mineral assemblages at the Mount Brady prospect, a coarse-grained lithology represented by an assemblage bearing pyroxene, magnetite, phlogopite, chalcopyrite, pyrite, apatite, and carbonate, and a lithology bearing forsterite, spinel, phlogopite and carbonate – a forsteritic marble. Neither assemblage records deformation. Copper mineralisation in the Mount Brady area is concentrated in the coarse-grained assemblage and is represented by small quantities of chalcopyrite, the only copper-bearing mineral identified in this system (e.g. Figure 4). Appendix 3 includes a supplementary paragenetic report and detailed petrological examination of the coarse-grained assemblage (Taylor 2019).

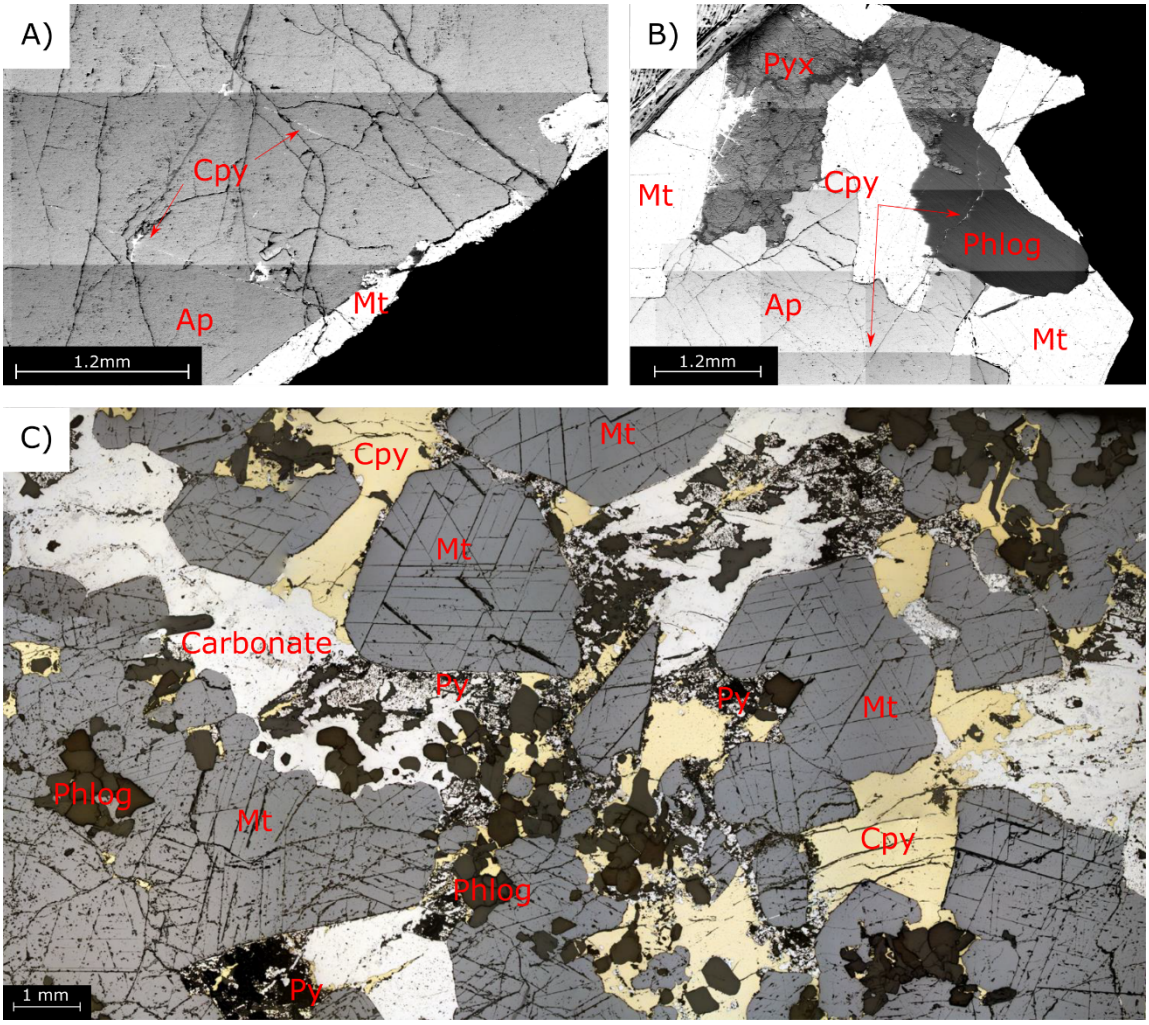

Figure 4: A; B) EBS images of macroscopic apatite fragments taken from the coarse assemblage (sample DD88LR20-1) showing the cross-cutting relationship of minor late chalcopyrite. **C)** plane polarised light image from thin section DD88LR20 165.2m showing the late stage growth of chalcopyrite around earlier magnetite and phlogopite. Py = pyrite, Cpy = chalcopyrite, Ap = apatite, Phlog = phlogopite, Mt = magnetite.

3.1.7 Forsteritic Marble assemblage

The forsteritic marble assemblage was sampled in three locations: MB059 110-112m, MB060 214-216m, and MB068 126-136m. Modal mineralogical compositions of samples varied both between sample interval and between chips from the same sample. Modal compositions for each sample are presented in Table 3.

Table 3: Modal compositions of marble samples, some sample intervals had chips of significantly different compositions.

Modal Compositions of Marble Samples							
Sample	**Carbonate**	**Phlogopite**	**Serpentine**	**Olivine**	**Spinel**	**Opaque**	**Pyroxene**
MB059 110-112	60	0	35	< 1	5	< 1	0
MB060 214-216	60	30	10	0	< 1	< 1	0
	60	0	38	< 1	2	< 1	0
	40	0	30	20	8	2	0
MB068 126-136	60	0	38	< 1	2	< 1	0
	40	30	0	0	< 1	< 1	30
	60	40	0	0	0	< 1	0

MB059 110-112m: This sample is comprised of five RC chips (Figure 5.a); all chips have the same mineralogy of calcite-serpentine-spinel-opaque minerals ± minor relict olivine. The calcite is coarse grained with strong crystal boundaries. Where it contacts olivine a reaction halo is formed. This is ubiquitous throughout this sample. Oval inclusions of calcite exist within serpentine grains. The serpentinised grains are rounded and preserve no relict euhedral crystal shapes. Many serpentinised grains contain minor disseminations of an opaque mineral. Serpentinised grains have two different textures, a characteristic ‘hour-glass’ pattern of serpentine minerals (e.g. Figure 5.b) and a darker rough texture with no defined internal structure (e.g. Figure 5.c). Spinel grains are rounded and fragmented but exsolved opaques retain relict euhedral rims. The spinel occurs as a green-brown phase with both rounded and euhedral form; it frequently occurs in proximity to serpentinised grains and is frequently fragmented.

MB060 214-216m: This sample is comprised of nine small RC chips (Figure 6.a). Most have a similar general mineralogy of carbonate, phlogopite, serpentine, spinel, olivine ± opaque minerals. The carbonate comprises the main groundmass of this thin section. It is coarsely crystalline and is commonly embayed by other carbonate crystals. Calcite shows minor exsolution of dolomite in phlogopite poor chips; the dolomite exsolves along crystal interstices. Carbonates are included as oval blebs within both serpentinised grains and phlogopite. Phlogopite forms as numerous non-oriented tabular phenocrysts and is occasionally included within serpentinised grains as small inclusions. Spinel grains in this sample are generally fragmented and colourless (e.g. Figure 6.c). Olivine occurs rarely as remnants within some serpentinised grains. Opaque minerals form in contact with both serpentinised grains and many spinel grains but also form discontinuous narrow stringers <10μm wide.

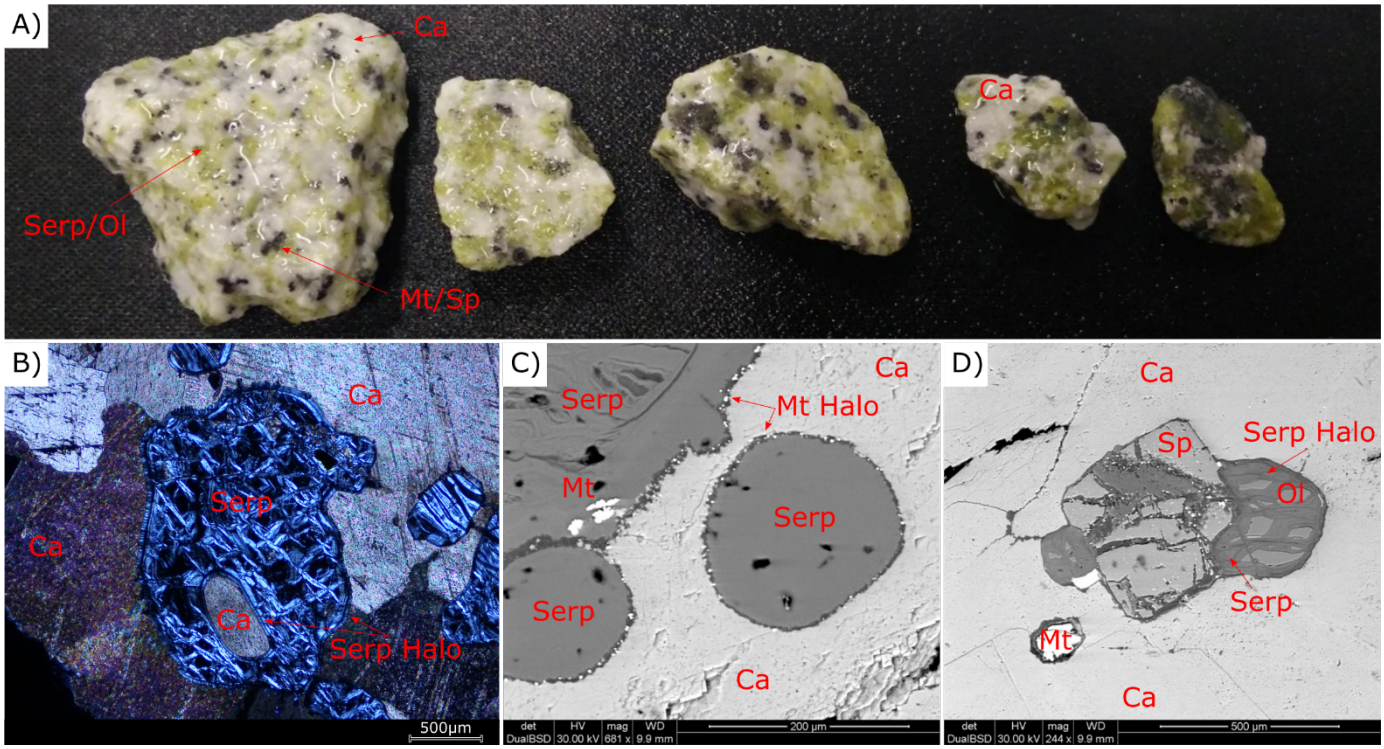

Figure 5: MB059 110-112m A) Hand sample rock chips from the forsteritic marble assemblage. **B)** Photomicrograph under crossed-nicols showing a rounded calcite inclusion within a serpentinised grain with 'hourglass' serpentine texture. **C)** An EBS image of a serpentinised grain showing no internal texture and a rim exsolving specks of magnetite. **D)** An EBS image of a fractured euhedral spinel grain set in a calcite matrix. The spinel is in contact with magnetite and two serpentinised grains containing relict olivine. The darker material within the spinel grain is an unidentified mineral phase. Ca = Carbonate, Serp = Serpentinised material, Ol = Olivine, Sp = Spinel, Mt = Magnetite

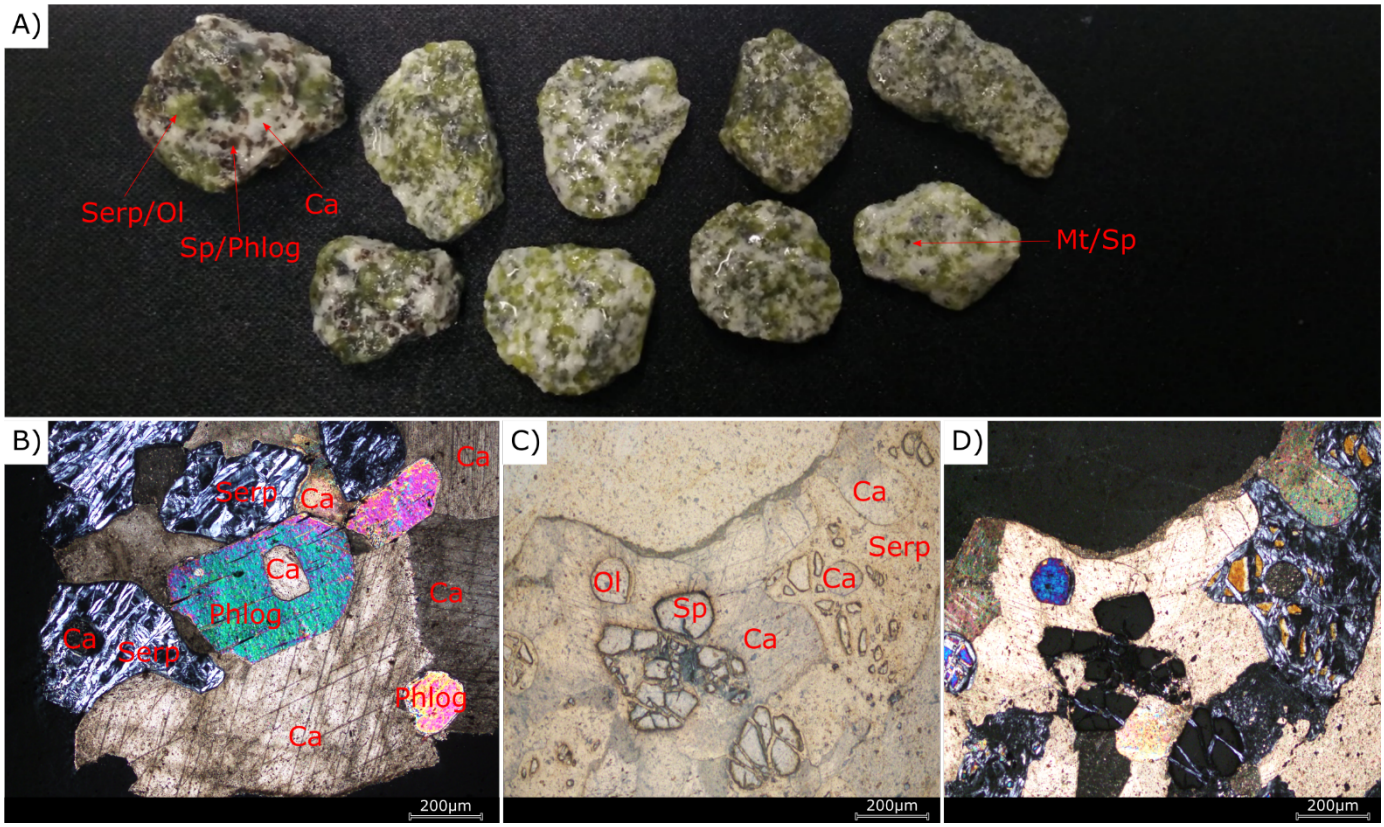

Figure 6: MB060 214-216m A) Hand sample rock chips from the forsteritic marble assemblage. **B)** photomicrograph under crossed-nicols showing forsteritic marble with serpentinised grains and phlogopite sheets with calcite inclusions. **C-D)** photomicrographs under plane polarised **(C)** and crossed nicols **(D)** showing spinel, olivine, serpentine and carbonates from the forsteritic marble. Ca = Carbonate, Serp = Serpentinised material, Ol = Olivine, Sp = Spinel, Mt = Magnetite, Phlog = Phlogopite.

MB068 126-136m: Three large RC chips from a marble lithology, two of the chips have the same mineralogy of calcite, serpentine, phlogopite, spinel ± opaques, one chip additionally contains pyroxenes. The calcite is coarsely crystalline and shows pressure twinning in most areas; calcite between serpentinised grains often shows a gritty surficial texture and the destruction of twinning. Serpentinised grains contain substantially higher quantities of opaque minerals compared to other samples of similar lithologies and the opaque minerals are concentrated in the areas with stronger alteration. The serpentinised grains often include carbonate blebs and show evidence of replacement by phlogopite (Figure 7.b; 7.c). Spinel is blue-green, generally fragmented and subhedral. Another chip has no serpentinised grains but contains pyroxene, phlogopite, and calcite. The pyroxene grains are generally euhedral or subhedral and often heavily fragmented with fracture infill of carbonate and phlogopite (e.g. Figure 7.d).

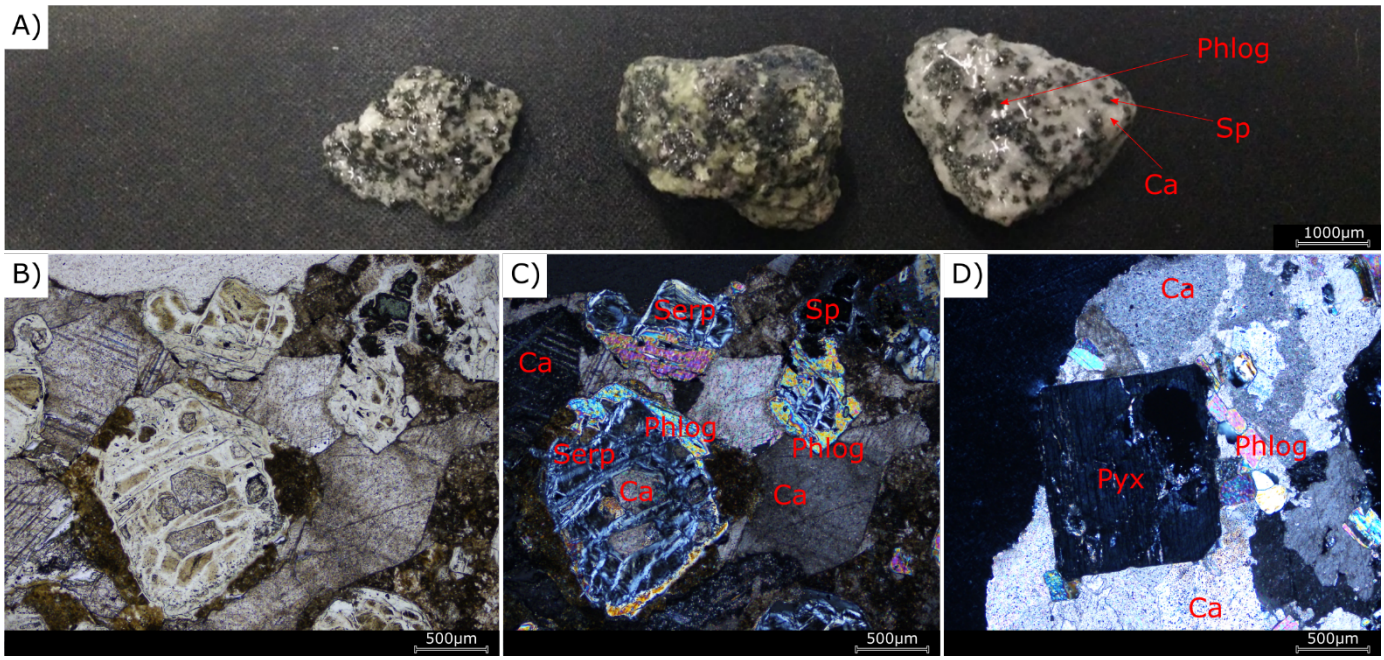

Figure 7: MB068 126-136m A) Hand sample rock chips from the forsteritic marble assemblage. **B-C)** Photomicrographs under plane polarised light **(A)** and crossed nicols **(B)** showing inclusions of calcite within a serpentinised grain which is rimmed by phlogopite. **C)** Photomicrograph under crossed-nicols showing a euhedral basal section of a pyroxene phenocryst sitting in a calcite and phlogopite matrix. **D)** hand samples of this lithology. Ca = Carbonate, Sp = Spinel, Phlog = Phlogopite, Pyx = Pyroxene.

3.2 TRACE ELEMENT DISTRIBUTION

Full analytical results presented in Appendix 4. All mineral analyses were recalculated to 100% major oxides (e.g. Traversa *et al.,* 2001).

3.2.1 Carbonates

Fifty-two analytical points were obtained from calcite in both the coarse-grained system and various intervals of forsteritic marble. Twelve spots were placed on dolomite in the forsteritic marble assemblage, no dolomite was identified in the coarse-grained assemblage. Trace element distributions are presented in Figure 8. All carbonate analyses contained negligible rare earth concentrations. Distinct negative europium anomalies were identified in all forsteritic-marble carbonates. The coarse-grained assemblage shows a broad compositional range with preferential light-rare-earth-element (LREE) enrichment and little to no europium anomaly. Calcite and dolomite show similar trace element patterns with weakly diverging heavy-rare-earth (HREE) compositions. MB068 shows similarities between calcite and dolomite only in the middle-rare-earth elements (MREE; Sm-Gd) with relative enrichment of both LREE and HREE in the dolomite compared to the calcite in the same sample, a pattern not observed in the other forsteritic marble containing dolomite (MB 059).

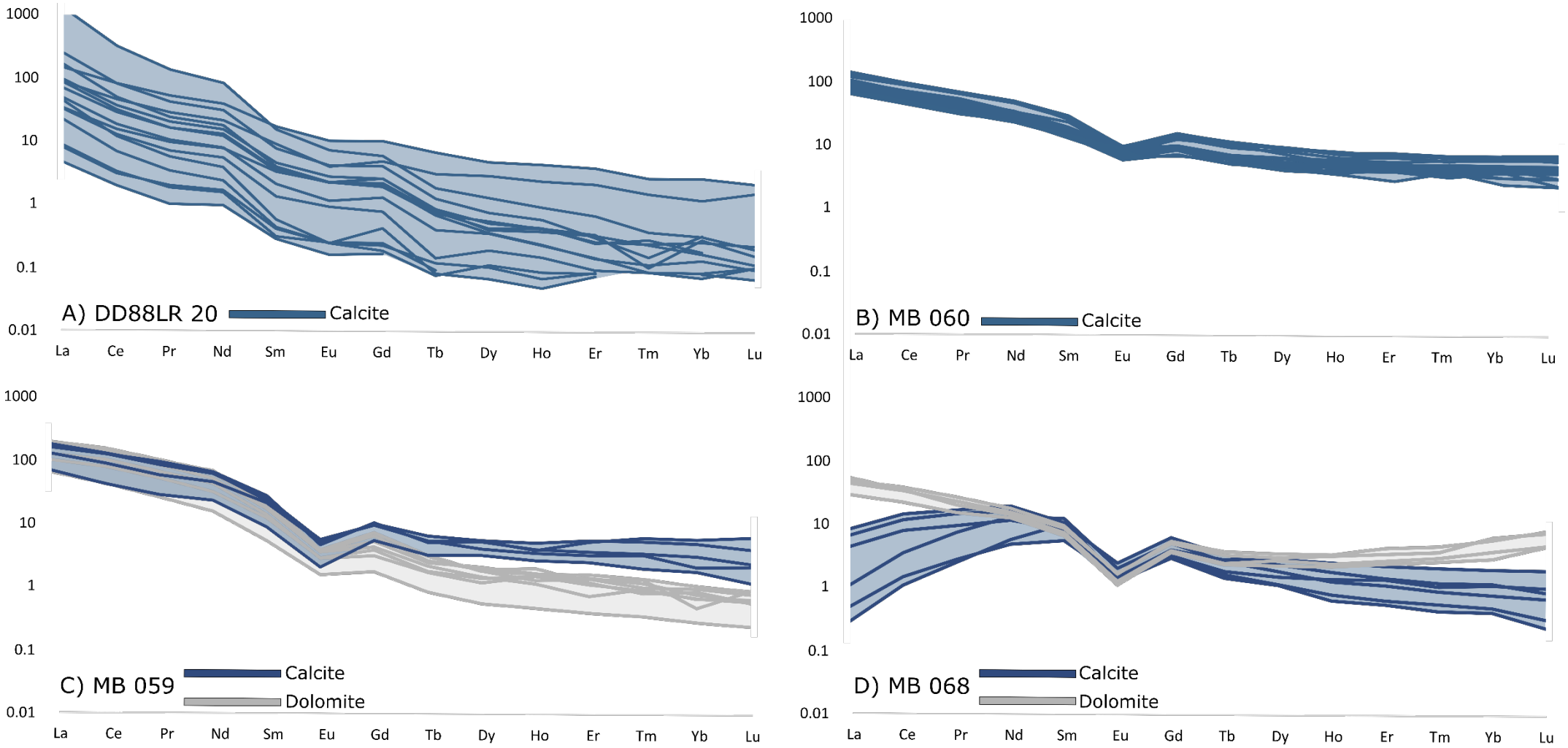

Figure 8: Trace elements in analysed carbonates, **6.A)** shows the coarse-grain assemblage calcite with a wide compositional variation. **6.B)**, **6.C)**, and **6.D)** show the variation in trace element partitioning in carbonates between similar forsteritic marble assemblages. Chondrite values from McDonough & Sun (1995).

3.2.2 Micas

Thirty-one analyses were obtained from micas in both the coarse-grained assemblage (n = 13) and the forsteritic marble (n=18). The analysed mica shows only minor variation in composition between the forsteritic marble assemblage and the coarse-grained assemblage and is classified as phlogopite (Figure 9). Analyses from the coarse-grained assemblage plot along the phlogopite-annite trend, comparatively, the phlogopite from the forsteritic marbles show slight Al enrichment which is similar across marble samples.

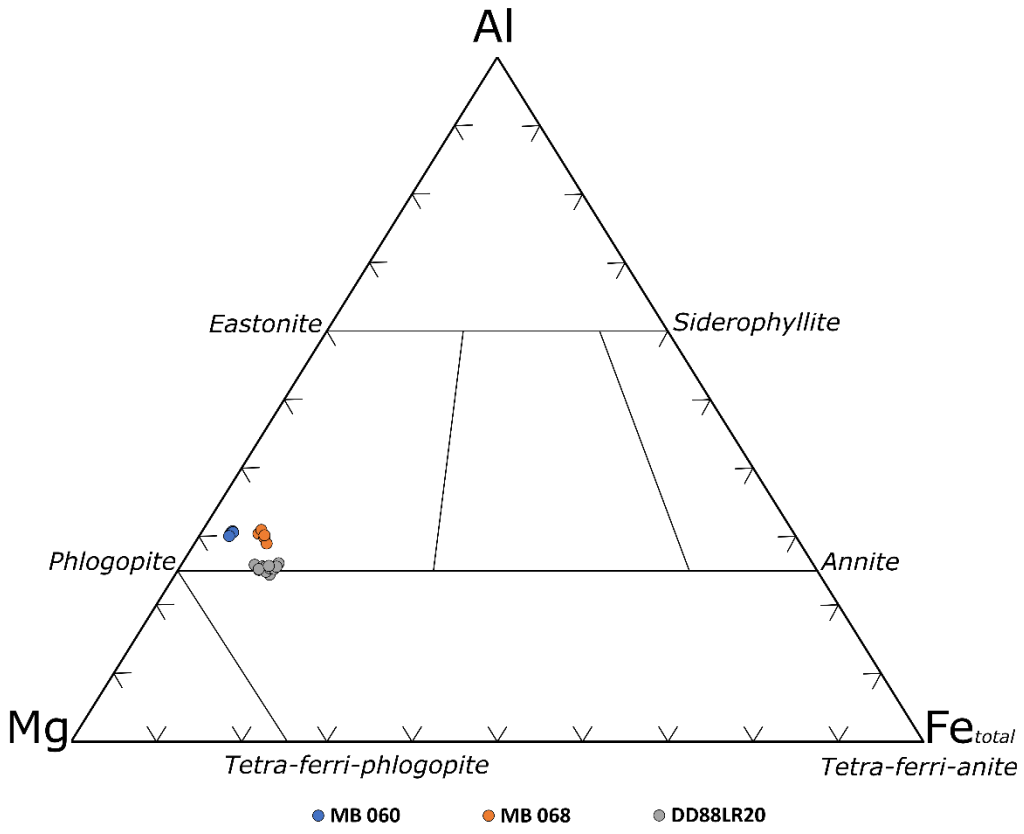

Figure 9: Mg-rich mica discrimination diagram (Brod et al., 2001). Showing the compositional variation between the analysed phlogopite from the coarse-grained assemblage and forsteritic-marble plotted on a ternary diagram. The coarse-grained assemblage phlogopite

3.2.3 Apatite

Trace element concentrations for apatite were collected simultaneously with geochronological measurements. 358 analyses were obtained from apatites contained within igneous lithologies and 183 analyses were gathered from macroscopic apatite crystals from the coarse-grained assemblage. Apatite trace element geochemistry diagrams (Figure 10) show similar rare earth patterns between all samples. Igneous samples are relatively enriched in all trace elements compared to the coarse-grained assemblage apatite. All samples show preferential LREE enrichment over HREE and a distinct negative Eu anomaly (Figure 10). No apatite was identified in the forsteritic marble assemblages.

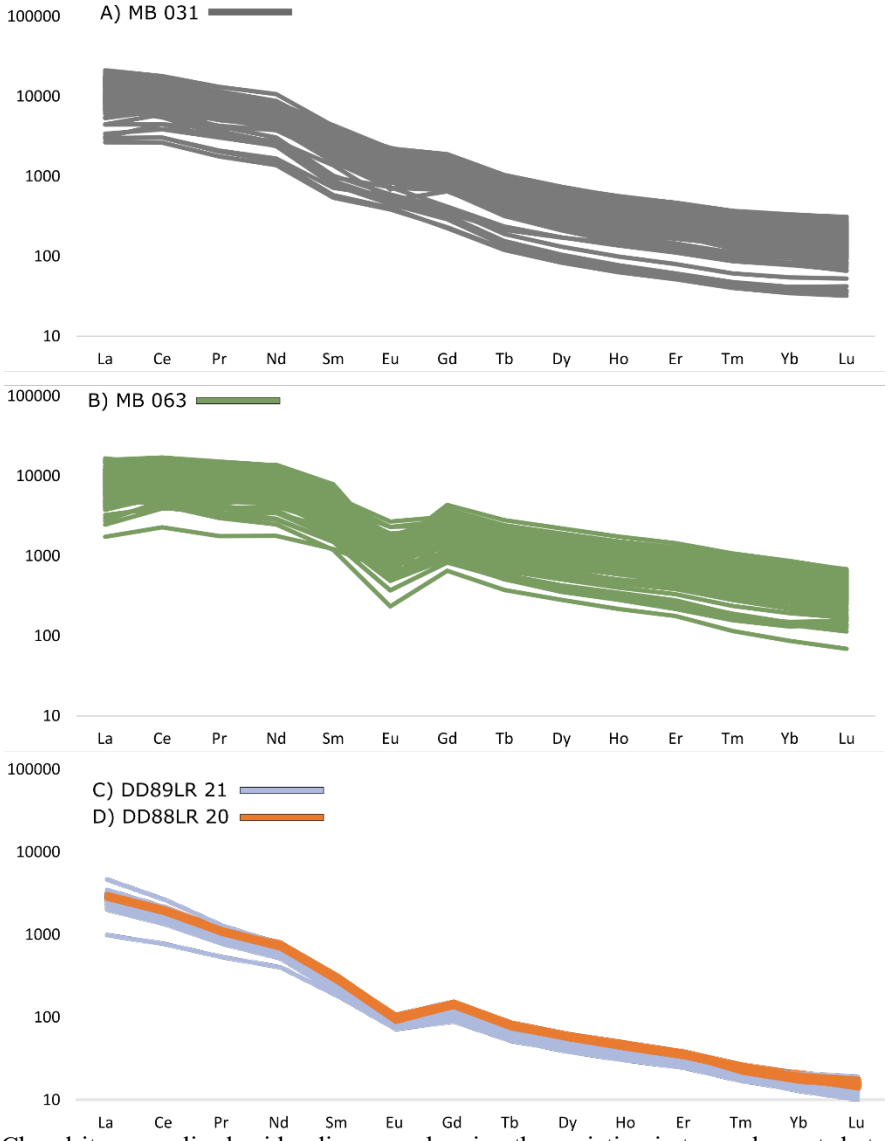

Figure 10: Chondrite normalised spider diagrams showing the variation in trace elements between apatite analyses from samples within an igneous host **(A; B)** and apatite from the coarse-grained assemblage **(C; D)**. Chondrite values from McDonough & Sun (1995).

3.2.4 Spinel and Olivine

Seven olivine and thirty-four spinel trace and major element analyses were obtained from two forsteritic marble units. Nickel and chromium concentrations are low in both olivine (< 13 ppm Ni, and < 7ppm Cr) and spinel (< 28 ppm Ni, and < 470 ppm Cr). Both spinel and olivine show compositional differences between similar lithologies. Summarised geochemical data for olivine analyses are presented in Table 4.

Table 4: Summarised geochemical characteristics of olivine from the two sampled forsteritic marble assemblages. Small grains and serpentinisation limited the number of available analyses.

Olivine	MB 059 – 110m - 112m				MB 060 – 214m - 216m			
	Min	Mean (3)	Max	Std.	Min	Mean (4)	Max	Std.
Si, %	35.3	36.4	37.5	1.1	35.6	36.1	36.5	0.3
Mg, %	60.4	61.6	62.9	1.3	59.6	61.0	61.5	0.4
Fe, %	1.3	1.5	1.6	0.1	2.7	2.9	3.6	0.2
Al, ppm	2,523.2	4,661.3	6,882.3	2,180.7	40.5	183.0	1,757.7	436.3
K, ppm	-	7.8	23.4	13.5	-	-	-	-
Ca, ppm	-	122.4	194.6	106.6	-	87.9	226.1	99.4
Ti, ppm	128.4	232.0	314.1	94.7	130.0	197.0	242.1	29.3
V, ppm	0.6	0.9	1.0	0.2	0.6	1.1	1.7	0.3
Cr, ppm	2.5	4.2	6.4	2.0	-	0.5	2.8	0.8
Mn, ppm	385.1	433.1	466.2	42.5	589.9	641.2	826.4	54.7
Ni, ppm	10.4	11.8	13.4	1.5	9.4	10.4	11.5	0.6
Sr, ppm	0.1	0.1	0.2	0.1	-	-	-	-
Zr, ppm	0.2	0.2	0.3	0.0	0.1	0.8	1.3	0.3
Nb, ppm	-	-	-	-	-	0.1	0.5	0.1
Ba, ppm	-	0.1	0.2	0.1	-	-	-	-

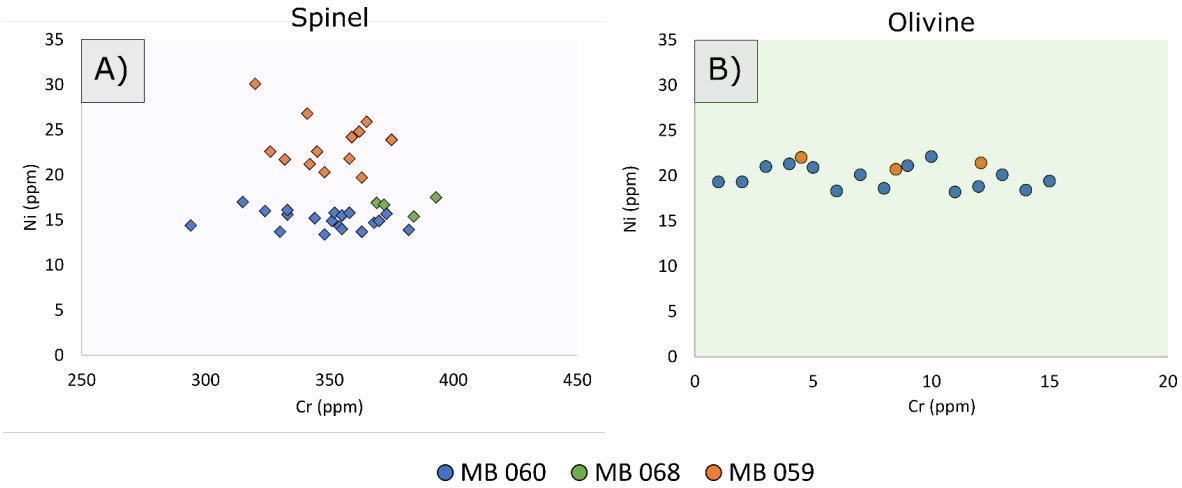

Figure 11: Bivariate plots showing variation in concentration between Ni and Cr in spinel (A) and olivine (B) analyses. Spinel was present and analysed in three samples (MB 060, MB 068, and MB 059) whereas olivine was only present in two samples (MB 060).

3.2.5 Magnetite

Two geochemically distinct textures of magnetite were identified in the coarse-grained assemblage; macroscopic euhedral grains, and anhedral masses intergrown with sulphides (pyrite with minor chalcopyrite – e.g. Figure 4.c). Magnetite is only a small component in the forsteritic marble and takes the form of either individual grains (<200µm), narrow stringer style veins (<30µm) or exsolution from serpentinised grains, spinel, or phlogopite. The magnetite analyses from the forsteritic marble show stronger grouping with the macroscopic euhedral magnetite analyses in the coarse-grained assemblage than the intergrown magnetite-pyrite-chalcopyrite in the same assemblage (Figure 12; Figure 13).

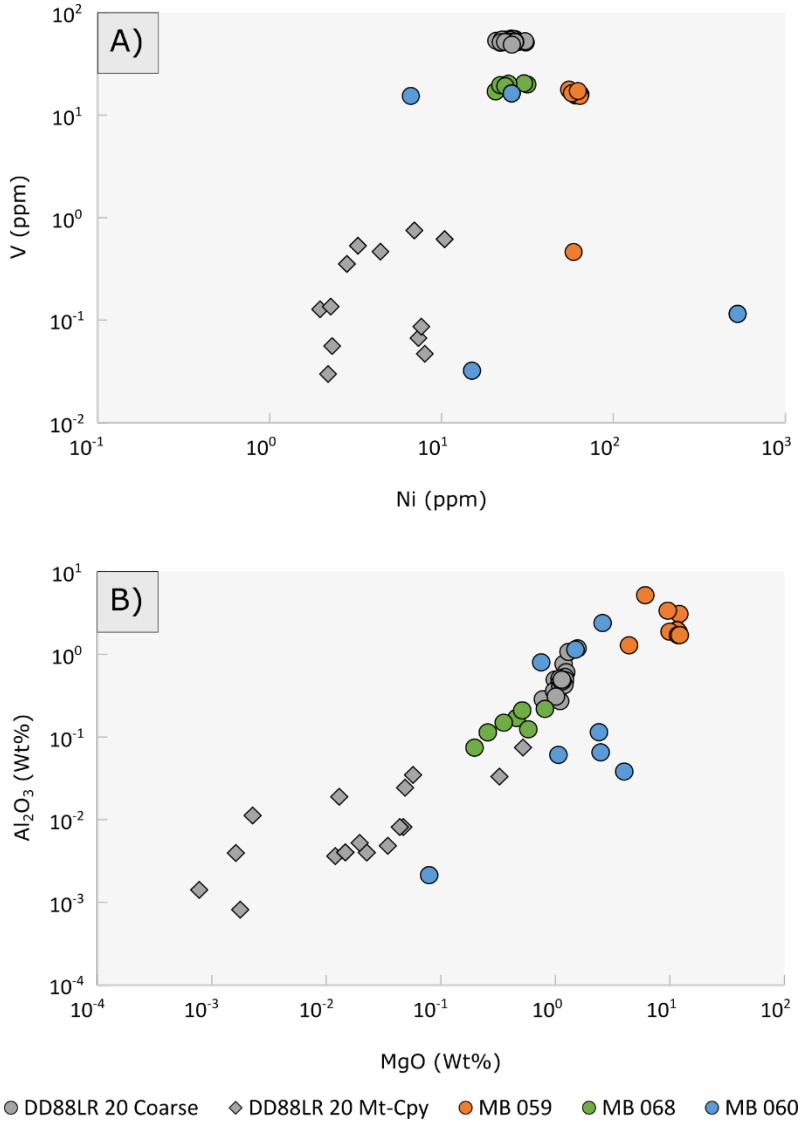

Figure 12: Bivariate plots for magnetite analyses showing geochemical variation between two distinct magnetite generations in the coarse-grained assemblage and magnetite in three forsteritic marble samples.

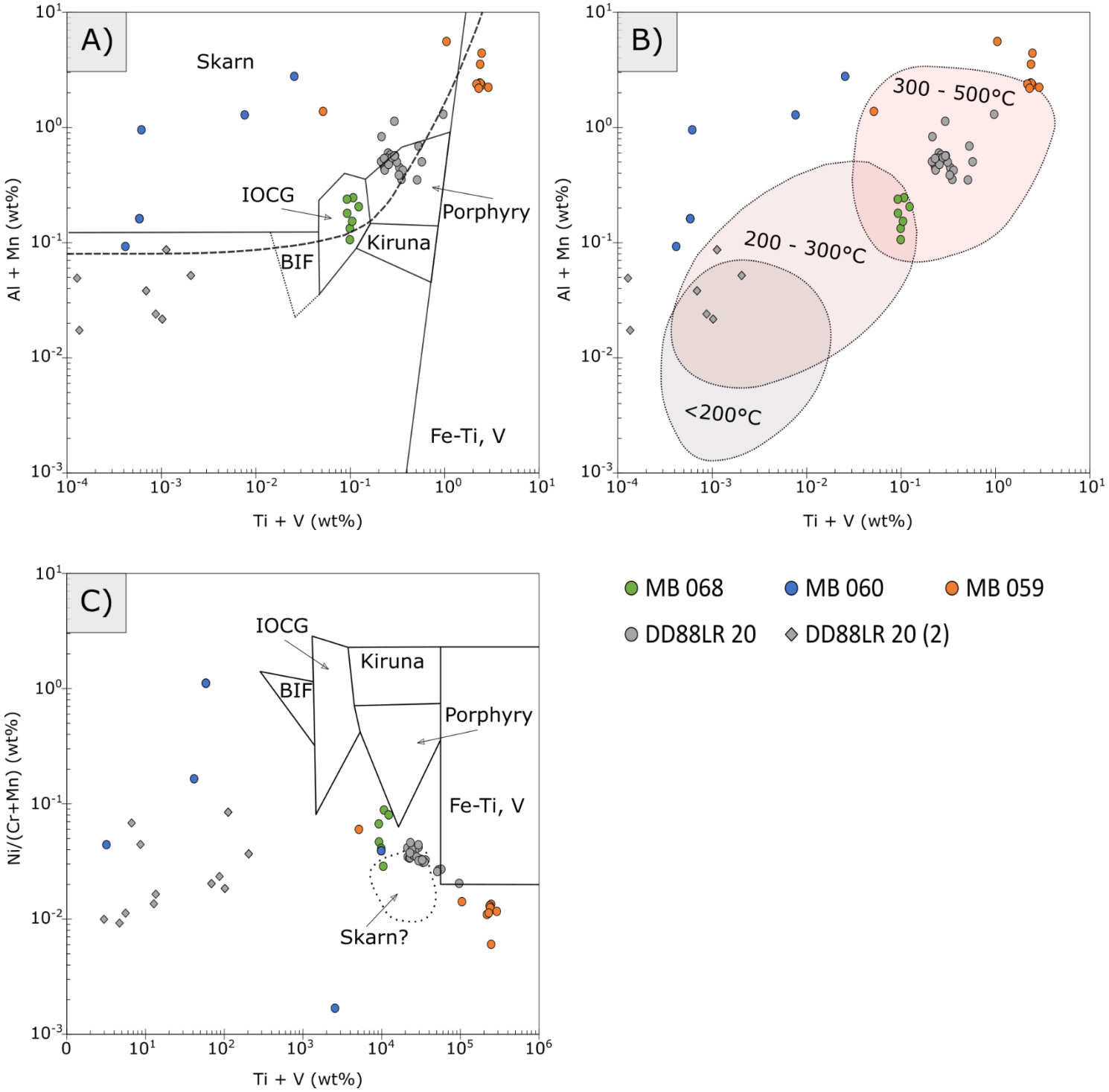

Figure 13: Bivariate plots for magnetite discrimination from Nadoll *et al.* (2014), temperature fields in **B** adapted from Zhou, Tang, and Chen (2017). Comparison of **(A)** and **(C)** shows that the analyses plot outside of IOCG, porphyry, BIF, and (Fe-Ti, V) deposit styles. The analyses plot close to, or within, the new skarn border (dashed line in A; skarn field in C) proposed by Nadoll *et al.* (2014).

3.3 GEOCHRONOLOGY

3.3.1 Apatite Geochronology

MLA mapping of two igneous lithologies (MB031 70-72m, MB063 154-160m) in thin section located numerous euhedral apatite grains between 20 and 400µm, from which, 409 apatite geochronological and trace element measurements were obtained. Fragments of two macroscopic apatite crystals (>> 2cm) from the coarse-grained assemblage (DD89LR 21 203.75m and DD88LR 20 188m) provided a further 183 data points. The apatite fragments from the coarse assemblage are largely homogeneous, however minor inclusions of monazite (<5µm) are present in the sample from DD89LR 21, and late stage chalcopyrite crosscuts the apatite as small discontinuous stringers in the sample from DD88LR 20. The age from the apatite around the monazite inclusions was not resolvable. Table 6 summarises the resulting ages from apatite geochronology obtained in this project.

Table 5: Summary of results for apatite geochronology. Full results plotted on Figure 14, supplementary data in Appendix 5. N = number of spots used in the final age calculation, MSWD = mean square weighted deviation, (g) = gridded analyses on matrix apatite, (s) = analyses near cross-cutting sulphides, (m) = analyses near monazite inclusions. Entries in red indicate statistically unsuitable MSWD values for the number of analyses in that sample (Spencer, Kirkland, & Taylor, 2016).

Sample	N (total)	Age (discordia)	MSWD
MB 031 70m-72m	214 (214)	1437.48 ± 6.85 Ma	0.71
MB 063 C1	41(41)	1457.90 ± 21.7 Ma	0.41
MB 063 C2	19 (19)	1411.40 ± 69.9 Ma	0.66
MB 063 C3	17 (17)	1261.10 ± 12.60 Ma	1.10
MB 063 C4	0 (16)	1435.6 ± 16.3 Ma	1.90
MB 063 C5	53 (53)	1458.51 ± 8.65 Ma	0.89
DD88LR 20 (g)	96 (96)	1300.3 ± 10.40 Ma	1.20
DD88LR 20 (s)	20 (20)	1282.8 ± 33.70 Ma	0.65
DD89LR 21 (g)	31 (31)	1085.0 ± 16.10 Ma	1.40
DD89LR 21 (m)	0 (27)	-	16

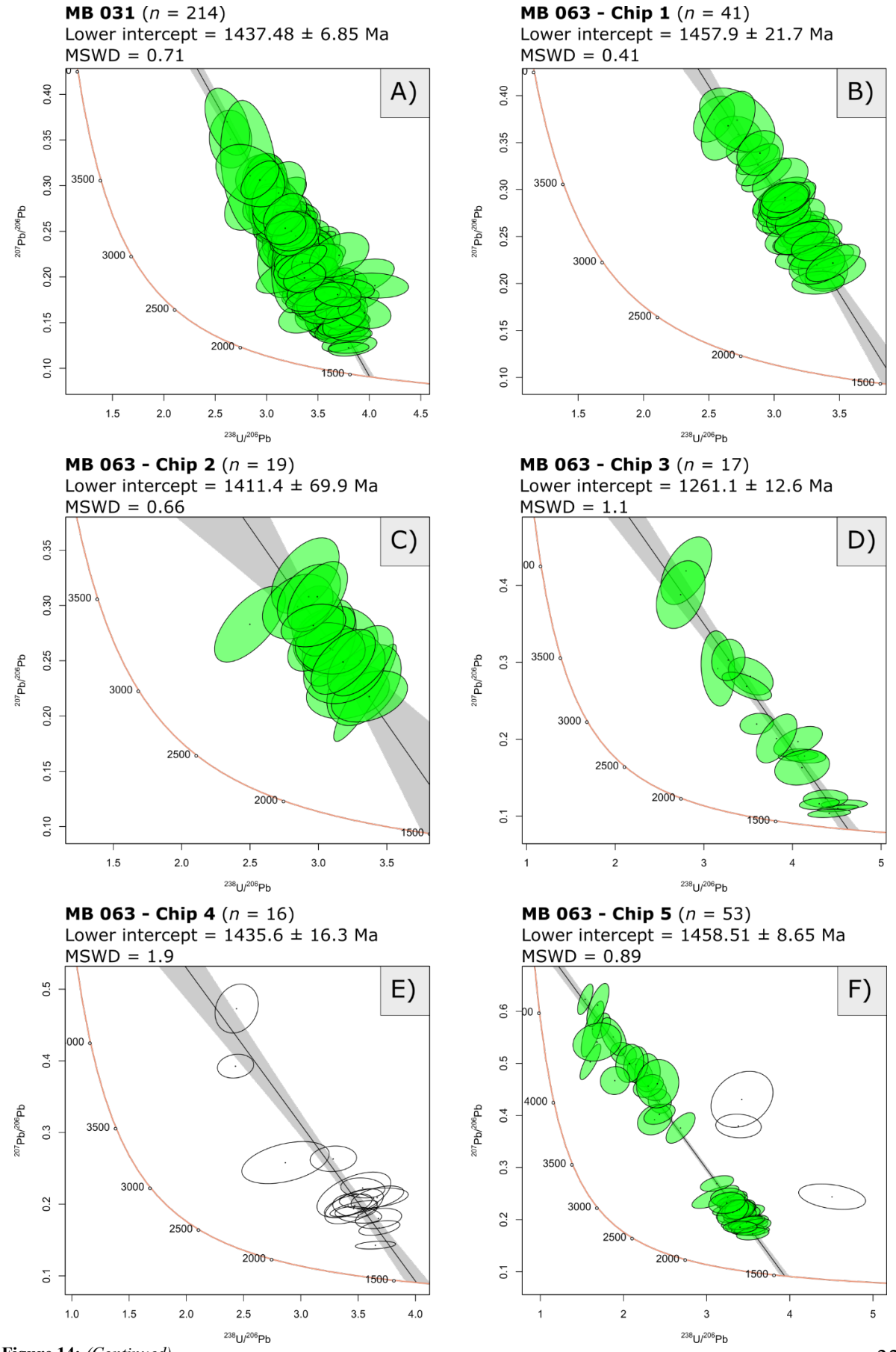

Figure 14: *(Continued).*

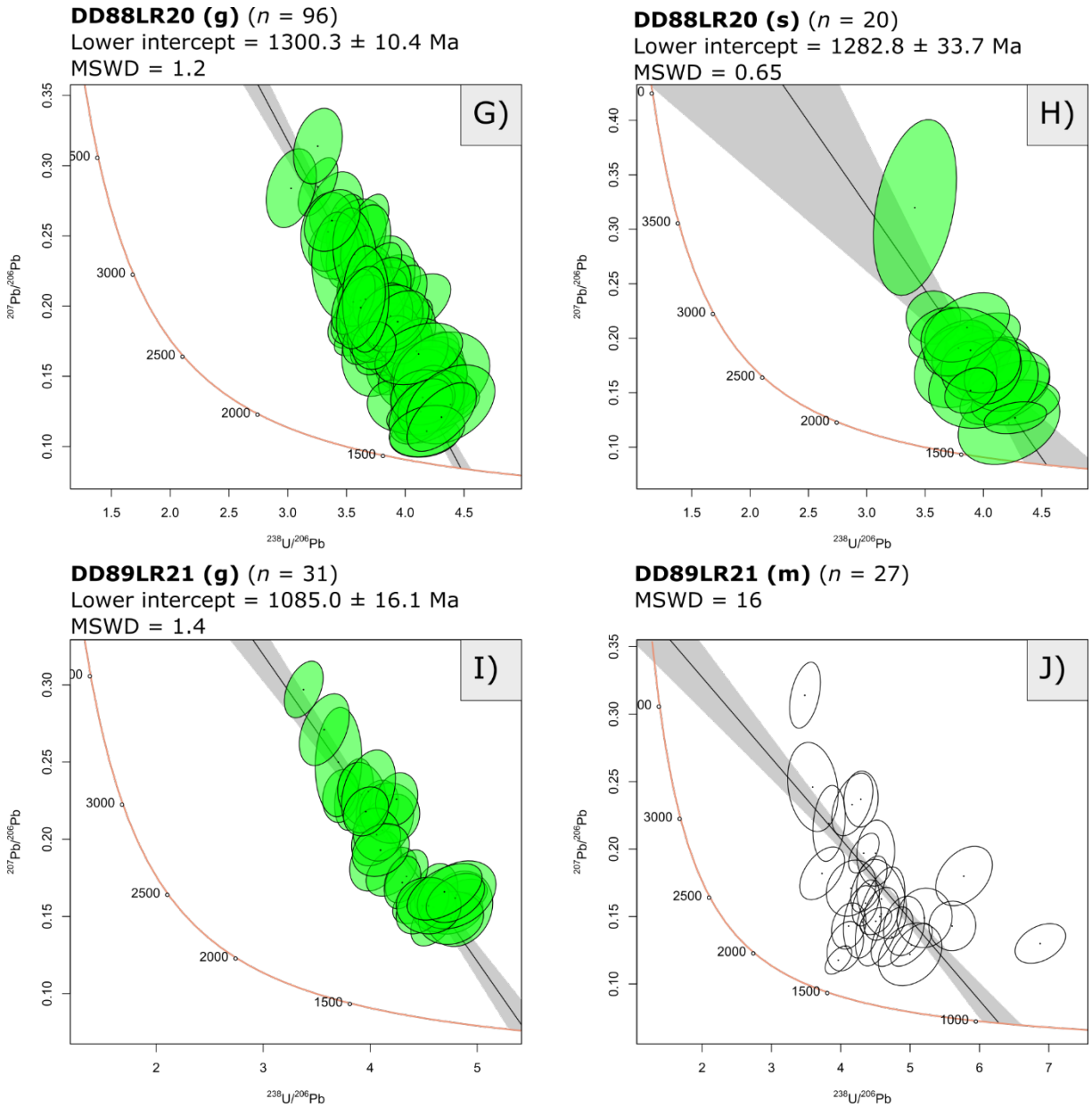

Figure 14: Terra-Wasserberg concordia plots for all apatite U/Pb analyses. White circles represent anomalous measurements or groups that do not provide a statistically robust age. **A-F)** show analyses from apatite grains within igneous host rocks. Due to the nature of sampling, rock chips from the same interval (MB 063) have different ages which cannot be spatially resolved. **G-J)** show analyses from single macroscopic apatite crystals from the coarse-grained assemblage. (g) = gridded spots on apatite away from other minerals, (s) = apatite analyses near cross-cutting sulphide stringers, (m) = apatite analyses near monazite inclusions. Data point error ellipses are 2σ.

3.3.2 Zircon Geochronology and Trace Element Distribution

A total of 103 LA-ICP-MS analyses were carried out on zircon grains recovered from the sample MB068(2) 206-214m. During data reduction in Iolite nine analyses were removed due to poor quality signals attributed to analysis of mixed zones, or inclusions.

Cathodoluminescence conducted on the grains reveals five distinct textural characteristics in the zircon population (Figure 15), geochemical characteristics of each analysis are presented in Figure 16, eleven analyses record unaltered magmatic zircon composition while eighty-three analyses have LREE enrichment characteristic of mixed or hydrothermal zircon.

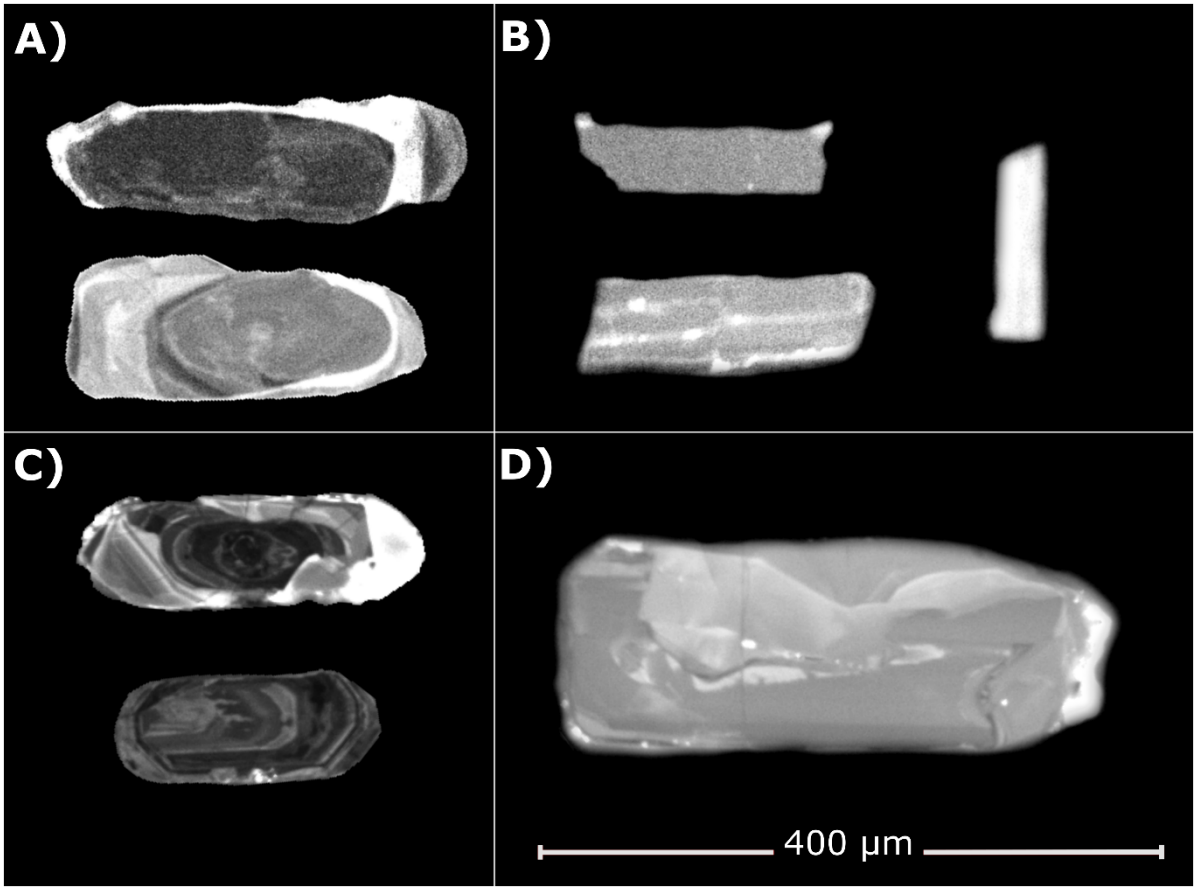

Figure 15: Selected zircon grains summarising the five main textural groups in this sample, using textural references from Corfu (2003). **A)** examples of two textures, cores with a poorly preserved structure, possibly metamict or recrystallised, and asymmetric bright rims. Bright rims are observed overgrowing all core textures to varying degrees. **B)** acicular zircon grains with elongation ratios of 1:3 or higher, this textural group has dark and bright linear zonation. **C)** Oscillatory zoned zircon cores, **D)** Patchy cores.

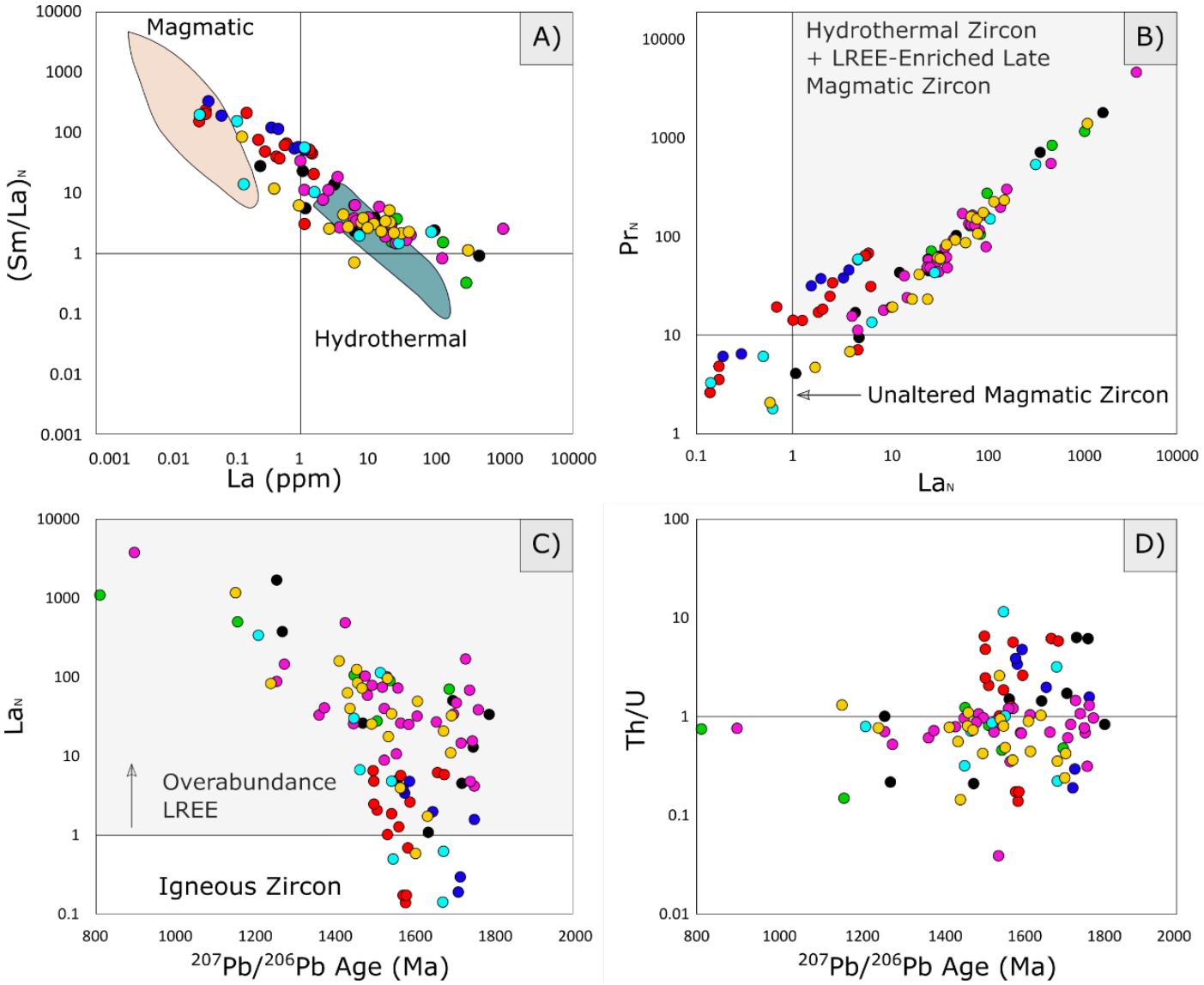

Figure 16: Magmatic/hydrothermal zircon discriminant diagrams from Wang, Guo, and Yang, (2019). **A)** shows the distribution of textural populations between the magmatic field and hydrothermal field. **B)** shows a small (n=9) group of zircons plotting in the 'unaltered magmatic' field. **C)** Ten analyses between 1545 and 1713 Ma plot in the igneous zircon field, numerous analyses over the same time period have high La and show increasing LREE as the $^{207}Pb/^{206}Pb$ age decreases. **D)** shows Th/U ratios of each analysis plotted against the $^{207}Pb/^{206}Pb$ age, there is a wide variation of Th/U over the entire population, all high Th/U ratios (>2) occur after 1500 Ma ($^{207}Pb/^{206}Pb$ age).

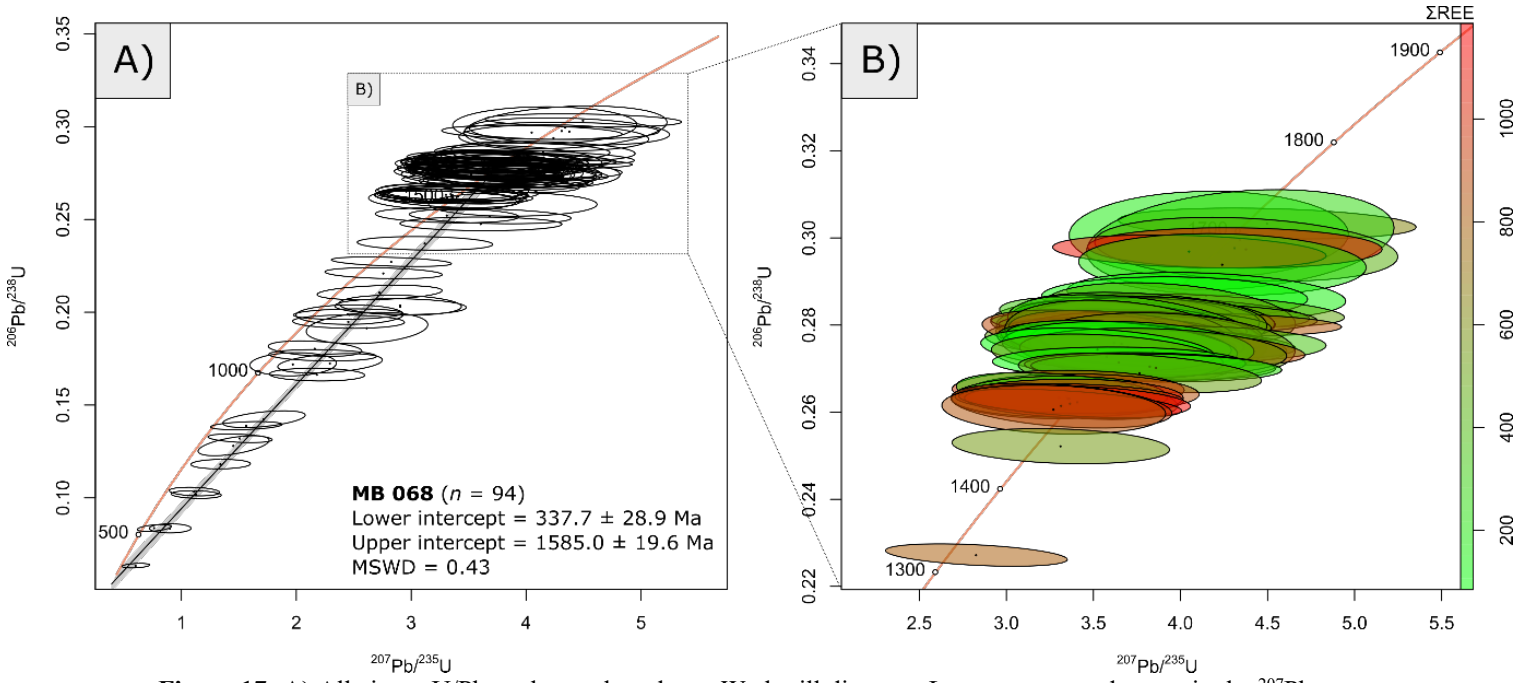

Figure 17: A) All zircon U/Pb analyses plotted on a Wetherill diagram. Large propagated errors in the ^{207}Pb measurements – likely due to low ^{207}Pb counts in the analysed zircons– causes intersection of error ellipses with the concordia line over an extended period. **B)** Zircon analyses within 10% concordance showing total rare-earth element concentrations (ΣREE) for each analysis, with a cluster of high-REE zircon at 1500 Ma. Data point error ellipses are 2σ.

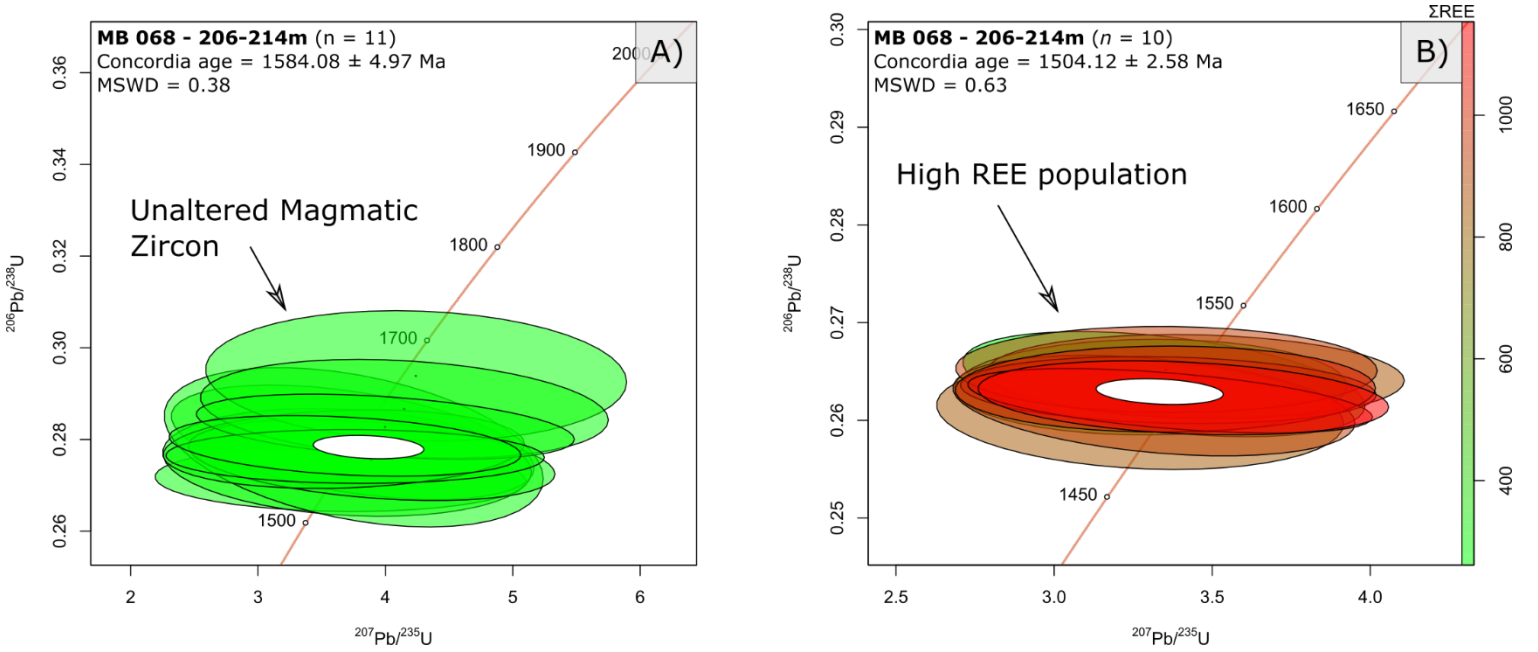

Figure 18: LA-ICP-MS zircon geochronology for geochemically distinct populations. **A)** Wetherill plot showing 'unaltered magmatic zircon' analyses identified in Figure 16. Unaltered magmatic zircons have characteristically low LREE and high $(Sm/La)_N$ values (Nadol *et al.,* 2014). **B)** Wetherill plot showing high total REE zircon population. Data point error ellipses are 2σ.

4. DISCUSSION

4.1 GEOCHRONOLOGY

This study employed both zircon and apatite geochronology to examine the geochronological record of high and low temperature events in the Mount Brady area. Zircon U-Pb geochronology is used for recording high-temperature events due to the >900°C closure temperature of the zircon crystal (Lee, Williams, & Ellis, 1997). Apatite passes the U-Pb closure temperature around 550-350°C (Chew & Spikings, 2015; Kirkland *et al.* 2018) making it useful for recording low temperature events such as cooling ages. Previous work on geochronology in the Coober Pedy Ridge and surrounding regions is summarised in Table 6.

Table 6: Selected geochronological data from the Coober Pedy subdomain and surrounding domains. CPR = Coober Pedy Ridge, MCR = Mabel Creek Ridge, UHT = ultra-high temperature. Shaded entries denote results from this study.

Area	Type of Age	Lithology	Mineral	Age	Reference
Nawa	Magmatic	Paragneiss	Zircon	2526 ± 7 Ma	Reid *et al.,* 2014
CPR	Magmatic	Orthogneiss	Zircon	1914 ± 8 Ma	Reid *et al.,* 2014
MCR	Deposition	Detrital	Zircon	~1740 Ma	Payne *et al.,* 2006
CPR	Magmatic	Gabbro	Zircon	1725 ± 7 Ma	Hand *et al.,* 2007
MCR	Metamorphic	Granites	Monazite	1700-1730 Ma	Payne *et al.,* 2008
CPR	Metamorphic	Orthogneiss	Zircon	1685 ± 6 Ma	Reid *et al.,* 2014
Ooldea	UHT event	Granulite	Zircon	1665-1650 Ma	Fanning *et al.,* 2007
CPR	Metamorphic	Granodiorite	Zircon	1589 ± 11 Ma	Fanning *et al.,* 2007
CPR	UHT event	Metapelitic granulite	Monazite	~1585 Ma	Cutts *et al.,* 2011
CPR	Magmatic	Granite	Zircon	1584.08 ± 4.97	This study
CPR	Metamorphic	Gabbro	Zircon	1565 ± 8 Ma	Fairclough, Fanning, & Daly, 1998
CPR	Metamorphic	Gabbro	Zircon	1565 ± 7 Ma	Hand *et al.,* 2007
Mt Woods	Metamorphic	Metasedimentary	Zircon	1587- 1576 Ma	Skirrow *et al.,* 2006
Nawa	Magmatic/ Metamorphic	Granite Dyke	Zircon	~1521 Ma	Reid *et al.,* 2014
Nawa	Metamorphic	Paragneiss	Zircon	1521 ± 9 Ma	Reid *et al.,* 2014
CPR	Metamorphic	Granite	Zircon	1504.12 ± 2.58 Ma	This study
Ooldea	Fault reactivation	-	Muscovite/ Kspar	1450 Ma	Howard *et al.,* 2014
CPR	Cooling	Granite	Apatite	1437.48 ± 6.85 Ma	This study
CPR	Cooling	Granite	Apatite	1457.90 ± 21.7 Ma	This study
CPR	Cooling	Granite	Apatite	1411.40 ± 69.9 Ma	This study
CPR	Cooling	Gabbro	Apatite	1413 ± 17 Ma	Hall *et al.,* 2018
CPR	Resetting?	Skarn assemblage	Apatite	1300.3 ± 10.40 Ma	This study
CPR	Resetting?	Granite	Apatite	1261.10 ± 12.60 Ma	This study
CPR	Resetting?	Skarn assemblage	Apatite	1085.0 ± 16.10 Ma	This study

4.1.1 Zircon

Previous zircon geochronology conducted on samples from Mount Brady found that the gabbroic lithologies have an emplacement age of 1725 ± 7 Ma and metamorphic overgrowth at 1566 ± 9 Ma. Zircon analyses from felsic rocks in this study identified a heavily altered zircon population with 11 analyses plotting as un-altered magmatic zircon (Figure 16). These zircons yield a crystallisation age of 1584.08 ± 4.97 (*n* = 11, MSWD = 0.38, Figure 18). This age is coincident with the Hiltaba Event (1595 – 1575 Ma; Hand *et al.,* 2007) and a period of known UHT metamorphism in the Coober Pedy Ridge (Cutts *et al.,* 2011). Most zircon analyses are highly enriched in light rare-earth elements, which is consistent with hydrothermal zircon growth (Wang *et al.,* 2019; Figure 16.c). Additionally, the analysed zircons display a strong lead-loss trend, which is statistically unlikely to represent lead loss from a single zircon population (*n* = 94, MSWD = 0.43; Figure 17.a). Zircons that have undergone lead loss have also been decoupled from the geochemical signatures of their original population. For this reason, and due to the large analytical errors caused by low ^{207}Pb in the zircon analyses, it is difficult to separate distinct zircon populations to infer discrete timings of metamorphic activity or the age of a thermal event that caused lead loss. However, a concordant cluster of REE enriched zircon, which yield an age of 1504.12 ± 2.58 Ma (*n* = 10, MSWD = 0.63, Figure 18.b), suggest a period of metamorphic/hydrothermal zircon growth around that time. Furthermore, Figure 16.c shows that La_N increases as the $^{207}Pb/^{206}Pb$ age decreases and that the Th/U ratio drops. These trends are both consistent with hydrothermal zircon growth. Zircon textural characteristics (Figure 15) were found to be independent of geochemical characteristics or specific ages.

4.1.2 Apatite

Apatite from four samples of the igneous lithologies (MB 031 and MB 063) displays cooling ages between ~1450Ma and 1400 Ma (Table 6; Figure 14). This is broadly consistent with previous work completed on the Coober Pedy Ridge, which interpreted regional cooling at ~1400 Ma (Hall *et al.,* 2018). The youngest apatite ages obtained in this study are those of the coarse-grained mineral assemblage, which provide ages of 1300.3 ± 10.4 Ma (n = 96, MSWD = 1.2; Figure 14.g; DD88LR20) to 1282.8 ± 33.7 Ma (n = 20, MSWD = 0.65; Figure 14.h; DD88LR20) and 1085.0 ± 16.1 Ma (n = 31, MSWD = 1.4; Figure 14.i; DD89LR21). Enigmatically, these youngest apatite ages cannot represent regional cooling as near-by apatite hosted in igneous lithologies records ~1400 Ma ages. Nor can they reliably be said to record the formation age of the coarse-grained mineral assemblage due to the similar rare earth patterns to the apatite contained within the igneous lithologies (Figure 10). Similarities in trace element patterns suggest the metamorphic fluids generated by, or affecting, the igneous lithologies are akin to the fluids responsible for the apatite growth in the coarse-grained assemblage. The two samples from the coarse-grained assemblage apatite have a large age difference (~215 Ma) but display similar geochemical patterns (Figure 10.c; Figure 10.d). This is inconsistent with the interpretation that their ages represent different formation times. However, it is consistent with an interpretation where the apatite samples from the coarse-grained assemblage have been reset at different times by minor local events, which have not been long-lived or of large enough scale to reset surrounding igneous lithologies. More information is required from areas within the Coober Pedy Ridge to identify the geological significance and distribution of the anomalously young apatite ages before conclusive interpretations can be made.

4.2 THE MOUNT BRADY PROSPECT

The basement rocks at the Mount Brady prospect are comprised of alternating units of forsteritic marble, thin monzonitic intervals between 2 and ~10 meters thick, gabbro, and a coarse-grained mineral assemblage of pyroxene, phlogopite, magnetite, and carbonate ± chalcopyrite ± pyrite ± apatite. Iron mineralisation is present as magnetite and there are trace quantities of copper mineralisation in the form of minor late-stage crosscutting stringers and intergrown magnetite-chalcopyrite. The coarse-grained assemblage is consistent with a magmatic-hydrothermal magnesian skarn (Yao, Chen, Lu, Wang, & Zhang, 2014; Meinert, Hedenquist, Satoh, & Matsuhisa, 2003). Skarns are coarse grained metamorphic rocks, which form through interaction of a carbonate rich lithology with hydrothermal fluids in processes such as metasomatism and contact metamorphism. The term 'skarn' is a very broad classification and skarn-like assemblages are commonly formed during the final crystallisation stages of an associated silicate magma (Meinert *et al.*, 2003). The coarse grain size is common in skarn systems and reflects a high fluid/rock ratio during metamorphism facilitating extensive grain growth (Meinert, 1992; Meinert *et al.,* 2003). Magnesian skarns are relatively uncommon and result from the hydrothermal replacement of magnesium rich carbonate-bearing lithologies such as dolomite (Yao *et al.,* 2014). During early high-temperature magnesian-skarn development forsterite is known to form in marbles due to infiltration of magmatic-hydrothermal fluids. However, original drilling logs identify forsteritic-marble as a potential carbonatite or a metamorphosed dolomitic marble (BHP, 2000). If this system is carbonatitic, the coarse-grained assemblage bears striking resemblance to mineralised zones in the Kovdor carbonatite complex of Murmansk Oblast, Russia, and the mineralogical composition of the forsteritic marble is similar to many known primary carbonatitic occurrences (Mikhailova *et al.*, 2017; Kalashnikov *et al.,* 2017; Mitchell,

2005; Tucker & Collerson, 1972). Numerous studies have shown that there is ambiguity surrounding the correct identification of uncommon carbonate lithologies (Le Bas *et al.,* 2004; Le Bas, Subbarao, & Walsh, 2002; Mitchell, 2005; Simandl & Paradis, 2018; Bell, 1989; Bell, 2009). For example, Bayan Obo, the world's largest REE-Nb-Fe type deposit still provokes controversy on the primary igneous or sedimentary origin of dolomitic marbles (Song *et al.,* 2018; Changhui, Yike, & Zhongjian*,* 2018). As such, mineralogic and textural features of mineral assemblages in carbonate lithologies are insufficient to classify a rock as carbonatite on their own due to the strong overlapping characteristics of carbonatites with metasedimentary and magmatic skarn carbonate lithologies. Interrogation of mineral chemistry provides the most robust indication for carbonatitic origin; however, multiple lines of evidence, such as trace element distributions in major mineral phases, are required to confidently support the correct interpretation in occurrences where field relationships are not evident due to overburden and limited drill hole coverage. Carbonatitic magmatism is yet unknown in the Gawler Craton but numerous occurrences, including Mount Brady, have been preliminarily classed as potential carbonatites or carbonatite complexes (e.g. BHP, 2000). Carbonatites may represent rare distal endmembers of the IOCG clan. Of the ~530 known carbonatite occurrences, 9% contain economic concentrations of Nb or REEs (Groves & Vielreicher, 2001; Woolley & Kjarsgaard, 2008). As such, carbonatites represent significant exploration targets, identification of carbonatitic activity in the northern Gawler Craton has associated economic implications and would provide basis for further exploration for carbonatites in the region.

4.2.1 Carbonatites

The term 'carbonatite' was first used to describe a carbonate lithology as being of igneous origin in 1895 at the Alnö Island carbonatite and alkaline ring-type intrusive complex in

Sweden. The term was applied again in 1921 at the Fen carbonatite complex in Norway (as cited in Marien, Dijkstra, & Wilkins, 2017). Initial proposals that the observed carbonate lithologies were of igneous origin were strongly contested, with arguments of limestone-syntexis and assimilation driven by associated silicate magmas, which would explain the ultra-basic rock types. The discovery of the only active 'modern-day' extrusive natrocarbonatite system at Oldoinyo Lengai in Tanzania showed that igneous carbonates – carbonatites – were possible (Mitchell, 2005). The definition of 'carbonatite' as a genetically distinct rock classification is widely stated to have >50 modal percent primary igneous carbonate and a <20 modal percent SiO_2 (Le Maitre *et al.,* 2004). Woolley *et al.* (1995) and Mitchell (2005) instead provide alternative mineralogical-genetic classifications, which recognise a spectrum of compositionally diverse but genetically related rocks derived from a single magma type. If the IUGS classification system is used, one can reasonably call any carbonate rich rock with apparent igneous origin a carbonatite. Therefore, magmatic hydrothermal activity, such as calcite veining or the formation of carbonate rich skarn mineral assemblages - which are present in the final stages of crystallisation of many magma types - can also be classified as 'carbonatitic'. This classification system is ineffective and can lead to the incorrect interpretation of carbonate-rich lithologies. The forsteritic marble at Mount Brady features characteristics very similar to a known South Australian carbonatite occurrence described by Tucker and Collerson in 1972, and carbonate-rich kimberlites from South Africa (Bosch 1971). The known South Australian carbonatite takes the form of numerous Jurassic-aged carbonatitic-lamprophyric dykes and plugs hosted within the Walloway diapir in the Adelaide Fold Belt. The Walloway carbonatitic lamprophyres contain 50 to 80 percent carbonate as a fine-to-medium grained porphyritic matrix. Two lithological suites are identified, one is characterised by an abundance of mica phenocrysts and the

second is characterised by pseudomorphed phenocrysts of serpentine after olivine. These carbonatitic lamprophyres have the same mineralogy and textural appearance as the Mount Brady occurrence, however the true origin of the Mount Brady forsteritic marble was never confirmed.

4.2.2 Metamorphosed impure marbles and magnesian skarns

Simandl and Paradis (2018) discuss the main obstacles faced in correctly discriminating meta-sedimentary sequences and carbonatitic rocks. Metamorphism, such as that commonly associated with the later stages of carbonatite emplacement, modifies or resets the mineralogical, textural, and chemical characteristics of the carbonatite and surrounding rocks. Many of these characteristics can be mimicked in metamorphosed sedimentary carbonate lithologies. The alternative explanations for carbonate-hosted mineral assemblages with ambiguous origin involves regionally metamorphosed impure dolomitic marble or, rarely, magmatic magnesian skarns. Extensive forsterite formation is recorded in magnesium-skarn surrounding a contact aureole in the Alta of Utah, where dolomitic marbles host forsterite (Loury *et al.,* 2015). Experimental studies have shown that forsterite can be formed by the reactions described by Ferry, Ushikubo, and Valley (2011). The study also states that the formation of forsterite in dolomite marble can be driven by a wide range of fluid compositions. Bucher (1981) describes a chlorite-spinel-marble occurrence in Svalbard, which formed as a result of regional high-grade metamorphism. This occurrence is indisputably of metasedimentary origin but has a similar mineral assemblage to the Mount Brady carbonate assemblage and known carbonatites - dolomite, calcite, olivine, clinohumite, amphibole, diopside, chlorite, spinel, phlogopite, Fe-Ti oxides, and serpentine. Magmatic magnesian skarns can also produce similar mineral assemblages, for instance, the Siberian

Angara and Ilim river basins host tens of significant iron oxide systems known as Angara-Ilim type deposits. The deposits are characterised by brecciation, magnesian and calcitic skarns, and late stage crosscutting magnetite-apatite-calcite veins. Typically, the magnesian skarns in these deposits are composed of forsterite, diopside, calcite, spinel and magnetite. Phlogopite and serpentine are also often present (Soloviev 2010). However, the same paper briefly explores the potential of the magnesian skarns being of carbonatitic origin. In summary, it is difficult to classify uncommon carbonate-hosted mineral assemblages in lithologies with ambiguous origins based on their mineralogy and petrological textures alone.

4.3 MINERAL TRACE ELEMENT COMPOSITIONS

4.3.1 Carbonates

Primary magmatic carbonates generally have high strontium and total rare-earth-elements whereas crustal carbonates tend towards lower concentrations of these elements (Rosatelli, Wall, Stoppa, & Brilli, 2010). Discrimination diagrams from Macdonald, Chakhmouradian, Couëslan, and Reguir (2017) plotted in Figure 19 show analyses from the forsteritic marble and coarse-grained assemblage. There is a wide variation in elemental composition between similar lithologies of the forsteritic marble, which may be attributed to spatial distribution, geochemical composition of the primary lithology, or variation in metamorphic fluid compositions. All but one analysis plot within the crustal carbonate field, which supports a non-carbonatitic origin. The trace element spider plots for the carbonates (Figure 8) reveal a distinct negative europium anomaly and a lack of a cerium anomaly. This is diagnostic of carbonates from non-carbonatitic lithologies (Le Bas *et al.*, 2002; Loubet, Bernat, Javoy, & Allegre 1972). Figure 19.b shows that all carbonates plot consistently above the primitive mantle Y/Ho ratio (27.85). This also supports the interpretation that these marbles are not of carbonatitic origin.

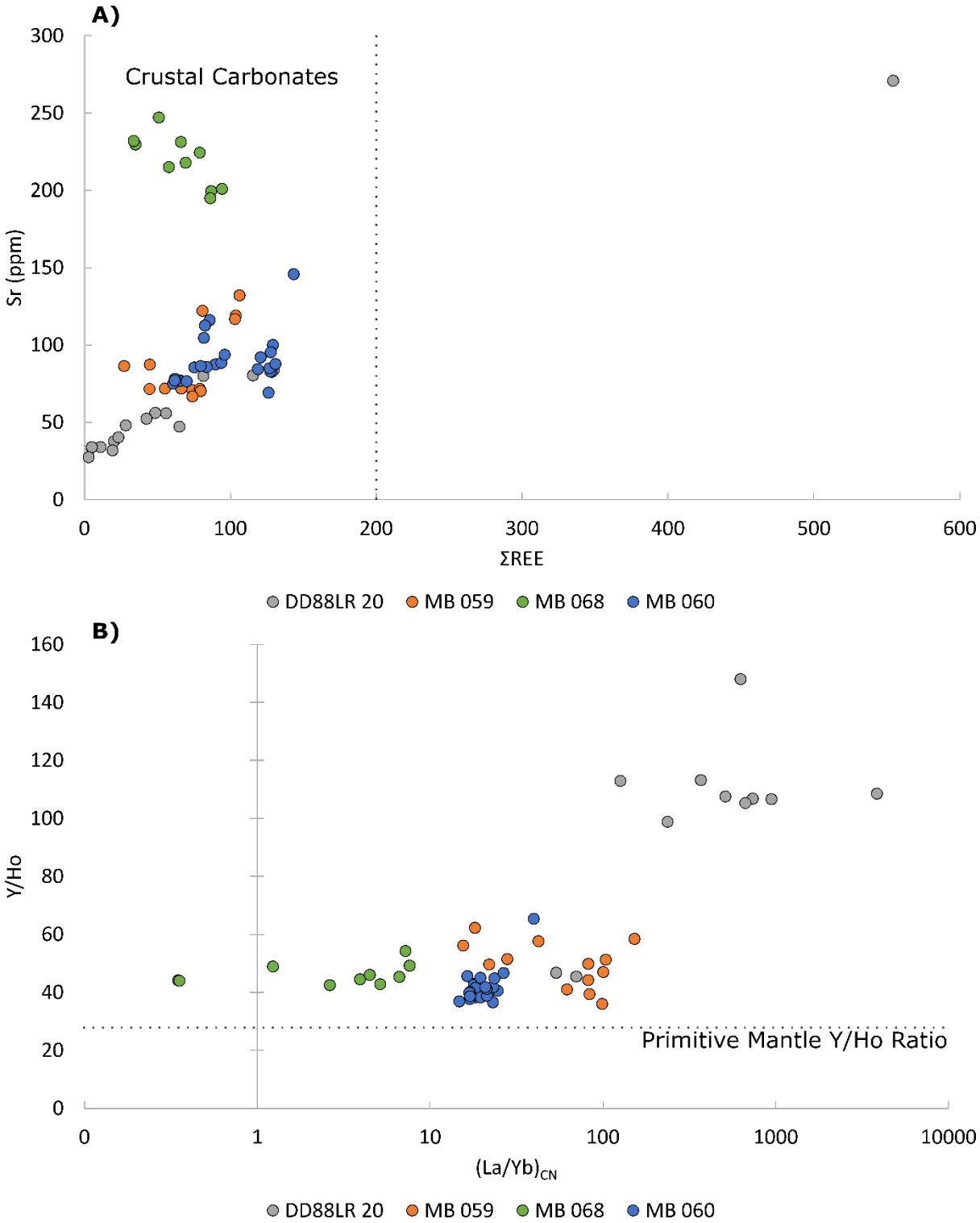

Figure 19: Bivariate diagrams from MacDonald *et al.* (2017) showing trace element variation between carbonates in the forsteritic marble and hydrothermal assemblage. **A)** All but one analysis plot within the crustal carbonate field of Chakhmouradian *et al.* (2009). **B)** Several measurements were removed due to lack of detection of either La, Ho, or Yb. All samples consistently show Y/Ho values above that of the primitive mantle ratio of 27.85 (Lubetskaya & Korenaga, 2007).

4.3.2 Spinel and Olivine

Olivine crystals may be present as porphyroblasts in a metamorphosed carbonate rich lithology or, in the case of a carbonatite, as xenocrystic grains sourced from the mantle. Spinel is not common in carbonatitic and associated lithologies, but the presence of spinel has been reported at several carbonatitic occurrences such as the South African Bonfontein Sill (Gaspar & Wyllie, 1984), and the Russian Kovdor phoscorite-carbonatite complex (Kalashnikov *et al.,* 2017; Mikhailova *et al.,* 2018). Comparison of the nickel and chromium contents of both spinel and olivine (Figure 11) shows negligible concentrations of these elements supporting a metamorphic origin (Nozaka 2010; Peltonen, 1990). Additionally, comparison of olivine calcium contents (<<1% - shown in Table 4 - to magmatic olivine calcium contents (>>1 wt% CaO; Libourel, 1999) demonstrate a large disparity. This lends further support to the metamorphic interpretation for the forsteritic marbles at Mount Brady.

4.3.3 Phlogopite

Phlogopite can be present in carbonatites and metamorphosed carbonate lithologies. In carbonatites, micas tend to have a broad compositional range trending from tetraferriphlogopite-phlogopite to biotite and eastonite (Traversa *et al.,* 2001; Brod *et al.,* 2001). Additionally, there is a trend in carbonatitic mica showing early high-Al phases grading towards tetraferriphlogopite due to Al depletion during magmatic crystallisation. The samples from the hydrothermal vein assemblage plot tightly along the phlogopite-annite trend and the mica from the forsteritic marble shows slight enrichment of Al compared to the phlogopite of the coarse-grained assemblage (Figure 9), which further supports the non-carbonatite interpretation.

4.3.4 Magnetite

Recent publications have used trace elements to identify temperature brackets of mineral systems and discriminate mineral system origins from magnetite analyses. Figure 13 shows bivariate plots modified from Nadoll, Angerer, Mauk, French, and Walshe (2014) demonstrating that the magnetite analysed in this study plot widely along the skarn border (Figure 13.a; Figure 13.c). The different lithologies tend to group well in the temperature approximation diagram (Figure 13.b) showing MB 059, DD88LR 20, and MB 068 plotting in the ~300-500°C field. However, the mineral assemblage present in the forsteritic marble is stable under these conditions only if there is high CO_2 activity in the metamorphic fluids (Konzett, Tropper, & Tessadri, 2003). Analyses from the coarse-grained assemblage additionally show that the coarse-grained magnetite formed at a higher temperature than the intergrown magnetite-chalcopyrite in the same assemblage. Similarities between the coarse hydrothermal magnetite and the disseminated magnetite in the forsteritic marble (e.g. Figure 11; Figure 13) suggests that the magnetite from the magnetite-pyrite-chalcopyrite intergrowth in the coarse-grained assemblage is a secondary - lower temperature - generation of magnetite rather than representative of magnetite alteration of the host rock prior hydrothermal overprinting.

4.4 PROSPECTIVITY IN THE COOBER PEDY RIDGE REGION

Due to the substantial exhumation that the Coober Pedy Ridge has experienced since the main IOCG-forming Hiltaba thermal event, the modern-day prospectivity of the Coober Pedy Ridge for Olympic Dam aged IOCG style mineralisation is likely low. IOCG systems form in the 'IOCG window' of the upper 12 kilometres of the crust (Porter, 2010). In the Coober Pedy Ridge, most – if not all – of this section of crust has been exhumed and eroded post Hiltaba-Event, which makes it highly unlikely that a fertile Olympic Dam aged IOCG system exists in this area. The presence of numerous magnetic and gravitational anomalies, and intersection of the weakly mineralised system at the Mount Brady prospect shows that mineralisation is present in this region. However, the quality, origin, and extent of mineralisation is not currently clear.

5. CONCLUSIONS

- The origin of the forsteritic marble at Mount Brady is shown through mineral chemistry to be an early stage in the development of the Mount Brady magnesian skarn system resulting from infiltration of magmatic-hydrothermal fluids into a sedimentary dolomitic carbonate.
- Mineral chemistry of analysed carbonates, spinel, olivine, and phlogopite provide conclusive evidence that the Mount Brady forsteritic marble is not of carbonatitic origin.
- The similarities in apatite trace element data between the coarse-grained hydrothermal skarn assemblage and the igneous-hosted apatite provides a geochemical link between the felsic intrusive bodies and the skarn system. However, due to subsequent resetting of analysed apatite samples, the timing of

fluid flow, which led to the generation of the coarse-grained skarn assemblage is unclear.

- Zircon geochronology records a complex thermal history with significant isotopic and geochemical perturbation, unaltered magmatic zircons show evidence for felsic magmatism at 1584.08 ± 4.97 Ma. This is coincident with the Hiltaba Event and prior to the onset of the Kararan Orogeny.
- A geochemically distinct population of rare earth element enriched zircons provide an age of 1504.12 ± 2.58 Ma, however, the extent and significance of a potential thermal event at this time is unclear. The enrichment of REEs in the younger zircon and the presence of other REE enriched prospects in the Coober Pedy Ridge may represent a widespread fluid flow that is trackable through further geochronological observations in the region.

ACKNOWLEDGEMENTS

I wish to extend my appreciation and thanks to my supervisors Dr Richard Lilly and Professor Martin Hand for their recommendations, guidance, and assistance in keeping me on track throughout this project. SIMEC, Geoff Johnson, and the geology team based in Whyalla, South Australia for providing funding, initial background, and sample collection. Dr. Sarah Gilbert and Dr. Benjamin Wade from Adelaide Microscopy, and Dr. Morgan Blades from the University of Adelaide for their assistance, training, and advice throughout the year. The staff at the Tonsley Core Library for their assistance with historic core inspection and sampling. Tom Wise at the Geological Survey of South Australia for his contributions and previous observations from the Mount Brady prospect. PhD candidates at the University of Adelaide, specifically Bradley Cave, Mitchell Bockmann, Renée Tamblyn, and Darwin Subarkah for their assistance with data processing and support. Finally, I wish to extend my thanks to the AusIMM and the EEF Scholarship Committee for providing generous financial support over this year.

REFERENCES

Andersen, T. (2002). Correction of common lead in U–Pb analyses that do not report 204Pb. *Chemical Geology,* 192(1-2), 59-79. doi:10.1016/S0009-2541(02)00195-X

Armit, R., Betts, P., Schaefer, B., Yi, K., Kim, Y., Dutch, R. A., . . . Ailleres, L. (2017). Late Palaeoproterozoic evolution of the buried northern Gawler Craton. *Precambrian Research, 291*, 178-201.

Bell, K. (1989). *Carbonatites : genesis and evolution*. London: Unwin-Hyman.

BHP. (2000). Safari, Lake Woorong, Leonard Rise, Thunderstorm Creek and Brumby Creek areas (Coober Pedy Ridge Project). Quarterly and six-monthly progress, plus annual and final, joint activity reports for the period 22/4/1991 to 22/3/2000. Adelaide, South Australia: BHP.

BHP. (2018). *Annual Report 2018*. Retrieved from BHP: https://www.bhp.com/investor-centre/annual-report-2018/annual-report-2018.

Bosch, J. L. (1971). The petrology of some kimberlite occurrences in the Barkly West District, Cape Province. *South African Journal of Geology, 74*(2), 75-101.

Brod, J. A., Gaspar, J. C., De Araújo, D. P., Gibson, S. A., Thompson, R. N., & Junqueira-Brod, T. C. (2001). Phlogopite and tetra-ferriphlogopite from Brazilian carbonatite complexes: petrogenetic constraints and implications for mineral-chemistry systematics. *Journal of Asian Earth Sciences, 19*(3), 265-296. doi:10.1016/S1367-9120(00)00047-X.

Bucher-Nurminen, K. (1981). Petrology of chlorite-spinel marbles from NW Spitsbergen (Svalbard). *Lithos, 14*(3), 203-213. doi: https://doi.org/10.1016/0024-4937(81)90042-6.

Chakhmouradian, A. R., Böhm, C. O., Demény, A., Reguir, E.P., Hegner, E., Creaser, R.A., Halden, N.M., & Yang, P. (2009). Kimberlite from Wekusko Lake, Manitoba: actually a diamond-indicator-bearing dolomite carbonatite. *Lithos*, 1125, 347-357.

Changhui. K. E., Yike, L., & Zhongjian, Wu. (2018). The First Discovery of the Early Palaeozoic Carbonatite in the Bayan Obo Deposit, Inner Mongolia, China: Evidence from Zircon U-Pb Geochronology. *Acta Geologica Sinica, 92*(6), 2440. doi:10.1111/1755-6724.13742.

Chew, D. M., & Spikings, R. A. (2015). Geochronology and Thermochronology Using Apatite: Time and Temperature, Lower Crust to Surface. *Elements, 11*(3), 189-194. doi:10.2113/gselements.11.3.189.

Chew, D. M., Petrus, J. A., & Kamber, B. S. (2014). U–Pb LA–ICPMS dating using accessory mineral standards with variable common Pb. *Chemical Geology, 363*, 185-199. doi: https://doi.org/10.1016/j.chemgeo.2013.11.006.

Corfu, F. (2003). Atlas of Zircon Textures. *Reviews in Mineralogy and Geochemistry, 53*(1), 469-500. doi:10.2113/0530469.

Cutts, K., Hand, M., & Kelsey, D. E. (2011). Evidence for early Mesoproterozoic (ca. 1590Ma) ultrahigh-temperature metamorphism in southern Australia. *Lithos, 124*(1), 1-16. doi: https://doi.org/10.1016/j.lithos.2010.10.014.

Dutch, R., Hand, M., & Kinny, P. D. (2008). High-grade Paleoproterozoic reworking in the southeastern Gawler Craton, South Australia. *Australian Journal of Earth Sciences, 55*(8), 1063-1081. doi:10.1080/08120090802266550.

Fairclough, M. C., Fanning, C. M. & Daly, S. J. (1998). *Tectonic evolution and exploration potential of the Gawler Craton, South Australia*. Retrieved from: http://pid.geoscience.gov.au/dataset/ga/81513, https://researchdata.ands.org.au/tectonic-evolution-exploration-south-australia.

Ferris, G. M., Schwarz, M. P., & Heithersay, P. (2002). The geological framework, distribution and controls of Fe-oxide Cu-Au mineralisation in the Gawler Craton, South Australia. Part I–Geological and tectonic framework. *Hydrothermal iron oxide copper-gold and related deposits: A global perspective, 2*, 9-31.

Ferry, J. M., Ushikubo, T., & Valley, J. W. (2011). Formation of Forsterite by Silicification of Dolomite during Contact Metamorphism. *Journal of Petrology, 52*(9), 1619-1640. doi:10.1093/petrology/egr021.

Forbes, C., Giles, D., Jourdan, F., Sato, K., Omori, S., & Bunch, M. (2012). Cooling and exhumation history of the northeastern Gawler Craton, South Australia. *Precambrian Research, 200-203*, 209-238. doi:10.1016/j.precamres.2011.11.003.

Fraser, G., Reid, A., & Stern, R. (2012). Timing of deformation and exhumation across the Karari Shear Zone, north-western Gawler Craton, South Australia. *Australian Journal of Earth Sciences, 59*(4), 547-570.

Gaspar, J. C., & Wyllie, P. J. (1984). The alleged kimberlite-carbonatite relationship: evidence from ilmenite and spinel from Premier and Wesselton mines and the Benfontein sill, South Africa. *Contributions to Mineralogy and Petrology, 85*(2), 133-140. doi:10.1007/BF00371703.

Groves, D., & Vielreicher, N. (2001). The Phalabowra (Palabora) carbonatite-hosted magnetite-copper sulfide deposit, South Africa: An end-member of the iron-oxide copper-gold-rare earth element deposit group? *Mineralium Deposita, 36*, 189-194. doi:10.1007/s001260050298.

Hall, J. W., Glorie, S., Reid, A. J., Boone, S. C., Collins, A. S., & Gleadow, A. (2018). An apatite U–Pb thermal history map for the northern Gawler Craton, South Australia. *Geoscience Frontiers, 9*(5), 1293-1308. doi:https://doi.org/10.1016/j.gsf.2017.12.010.

Hand, M., Reid, A., & Jagodzinski, L. (2007). Tectonic framework and evolution of the Gawler craton, Southern Australia. *Economic Geology, 102*(8), 1377-1395. doi:10.2113/gsecongeo.102.8.1377.

Jackson, S. E., Pearson, N. J., Griffin, W. L., & Belousova, E. A. (2004). The application of laser ablation-inductively coupled plasma-mass spectrometry to in situ U–Pb zircon geochronology. *Chemical Geology, 211*(1-2), 47-69. doi:10.1016/j.chemgeo.2004.06.017.

Kalashnikov, A., Pakhomovsky, Y., Bazai, A., Goryainov, P., Mikhailova, J., Yakovenchuk, V., & Konopleva, N. (2017). Subsolidus Evolution of the Magnetite-Spinel-UlvöSpinel Solid Solutions in the Kovdor Phoscorite-Carbonatite Complex, NW Russia. *Minerals, 7*(11), 215. doi:10.3390/min7110215.

Kelsey, D., & Hand, M. (2014). On ultrahigh temperature crustal metamorphism: Phase equilibria, trace element thermometry, bulk composition, heat sources, timescales and tectonic settings. *Geoscience Frontiers, 6*. doi:10.1016/j.gsf.2014.09.006.

Kirkland, C. L., Yakymchuk, C., Szilas, K., Evans, N., Hollis, J., McDonald, B., & Gardiner, N. J. (2018). Apatite: a U-Pb thermochronometer or geochronometer? *Lithos, 318-319*, 143-157. doi:https://doi.org/10.1016/j.lithos.2018.08.007.

Konzett, P., Tropper, R, & Tessadri, J. (2003). Spinel-bearing carbonates as petrogenetic recorders of the Variscan pT evolution of the Austroalpine basement of the Ötztal Complex (Tyrol, Austria). *Journal of the Czech Geological Society, 48*, 1-2.

Le Bas, M. J., Ba-bttat, M. A. O., Taylor, R. N., Milton, J. A., Windley, B. F., & Evins, P. M. (2004). The carbonatite-marble dykes of Abyan Province, Yemen Republic: the mixing of mantle and crustal carbonate materials revealed by isotope and trace element analysis. *Mineralogy and Petrology, 82*(1), 105-135. doi:10.1007/s00710-004-0056-2.

Le Bas, M. J., Subbarao, K. V., & Walsh, J. N. (2002). Metacarbonatite or marble? — the case of the carbonate, pyroxenite, calcite–apatite rock complex at Borra, Eastern Ghats, India. *Journal of Asian Earth Sciences, 20*(2), 127-140. doi:https://doi.org/10.1016/S1367-9120(01)00030-X.

Le Maitre, R., Streckeisen, A., Zanettin, B., Le Bas, M., Bonin, B., & Bateman, P. (Eds.). (2002). *Igneous Rocks: A Classification and Glossary of Terms: Recommendations of the International Union of Geological Sciences Subcommission on the Systematics of Igneous Rocks.* Cambridge: Cambridge University Press. doi:10.1017/CBO9780511535581.

Lee, J. K. W., Williams, I. S., & Ellis, D. J. (1997). Pb, U and Th diffusion in natural zircon. *Nature, 390*(6656), 159-162. doi:10.1038/36554.

Libourel, G. (1999). Systematics of calcium partitioning between olivine and silicate melt: implications for melt structure and calcium content of magmatic olivines. *Contributions to Mineralogy and Petrology, 136*(1), 63-80. doi:10.1007/s004100050524.

Loubet, M., Bernat, M., Javoy, M., & Allegre, C. J. (1972). Rare earth contents in carbonatites. *Earth and Planetary Science Letters, 14*(2), 226-232. doi:https://doi.org/10.1016/0012-821X(72)90011-8.

Ludwig, K. R. (1998). On the Treatment of Concordant Uranium-Lead Ages. *Geochimica et Cosmochimica Acta, 62*(4), 665-676. doi:10.1016/S0016-7037(98)00059-3.

Lyubetskaya, T., & Korenaga, J. (2007). Chemical composition of Earth's primitive mantle and its variance: 1. Method and results. *Journal of Geophysical Research: Solid Earth, 112*(B3), n/a-n/a. doi:10.1029/2005JB004223.

Macdonald, J., Chakhmouradian, A., Couëslan, C., & Reguir, E. (2017). Discriminative study of genetically diverse car-bonate rocks in the northwest-ern Pikwitonei granulite domain and Split Lake block, central Manitoba (parts of NTS 63P11, 12, 64A1). *Report of Activities*, 30-41.

Marien, C., Dijkstra, A., & Wilkins, C. (2017). The hydrothermal alteration of carbonatite in the Fen Complex, Norway: Mineralogy, geochemistry, and implications for rare-earth element resource formation. *Mineralogical Magazine*, in press. doi:10.1180/minmag.2017.081.070.

McDonough, W., & Sun, S. S. (1995). The composition of the Earth. *Chem. Geol., 67*, 1050-1056.

Meinert, L. D. (1992). Skarns and Skarn Deposits. *Geoscience Canada, 19*(4).

Meinert, L. D., Hedenquist, J. W., Satoh, H., & Matsuhisa, Y. (2003). Formation of Anhydrous and Hydrous Skarn in Cu-Au Ore Deposits by Magmatic Fluids. *Economic Geology, 98*(1), 147-156. doi:10.2113/gsecongeo.98.1.147.

Mitchell, R. H. (2005). Carbonatites and carbonatites and carbonatites. *The Canadian Mineralogist, 43*(6), 2049-2068. doi:10.2113/gscanmin.43.6.2049.

Morrissey, L. J., Barovich, K. M., Hand, M., Howard, K. E., & Payne, J. L. (2019). Magmatism and metamorphism at ca. 1.45 Ga in the northern Gawler Craton: The Australian record of rifting within Nuna (Columbia). *Geoscience Frontiers, 10*(1), 175-194. doi: https://doi.org/10.1016/j.gsf.2018.07.006.

Nadoll, P., Angerer, T., Mauk, J. L., French, D., & Walshe, J. (2014). The chemistry of hydrothermal magnetite: a review. *Ore Geology Reviews, 61*, 1-32. doi:10.1016/j.oregeorev.2013.12.013.

Nozaka, T. (2010). A note on compositional variation of olivine and pyroxene in thermally metamorphosed ultramafic complexes from SW Japan. *Okayama University Earth Science Report, 17*(1), 1-5.

Oz Minerals Ltd. (2017). *Carrapateena project mineral resource restatement and ore reserve statement*. Retrieved from Oz Minerals: https://www.ozminerals.com/operations/resources-reserves/

Oz Minerals Ltd. (2018). *Prominent Hill 2018 mineral resource and ore reserve statement and explanatory notes*. Retrieved from Oz Minerals: https://www.ozminerals.com/operations/resources-reserves/

Paton, C., Hellstrom, J., Paul, B., Woodhead, J., & Hergt, J. (2011). Iolite: Freeware for the visualisation and processing of mass spectrometric data. *Journal of Analytical Atomic Spectrometry, 26*(12), 2508-2518. doi:10.1039/C1JA10172B.

Payne, J. L., Barovich, K. M., & Hand, M. (2006). Provenance of metasedimentary rocks in the northern Gawler Craton, Australia: Implications for Palaeoproterozoic reconstructions. *Precambrian Research, 148*(3), 275-291. doi:10.1016/j.precamres.2006.05.002.

Peltonen, P. (1990). Metamorphic olivine in pictritic metavolcanics from southern Finland. *Bulletin of the Geological Society of Finland, 62*(2), 99-114. doi:10.17741/bgsf/62.2.001.

Petrus, J. A., & Kamber, B. S. (2012). VizualAge: A Novel Approach to Laser Ablation ICP-MS U-Pb Geochronology Data Reduction. *Geostandards and Geoanalytical Research, 36*(3), 247-270. doi:10.1111/j.1751-908X.2012.00158.x.

Porter, M. (2010). Current Understanding of Iron Oxide Associated-Alkali Altered Mineralised Systems: Part II, A Review. In (pp. pp. 33-106).

Reid, A. J., Jagodzinski, E. A., Armit, R. J., Dutch, R. A., Kirkland, C. L., Betts, P. G., & Schaefer, B. F. (2014). U-Pb and Hf isotopic evidence for Neoarchean and Paleoproterozoic basement in the buried northern Gawler Craton, South Australia. *Precambrian Research, 250*, 127-142. doi:10.1016/j.precamres.2014.05.019.

Rosatelli, G., Wall, F., Stoppa, F., & Brilli, M. (2010). Geochemical distinctions between igneous carbonate, calcite cements, and limestone xenoliths (Polino carbonatite, Italy): Spatially resolved LAICPMS analyses. *Contributions to Mineralogy and Petrology, 160*, 645-661. doi:10.1007/s00410-010-0499-x.

Shields, G., & Stille, P. (2001). Diagenetic constraints on the use of cerium anomalies as palaeoseawater redox proxies: an isotopic and REE study of Cambrian phosphorites. *Chemical Geology, 175*(1), 29-48. doi: https://doi.org/10.1016/S0009-2541(00)00362-4.

Simandl, G. J., & Paradis, S. (2018). Carbonatites: related ore deposits, resources, footprint, and exploration methods. *Applied Earth Science, 127*(4), 123-152. doi:10.1080/25726838.2018.1516935.

Sláma, J., Košler, J., Condon, D. J., Crowley, J. L., Gerdes, A., Hanchar, J. M., . . . Whitehouse, M. J. (2008). Plešovice zircon — A new natural reference material for U–Pb and Hf isotopic microanalysis. *Chemical Geology, 249*(1), 1-35. doi:10.1016/j.chemgeo.2007.11.005.

Song, W., Xu, C., Smith, M. P., Chakhmouradian, A. R., Brenna, M., Kynický, J., . . . Tang, H. (2018). Genesis of the world's largest rare earth element deposit, Bayan Obo, China: Protracted mineralization evolution over ~1 b.y. *Geology, 46*(4). doi:10.1130/G39801.1.

Spencer, C. J., Kirkland, C. L., & Taylor, R. J. M. (2016). Strategies towards statistically robust interpretations of in situ U–Pb zircon geochronology. *Geoscience Frontiers, 7*(4), 581-589. doi: https://doi.org/10.1016/j.gsf.2015.11.006.

Swain, G., Woodhouse, A., Hand, M., Barovich, K., Schwarz, M., & Fanning, C. (2005). Provenance and tectonic development of the late Archaean Gawler Craton, Australia; U–Pb zircon, geochemical and Sm–Nd isotopic implications. *Precambrian Research, 141*(3-4), 106-136.

Taylor, R. G. (2019). *Paragenetic interpretation – derived via petrological investigation of 9 samples from drill holes DD88LR19, DD88LR20 and DD89LR21, Mount Brady, South Australia*. Attached as Appendix 3.

Teasdale, J. (1997). *Methods for understanding poorly exposed terranes: the interpretive geology and tectonothermal evolution of the western Gawler Craton.* (Unpublished doctoral dissertation). University of Adelaide, Adelaide. Retrieved from: http://hdl.handle.net/2440/19235.

Thompson, J., Meffre, S., Maas, R., Kamenetsky, V., Kamenetsky, M., Goemann, K., . . . Danyushevsky, L. (2016). Matrix effects in Pb/U measurements during LA-ICP-MS analysis of the mineral apatite. *Journal of Analytical Atomic Spectrometry, 31*(6), 1206-1215. doi:10.1039/C6JA00048G.

Tong, L., Wilson, C., & Vassallo, J. (2004). Metamorphic evolution and reworking of the Sleaford Complex metapelites in the southern Eyre Peninsula, South Australia. *Australian Journal of Earth Sciences, 51*(4), 571-589.

Traversa, G., Gomes, C. B., Brotzu, P., Buraglini, N., Morbidelli, L., Principato, M. S., . . . Ruberti, E. (2001). Petrography and mineral chemistry of carbonatites and mica-rich rocks from the Araxá complex (Alto Paranaíba Province, Brazil). *Anais da Academia Brasileira de Ciências, 73*, 71-98.

Tucker, D. H., & Collerson, K. D. (1972). Lamprophyric intrusions of probable carbonatitic affinity from South Australia. *Journal of the Geological Society of Australia, 19*(3), 387-391. doi:10.1080/00167617208728808.

Vermeesch, P. (2018). IsoplotR: A free and open toolbox for geochronology. *Geoscience Frontiers, 9*(5), 1479-1493. doi:https://doi.org/10.1016/j.gsf.2018.04.001.

Wang, M., Guo, W., & Yang, W. (2019). Detrital zircon trace elements from the Mesozoic Jiyuan Basin, central China and its implication on tectonic transition of the Qinling Orogenic Belt. *Open Geosciences, 11*(1), 125-139. doi:10.1515/geo-2019-0011

Wiedenbeck, M., Allé, P., Corfu, F., Griffin, W. L., Meier, M., Oberli, F., . . . Spiegel, W. (1995). Three natural zircon standards for U-Th-Pb, Lu-Hf, trace element and REE analyses. *Geostandards Newsletter, 19*(1), 1-23. doi:10.1111/j.1751-908X.1995.tb00147.x.

Woolley, A. R., Bergman, S. C., Edgar, A. D., Le Bas, M. J., Mitchell, R. H., Rock, N. M., & Scott Smith, B. H. (1996). Classification of lamprophyres, lamproites, kimberlites, and the kalsilitic, melilitic, and leucitic rocks. *The Canadian Mineralogist, 34*(2), 175-186.

Woolley, A., & Kjarsgaard, B. (2008). Global carbonatite database. *Geol. Surv. Can., Open File, 5796*.

Yao, Y., Chen, J., Lu, J., Wang, R., & Zhang, R. (2014). Geology and genesis of the Hehuaping magnesian skarn-type cassiterite-sulfide deposit, Hunan Province, Southern China. *Ore Geology Reviews, 58*, 163-184.

Zhou, Z.-J., Tang, H., & Chen, Z.-L. (2017). Trace elements of magnetite and iron isotopes of the Zankan iron deposit, westernmost Kunlun, China: A case study of seafloor hydrothermal iron deposits. *Ore Geology Reviews, 80*, 1191-1205. doi:10.1016/j.oregeorev.2016.09.020.

APPENDIX 1: METHODS

SAMPLES AND INSTRUMENT PARAMETERS

Table 1: Sample names, descriptions, and analytical methods employed.

Sample	Sample Type	Depth	Rock ID	Dateable Minerals / Analytical methods
MB 031	Thin section	70m – 72m	Monzonite	Apatite / EBS, MLA
MB 031-1	Thin section	74m – 76m	Monzonite	- / EBS, MLA, LA-ICP-MS (Trace and U/Pb)
MB 032	Thin section	64m – 74m	Gabbro	- / EBS, MLA
MB 059	Thin section	110m -112m	Forsteritic Marble	- / EBS, SEM
MB 060	Thin section	214m – 216m	Forsteritic Marble	- / EBS, SEM
MB 063	Thin section	154m – 160m	Monzonite	Apatite / EBS, MLA, LA-ICP-MS (Trace and U/Pb)
MB 068	Thin section	94m – 104m	Biotite-Pyroxene rock	- / EBS, MLA
MB 068-1	Thin section	126m – 136m	Forsteritic Marble	- / EBS, SEM
DD88LR 20	Thin section	165.2m	Coarse-grained assemblage	- / LA-ICP-MS (Trace elements)
MB 068-2	Heavy minerals	206 – 214m	Intermediate Granite	Zircon / Panning, Frantz magnetic separation, Cathodoluminescence, LA-ICP-MS
MB 063-1	Heavy minerals	102-104	Felsic Granite	No zircons recovered / Panning, Frantz magnetic separation
DD89LR 21	Grain mount	203.75m	Apatite - Coarse- grained assemblage	Apatite / EBS, MLA, LA-ICP-MS (Trace and U/Pb)
DD88LR 20-1	Grain mount	188m	Apatite - Coarse- grained assemblage	Apatite / EBS, MLA, LA-ICP-MS (Trace and U/Pb)

Table 2: Scanning electron microscope parameters for EBS, MLA, Photomicrography, and cathodoluminescence (CL) imaging.

Method	EBS + MLA Mapping	Thin section Photomicrography	Grain mount Photomicrography	CL
Samples	MB031, MB031(1), MB032, MB063, MB068	MB060, MB068(1)	MB060(1)	MB068(2)
Instrument	Quanta-600 SEM	Quanta-600 SEM	Quanta-450 SEM	Quanta-600 SEM
Beam Energy	30 kV	30 kV	10 kV	20 kV
Working Distance	10mm	10mm	10mm	17mm
Spot size	7	N/A	N/A	7

Table 3: Target descriptions for LA-ICP-MS geochronology and trace element analysis in selected thin sections and grain mounts.

Name	Sample	Mineral	Spots	Target Description
MB 031	MB 031	Apatite	230	Large euhedral apatite grains within two monzonite RC chips
MB 063	MB 063	Apatite	158	Large euhedral apatite grains within five syenite RC chips
DD89LR21(g)	DD89LR 21	Apatite	36	Gridded analyses of a single macroscopic apatite grain, spots in areas of pure apatite.

Name	Sample	Mineral	Spots	Target Description
DD89LR21(m)	DD89LR 21	Apatite	31	Spots on a single macroscopic apatite grain near small (1-5µm) monazite accessory grains.
DD88LR20(g)	DD88LR 20	Apatite	96	Gridded analyses on fragments of a single macroscopic apatite grain, spots in areas of pure apatite.
DD88LR20(s)	DD88LR 20	Apatite	28	Spots on fragments of a single macroscopic apatite grain, spots next to sulphide stringers.
MB 068	MB 068(1)	Zircon	103	Spots on oscillatory cores, metamict (?) cores and light/dark overgrowth rims of zircons identified by CL imaging. Full description of individual zircon analyses provided in Appendix 2.

Table 4: Instrument parameters during LA-ICP-MS trace element and geochronology sessions. Analysed minerals were apatite, zircon, calcite, phlogopite, magnetite, spinel and olivine.

Apatite	
Instrument	Agilent 7900x ICP-MS
Spot Size	50µm
Fluence	3.5 J/cm^2
Repetition rate	5 Hz
Cleaning period	5 seconds
Rest period	20 seconds
Laser warming period (background collection)	30 seconds
Ablation period	30 seconds
Monitored Masses (Geochronology)	^{27}Al, ^{29}Si, ^{31}P, ^{35}Cl, ^{51}V, ^{55}Mn, ^{57}Fe, ^{65}Cu, ^{88}Sr, ^{89}Y, ^{90}Zr, ^{93}Nb, ^{139}La, ^{140}Ce, ^{141}Pr, ^{146}Nd, ^{147}Sm, ^{153}Eu, ^{157}Gd, ^{159}Tb, ^{163}Dy, ^{165}Ho, ^{166}Er, ^{169}Tm, ^{172}Yb, ^{175}Lu, ^{204}Pb,^{206}Pb, ^{207}Pb, ^{208}Pb, ^{232}Th, ^{238}U
Apatite standard glasses	NIST612, OD306, MAD, 401
Ablation Sequence	2x MAD, 2x 401, 2xOD306, 2x NIST612, 17x Unknown (apatite)
Data Reduction Scheme	Iolite, VizualAge_UcomPBine, Trace_element_DRS
Zircon, Calcite, Phlogopite, Magnetite, Spinel, Olivine	
Instrument	Agilent 7900x ICP-MS
Spot Size	29µm
Fluence	2 J/cm^2 for zircon analyses, 3.5 J/cm^2 for other minerals
Repetition rate	5hz
Cleaning period	5 seconds
Rest period	20 seconds
Background collection period	30 seconds
Ablation period	30 seconds
Monitored Masses (Geochronology)	^{31}P, ^{29}Si, ^{24}Mg, ^{27}Al, ^{39}K, ^{43}Ca, ^{47}Ti, ^{51}V, ^{53}Cr, ^{55}Mn, ^{57}Fe, ^{60}Ni, ^{88}Sr, ^{89}Y, ^{90}Zr, ^{93}Nb, ^{106}Pd, ^{137}Ba, ^{139}La, ^{140}Ce, ^{141}Pr, ^{146}Nd, ^{147}Sm, ^{153}Eu, ^{157}Gd, ^{159}Tb, ^{163}Dy, ^{165}Ho, ^{166}Er, ^{169}Tm, ^{172}Yb, ^{175}Lu, ^{178}Hf, ^{181}Ta, ^{195}Pt, ^{204}Pb,^{206}Pb, ^{207}Pb, ^{208}Pb, ^{232}Th, ^{238}U
Standards	NIST 610, GJ, Plesovice, 91500, NIST 612, GSD
Ablation Sequence	2x NIST 610, 2x GJ, 2x Plesovice, 2x 91500, 18x Unknown (zircon) 2x NIST 612, 2x GSD, 2x GSD @ 13µm, 2x GSD @ 29µm, 18x Unknown (calcite/magnetite/olivine/phlogopite/spinel)
Data Reduction Scheme	Iolite, U_Pb_GeoChron4, Trace_Element_X

APPENDIX 2: ADDITIONAL PETROGRAPHIC IMAGES

5.1 M031 70-72m – Monzonite

This sample is comprised of two large RC chips of a fine to medium grained felsic intrusive rock. The matrix is heavily altered but is likely to be a feldspar; grain boundaries are destroyed. Several grains of plagioclase retain euhedral shapes but are also highly altered. Minor poikiloblastic clinopyroxene is present and appears to be chloritised with inclusions of quartz. Numerous apatite grains are present ranging from 20 to >200 microns. Late-stage carbonate stringer veins crosscut the sample. There is a far higher abundance of biotite in the second grain and the textures in the second chip seem to have been preserved to a greater extent than the first chip. Apatite is present mostly as grey euhedral crystals with a wide variation in size from sub-20µm to greater than 200µm.

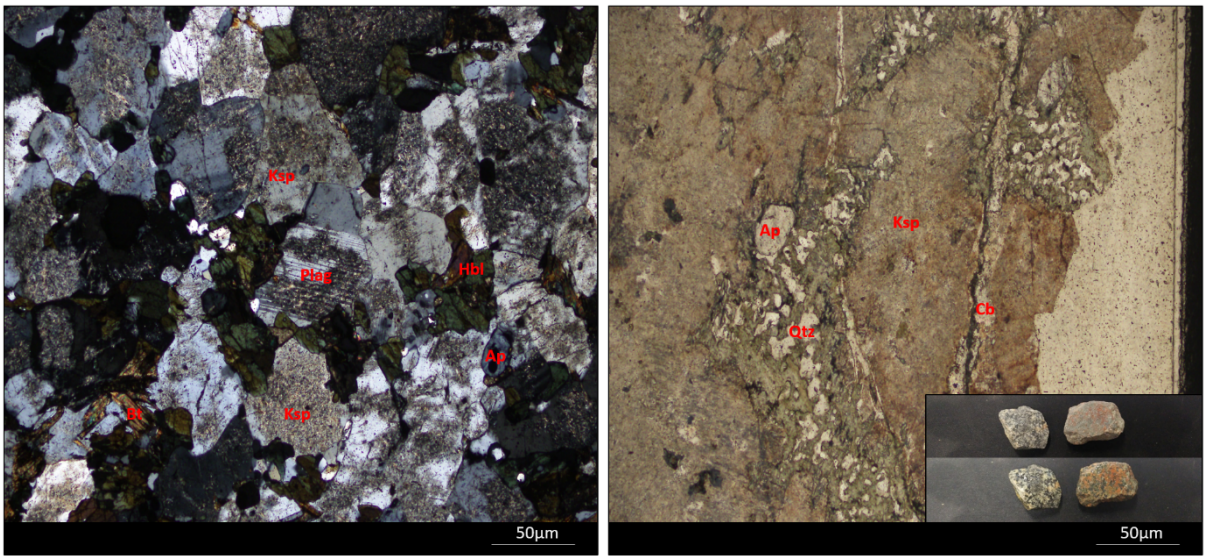

Figure 1: Left - Photomicrograph under crossed-nicols showing a heavily altered monzonite from M031 70-72m. Right - Photomicrograph under plane-polarised light showing crosscutting late-stage carbonate veins and poikiloblastic clinopyroxene with quartz inclusions. Ksp = potassium feldspar, Bt = biotite, Qtz = quartz, Cb = Carbonate, Ap = apatite, Plag = plagioclase feldspar, Hbl = hornblende.

5.2 MB031 (1) 74-76m - Monzonite

This sample has strong magnetite alteration (patching) in a plagioclase rich rock, identified as a monzonite; magnetite spots account for approximately 20% of the rock mass with feldspars at 60% and clinopyroxene at 20% mineral grains are well preserved with no destructive alteration and sharp grain boundaries.

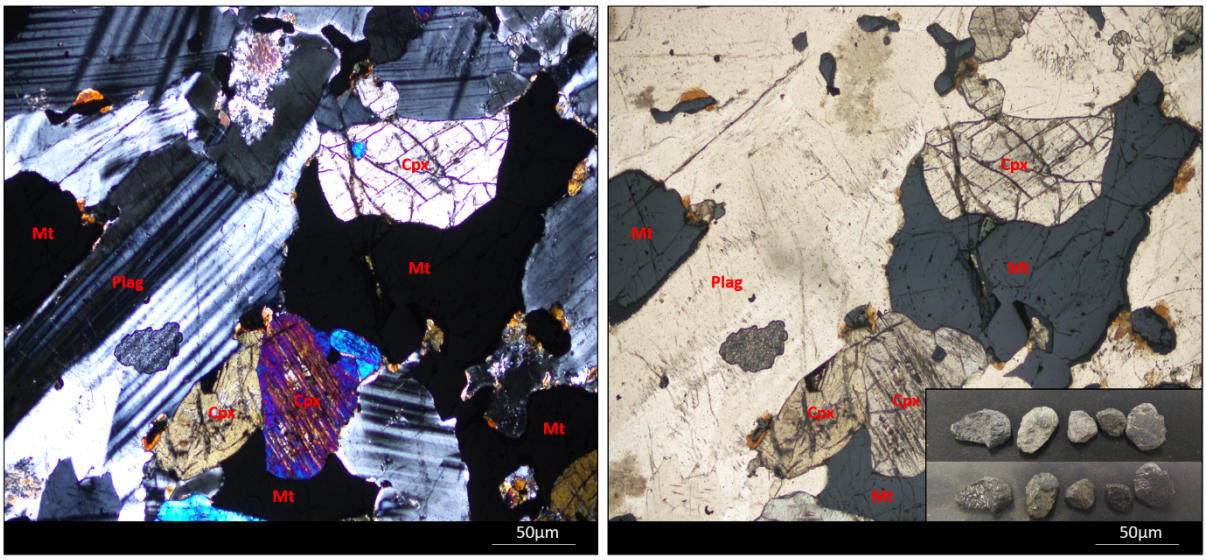

Figure 2: Comparison of the same field-of-view showing coarse plagioclase and clinopyroxene, magnetite spotting is present and pervasive throughout this sample.

5.3 MB032 64-74m - Gabbro

This sample has variable grain size from very coarse to very fine, magnetite alteration spots are pervasive and late stage crosscutting carbonate veins are present.

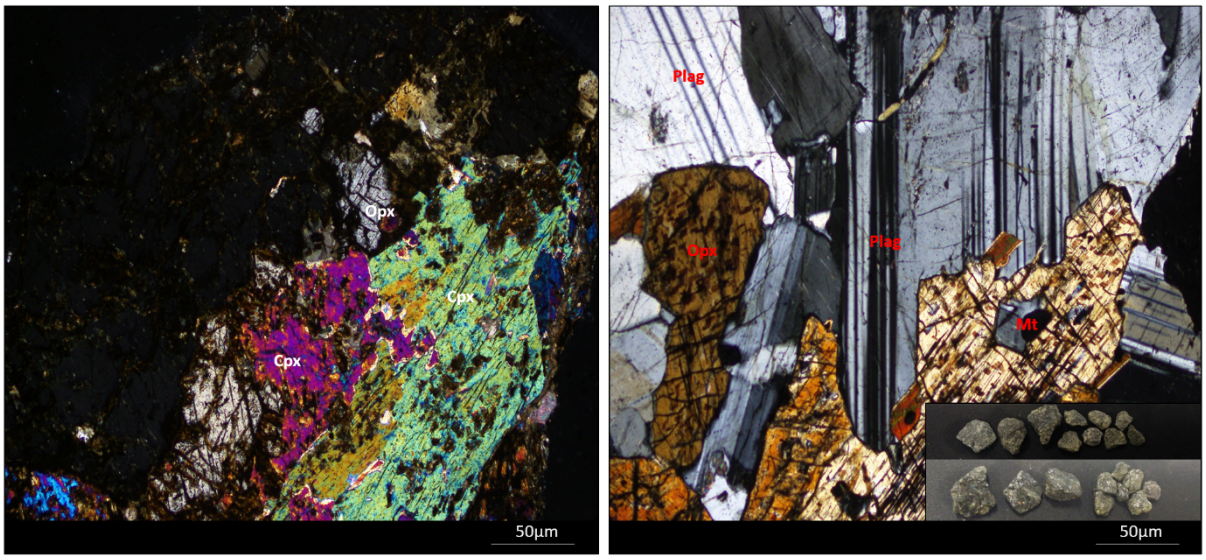

Figure 3: Left - Photomicrograph under crossed-nicols showing clinopyroxene and orthopyroxene. Right - Photomicrograph under crossed-nicols showing coarse plagioclase and pyroxenes.

5.4 MB068 94-104m - Phlogopite-Pyroxene rock

A largely monomineralic phlogopite rock with crosscut by a late stage magnetite vein with minor sulphides (chalcopyrite + pyrite). Some chips are comprised largely of altered clinopyroxene and phlogopite with pervasive brown staining.

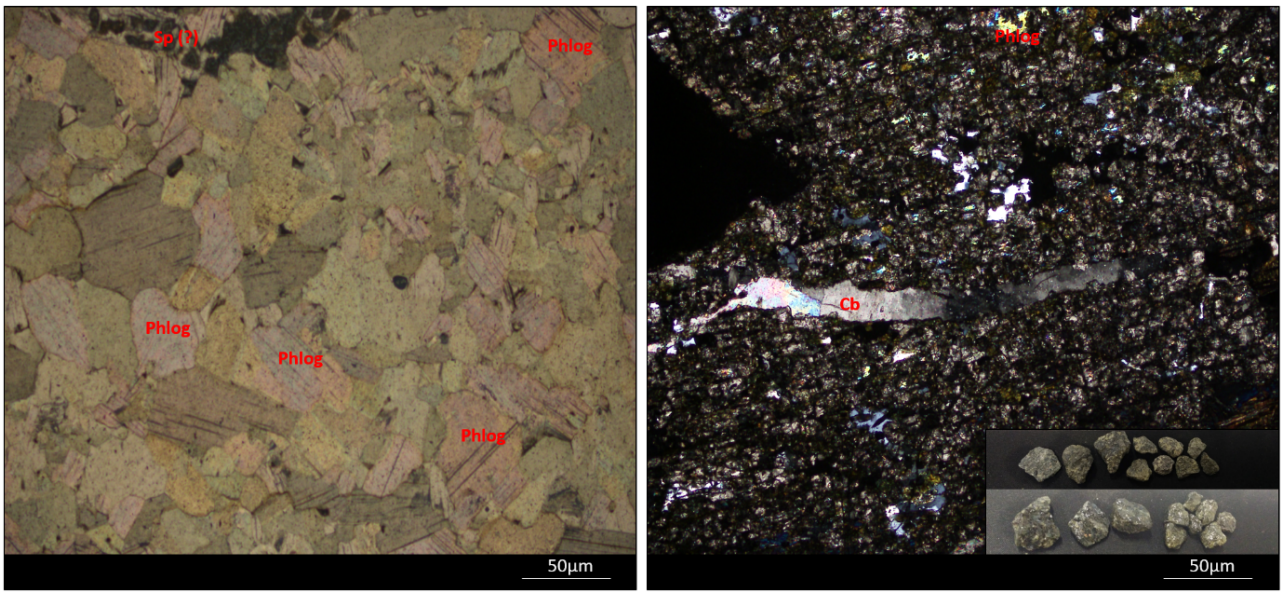

Figure 4: Left - Photomicrograph under plane-polarised light showing a nearly pure phlogopite composition and curious spinel-bearing carbonate veining in the top left. Right - Photomicrograph under crossed-nicols showing minor foliation in a very fine-grained matrix with a crosscutting carbonate vein.

5.5 MB063 154-160 – Monzonite

This sample has the same mineralogy and textures as MB031 70-72m but has undergone stronger red-rock alteration leading to the discolouration of the contained apatites.

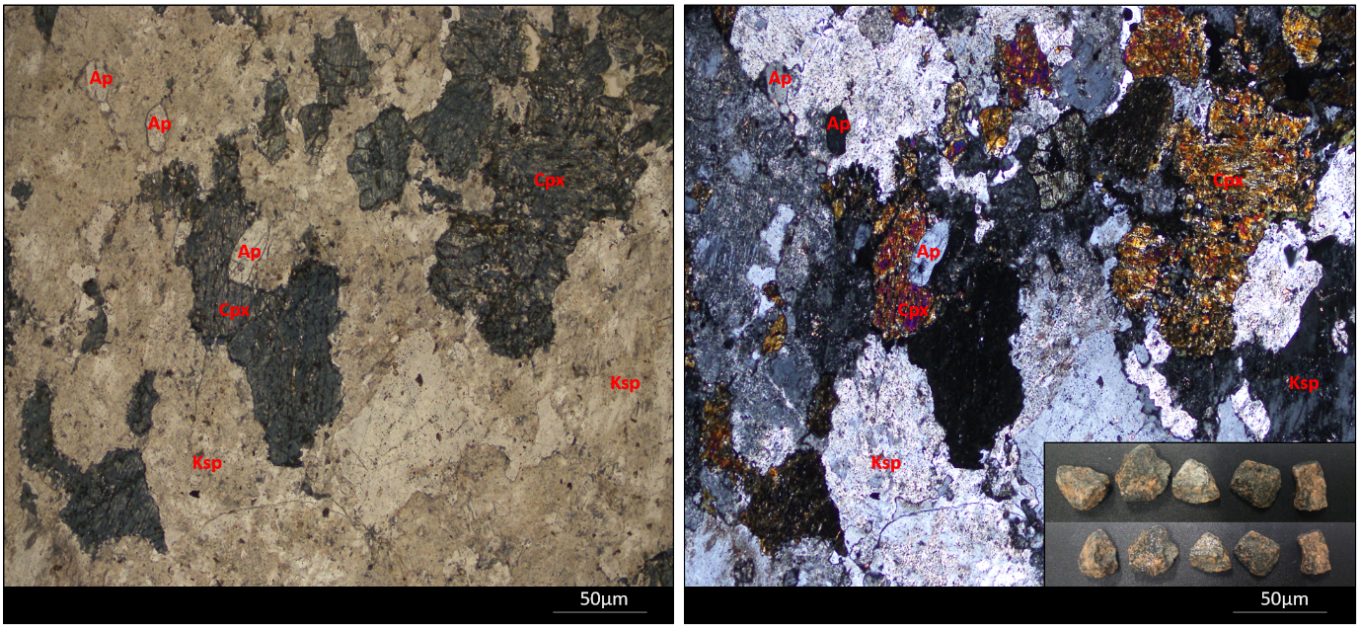

Figure 5: Comparison of the same field-of-view showing similar textures and mineralogy to MB031 70-72m with stronger red-rock alteration.

3.1.7 MB060 214-216m - Forsteritic Marble

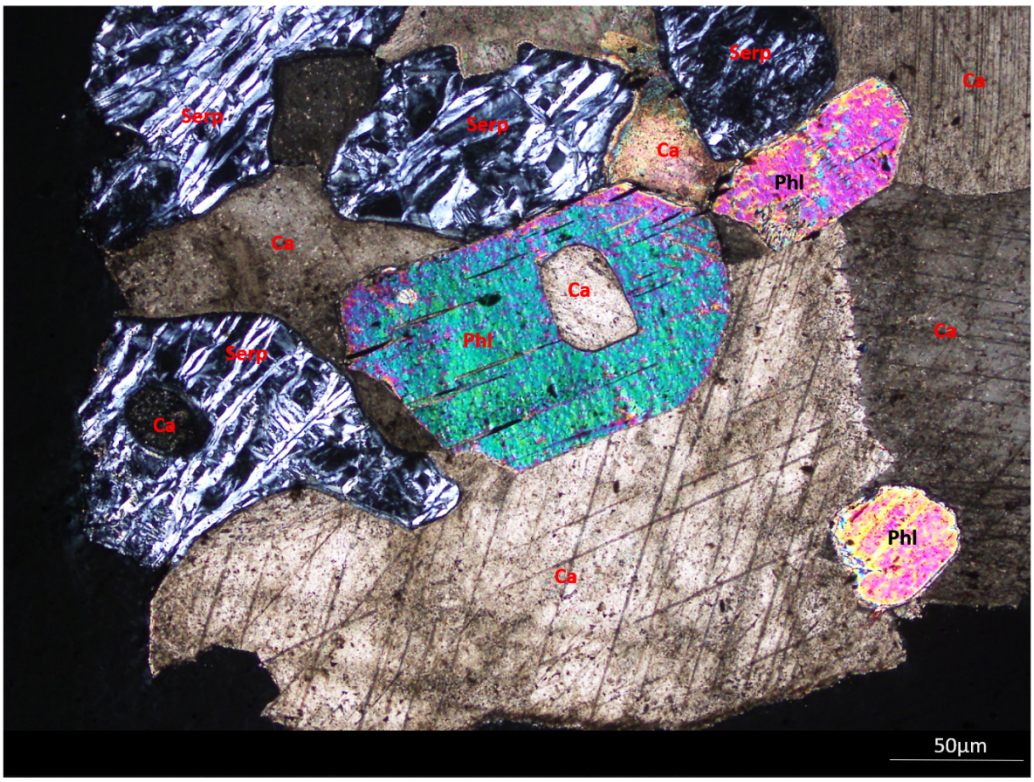

Figure 6: Photomicrograph under crossed-nicols showing 'droplet' inclusion texture of calcite within both phlogopite and a serpentinised olivine grain.

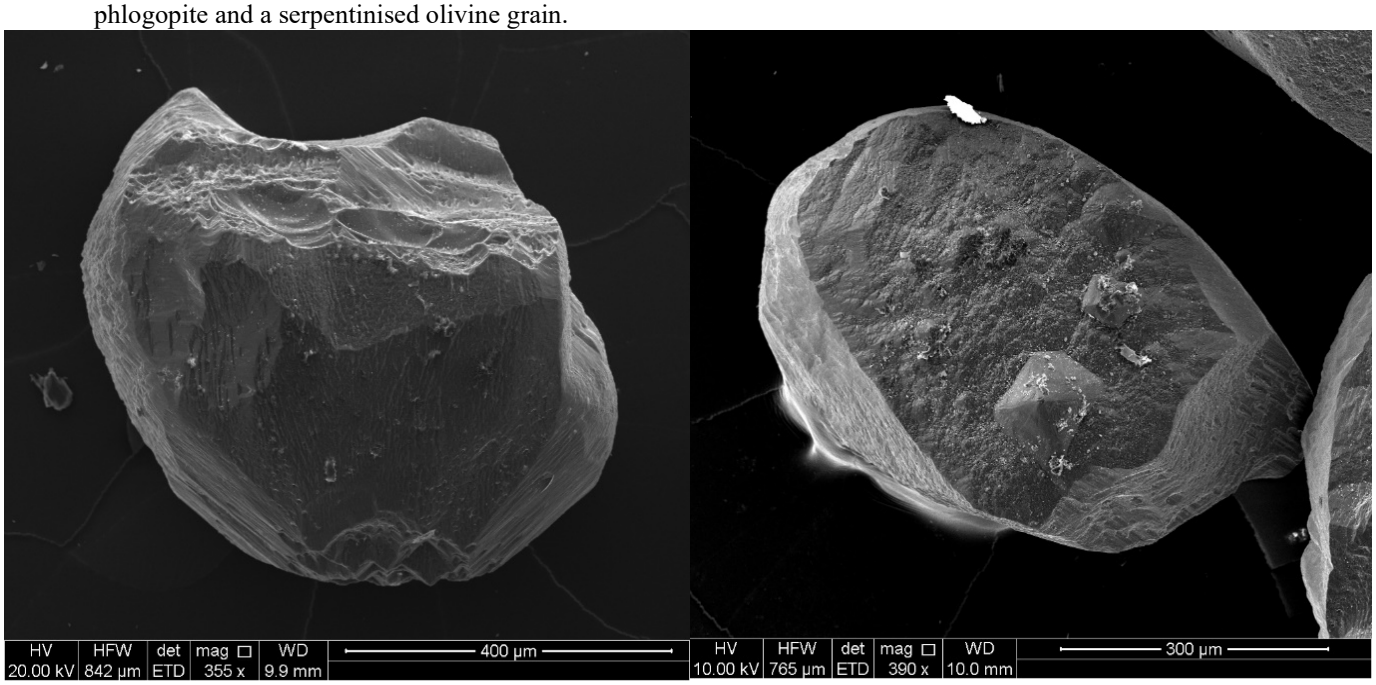

Figure 7*:* BSE images from MB060(1) grain mount, showing rounded forsteritic olivines, right image shows a euhedral forsterite crystal growing from the main crystal mass.

3.1.8 MB068 126-136m - Forsteritic Marble

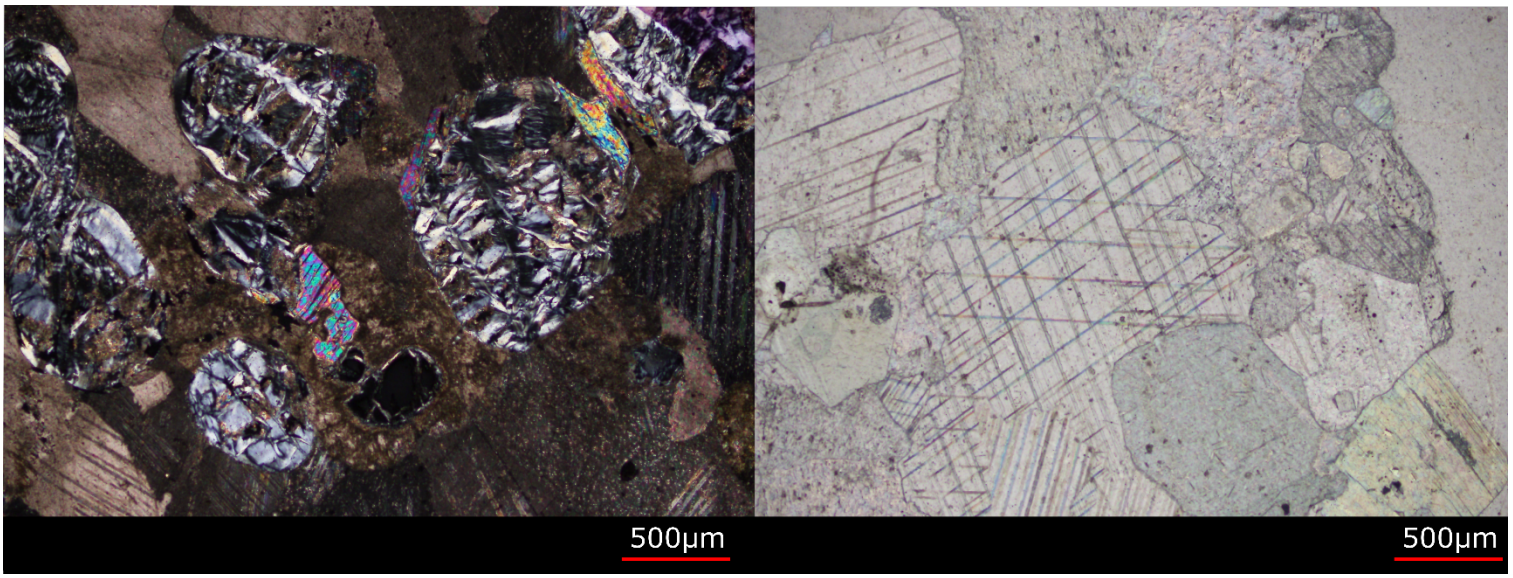

Figure 8: Carbonate from MB 068 126-136m in the forsteritic marble showing altered calcite on the left with serpentinised forsterite grains, which are being rimmed by phlogopite. The right image shows strong internal calcite twinning in unaltered grains which have a different trace element concentration.

APPENDIX 3: SUPPLEMENTARY PARAGENETIC REPORT

PARAGENETIC INTERPRETATION – DERIVED VIA PETROLOGICAL INVESTIGATION OF 9 SAMPLES FROM DRILL HOLES DD88LR19, DD88LR20 AND DD89LR21, MOUNT BRADY, SOUTH AUSTRALIA

Dr R. G. Taylor
BSc (Hons), D.I.C., PhD, M.A.I.G.

AUGUST 2019

roger-taylor@bigpond.com
c/o 15 Burns Street, Invermay, Launceston, Tasmania, 7248

This work was commissioned for SIMEC Mining by Dr. Richard Lilly to compliment the 2019 honours project being completed through the University of Adelaide. The author extends gratitude to Graham Teale (Teale and Associates) for the access to the slides, which had previously been held in personal collection. All petrology and observations completed by Roger Taylor. This report has been prepared with formatting assistance by Richard Lilly.

Table 1: Sample List

Hole ID	Depth	Notes
DD88LR19	**171.6**	'Felsic', fine-grained, red-rock alteration, cpx and magnetite
DD88LR20	**120.2**	Skarn assemblage, cpx, phlog and magnetite (coarse grained)
DD88LR20	**165.2**	Skarn assemblage, magnetite, minor cpx plus sulphide (v. coarse grained)
DD88LR20	**230.9**	Skarn assemblage, cpx and magnetite (coarse grained)
DD88LR20	**261.3**	Skarn assemblage, cpx and magnetite (coarse grained)
DD88LR20	**270.8**	Skarn assemblage, cpx and magnetite (coarse grained)
DD89LR21	**113**	Skarn assemblage, cpx and magnetite (coarse grained)
DD89LR21	**122.3**	Forsterite marble
DD89LR21	**242**	Skarn assemblage; phlog, mag and cpx

PARAGENETIC SUMMARY

With relatively few samples the following should be viewed as provisional.

Bearing in mind the internationally available information concerning general skarn paragenisis (see related Skarn Discussion Report, Roger Taylor, 2019), the above samples are interpreted to represent deposit paragenisis as:

Early

Forsterite* ± minor garnet ± phlogopite
Pyroxene ± phlogopite
Magnetite
Chalcopyrite
Pyrite± carbonate
Hematite-carbonate

] Possibly Overlapping

Late

Carbonate

(Origin of Forsterite requires more field data concerning regional setting, See discussion)*

PARAGENETIC DISCUSSION

The earliest stage is present as forsterite (variably serpentinised) and garnet (as seen in DD88LR21-122.30m) and as forsterite (variably serpentinised) ± phlogopite (as seen in DD88LR20-120.12m). The olivine (presumed forsterite) dominant samples are assessed as high temperature products and within the current data confines are a little difficult to interpret.

Forsterite skarns are widely reported as regional metamorphic products of impure dolomites in high temperature terrains, but are less widely present in more localised magmatic hydrothermal skarn systems.

The distinction here is difficult as the pyroxene and later magnetite, with their overprinting characteristics and coarse grain size are consistent with a ***magmatic skarn development***.

The question becomes; what is the distribution of the early forsterite containing material? Regional or local (and what is the regional metamorphic grade)?

However, ***the remaining system appears to be a relatively standard magnesium style skarn.***

There are no clear relationships between the later abundant pyroxene and the forsterite, but in all skarn paragenetic sequences, pyroxene is an early stage and is usually closely associated with garnet.

The magnetite clearly postdates the pyroxene and phlogopite with numerous overprinting examples, and magnetite reaches 40-50% In DD88LR20-230.90m.

Magnetite alteration is widespread.

Regardless of the origin of the forsteritic materials the sequence from pyroxene onward is consistent with development of a magnesium skarn system culminating in localised chalcopyrite mineralisation. Including minor pyrite ± trace chalcopyrite observed in late fractures in DD88LR20-120.20m and DD88LR20-165.20m. The minor pyrite(?) and chalcopyrite recorded in DD88LR20-120.20m - could relate to the pyrite stage recorded above, and clearly more samples are required to refine the interpreted paragenesis proposed by this report.

The skarn materials do not seem to be severely deformed, although their relationship to the overall geological environment is not discernible from the limited samples available.

The alkali feldspar syenite sample (with hydrothermal overtones), DD88LR19-171.6, is of interest as a possible magmatic link, but needs to be assessed in geological context to allow discussion.

Specimen DD88LR19 - 171.60m: Alkali Feldspar Syenite

Tripartate divisions of slide:

1. Fine grained (400 microns) composed of K-feldspar-amphibole-magnetite (plus trace albite). Many unusual textures; albite saturated K-feldspars, K-feldspars with globular albite blebs, unusual looking perthitic patches. A single minute discontinuous irregular stringer of pyrite is observed in this area

2. Coarse grained K feldspar zone (6.0mm) with trace amphibole and magnetite. Perthitic and sutured albite textures, K-feldspars have sutured crystal contacts. Hint of UST texture (need to see hand specimen).

3. As 2 above, slightly finer with increased amphibole and magnetite. The amphiboles are very altered, and one has prominent blue green colour-probe work required for details.

The rock is highly fractionated-with textures indicating possible links to hydrothermal fluid generation.

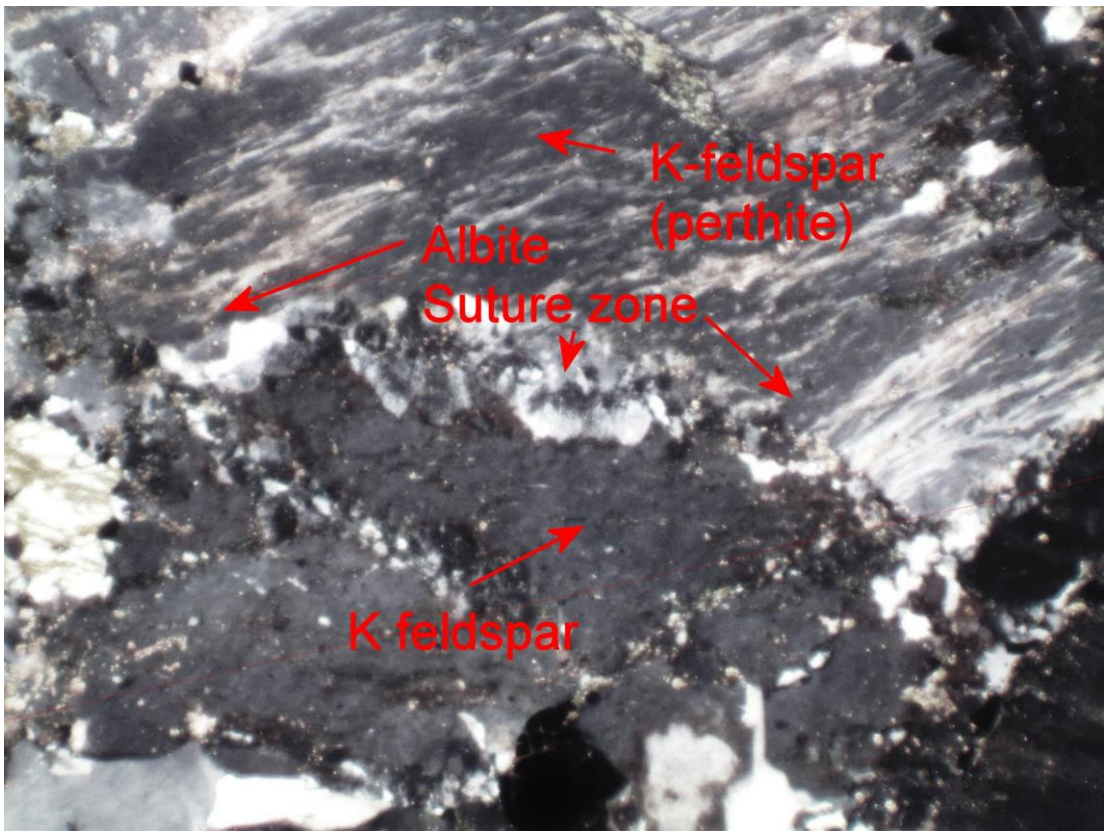

Figure 1. DD88LR19-171.60m. Perthitic K feldspar and albite along junction of K-feldspars. WOF 2.2mm. Crossed Nicols (CN)

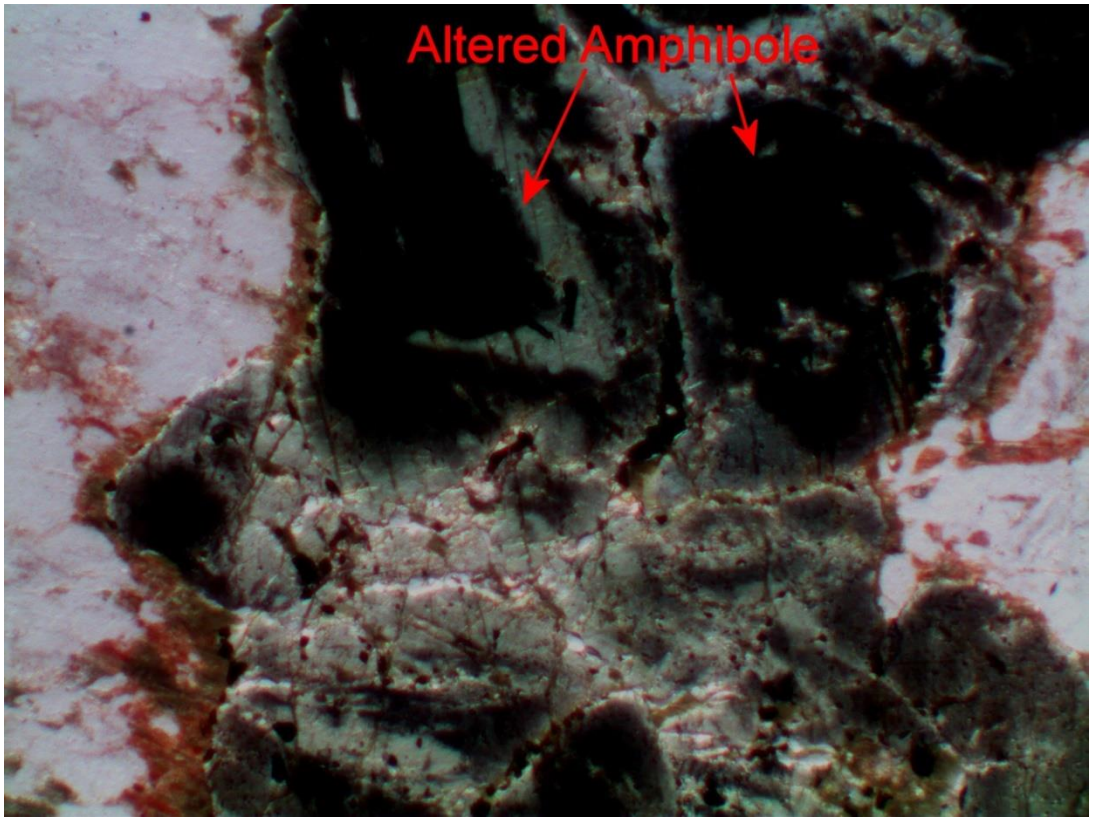

Figure 2. DD88LR19-171.60m. Altered amphibole. WOF 2.2mm. Ordinary light (OL)

Specimen DD88LR20-120.2m: Forsterite phlogopite skarn

Composition:

- Serpentine; minor olivine (forsterite) remaining **50-60%**
- Carbonate **20-30%**
- Phlogopite **20-30%**
- Magnetite (irregular spots, discontinuous veinlets and alteration of host carbonate and phlogopite host minerals) **5-7%**
- Pyrite **<1%**
- Chalcopyrite **Trace**

Interpreted paragenesis for DD88LR20-120.2m:

Early	Forsterite –phlogopite
	Magnetite
Late	Pyrite ± chalcopyrite

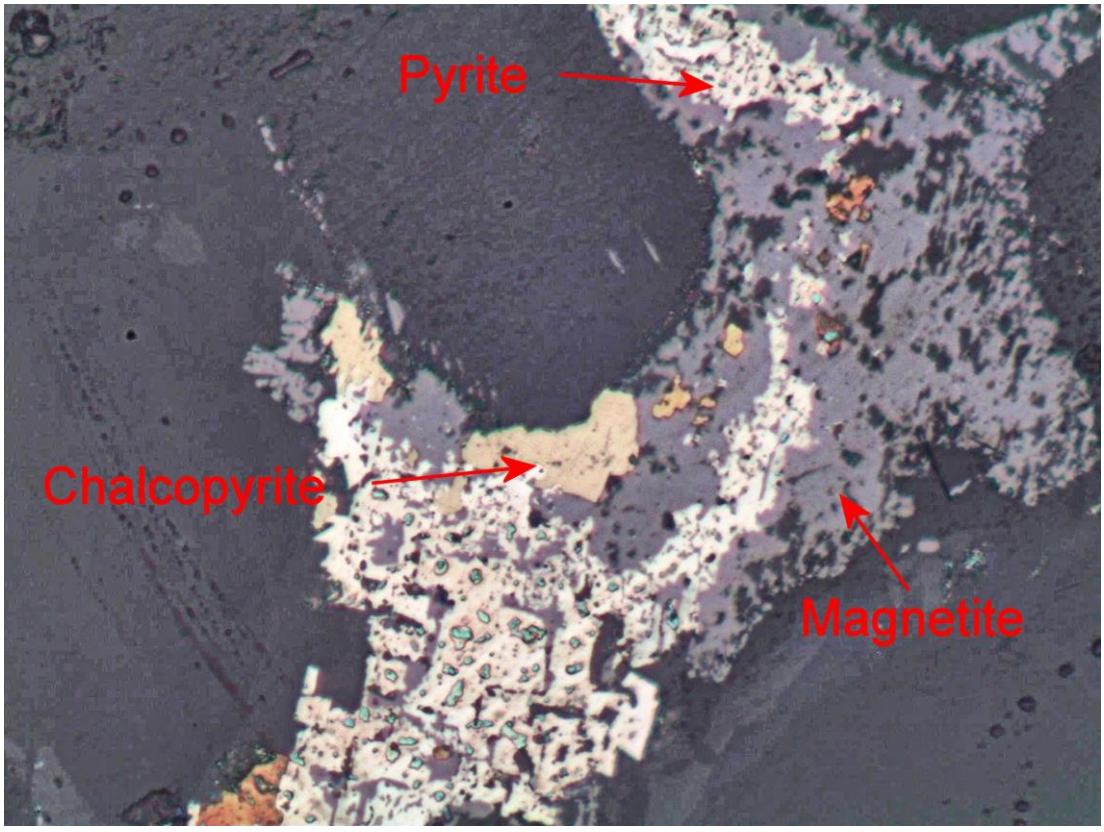

Figure 3. DD88LR20-120.2m. Pyrite and chalcopyrite. WOF 200 microns. Polished section (PS). Reflected Light (RL)

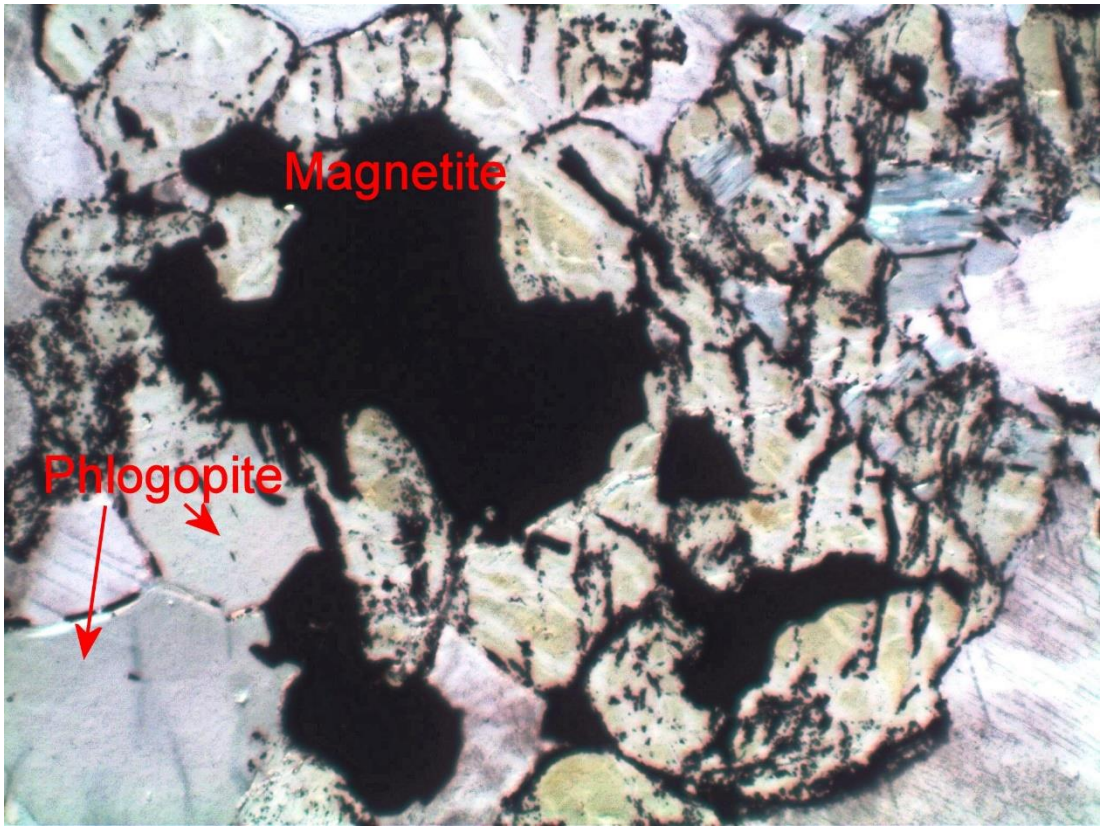

Figure 4. DD88LR20-120.20m. Magnetite replacing phlogopite. WOF 2.2mm Ordinary light(OL).

Specimen DD88LR20 – 165.2m

It is the interpretation of the author slide DD88LR20 -165.2m records:-

Early

1. Magnetite - both as infill of big vugs, and as small irregular to rounded alteration grains in host rock

Minor fracture

2. Chalcopyrite cuts/brecciates magnetite in many places –irregular blebs small in host carbonate may be alteration. Some small blebs are disaggregated magnetite - chalcopyrite fragments and alteration spots tend to have curvy rounded outlines

Minor fracture

3. Pyrite ± carbonate – veins with good infill and lots of alteration spotting in host carbonate patches –seem to also alter chalcopyrite in places. The veins often have carbonate centres and some late heamatite crystals in the carbonate (Possibly minor chalcopyrite?).

Continuing fracture whilst forming to allow (4)

4. Hematite carbonate infill stingers; continuation of the above as the pyrite veins fill and then some late crackle gives cracks with hematite – carbonate ± very minor pyrite. *(Figure 12)*

Minor fracture

5. Carbonate simple infill vein

Limonite spots (weathering)

Late

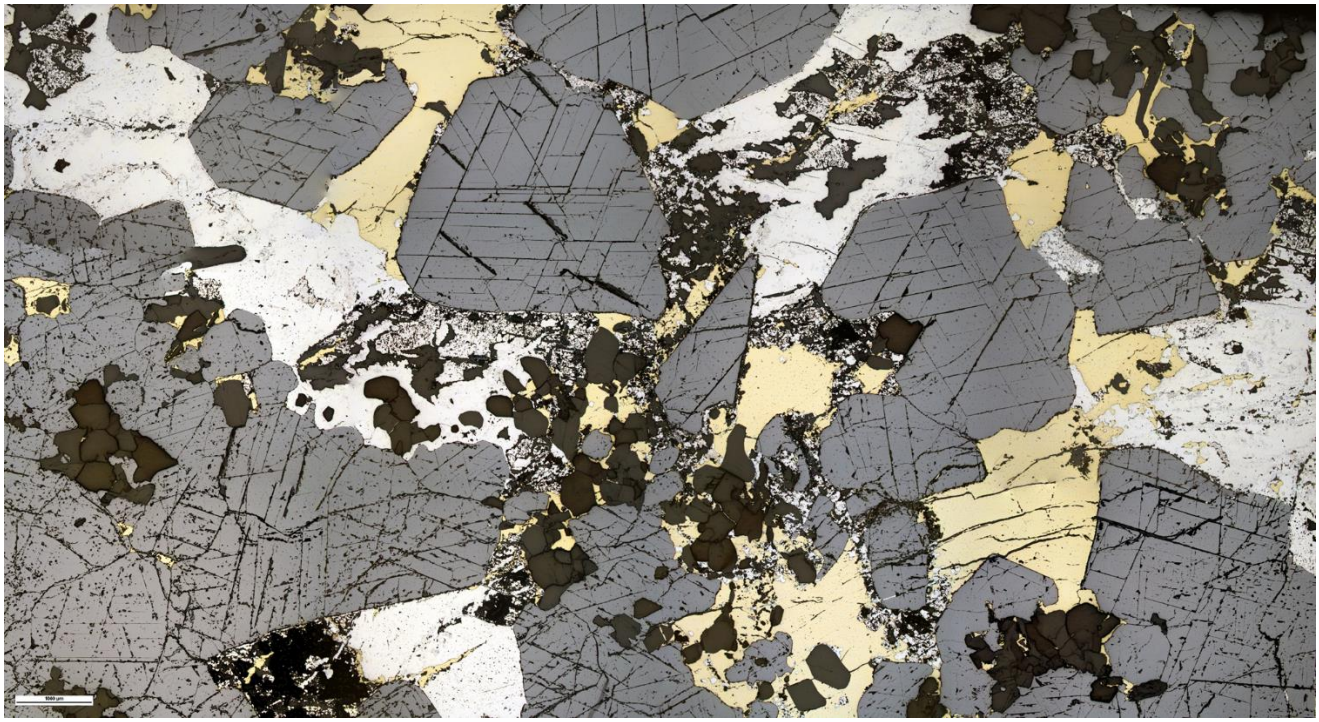

Figure 5. DD88LR20 – 165.2m. Obvious vug infill with magnetite - note the magnetite growing off the host rock fragments(black) in the bottom right corner. Image by Martin Hand.

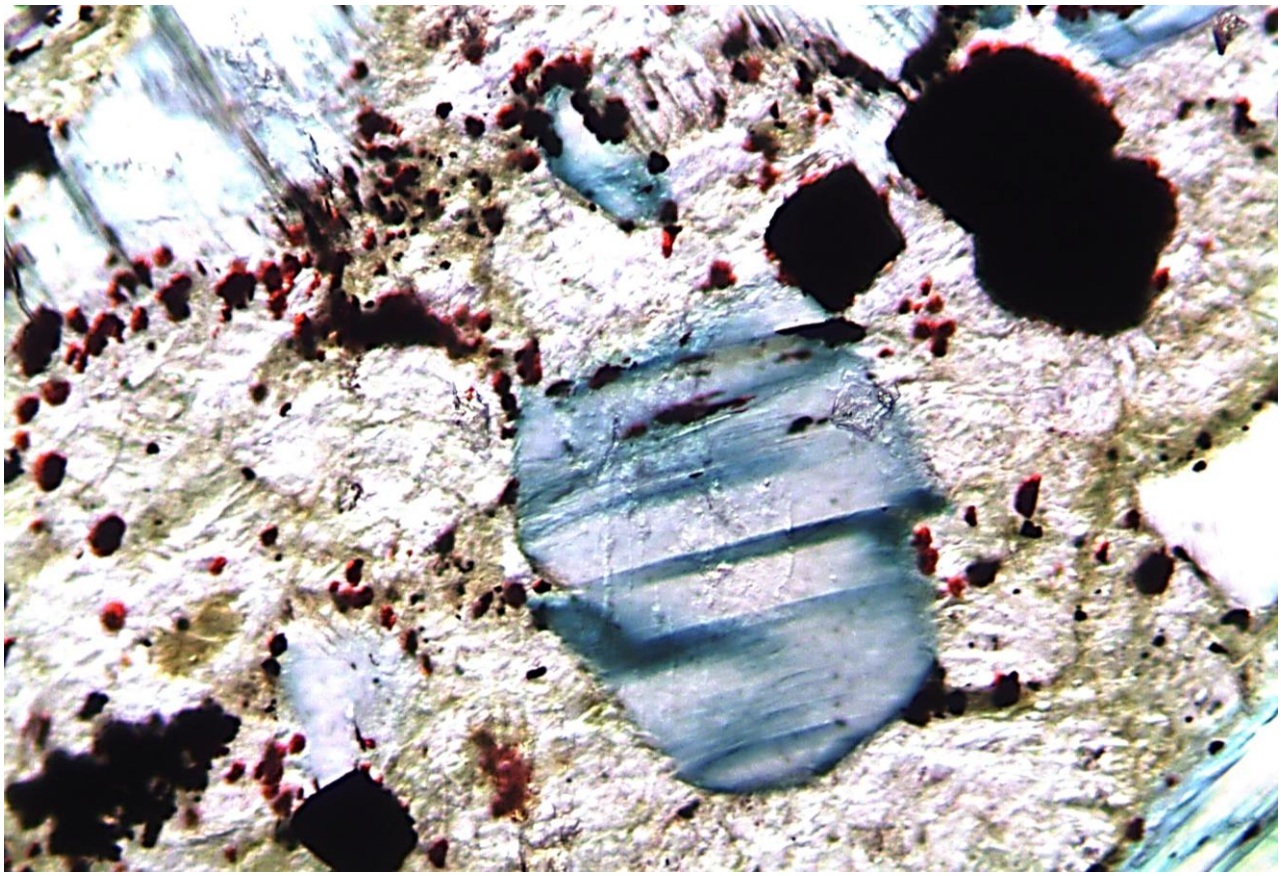

Figure 6. DD88LR20 – 165.2m. Host rock with suspected phlogopite and carbonate. Note magnetite alteration spots – compare with the crystals in Figure 5. Minor limonite also present (weathering). WOF 820 microns.

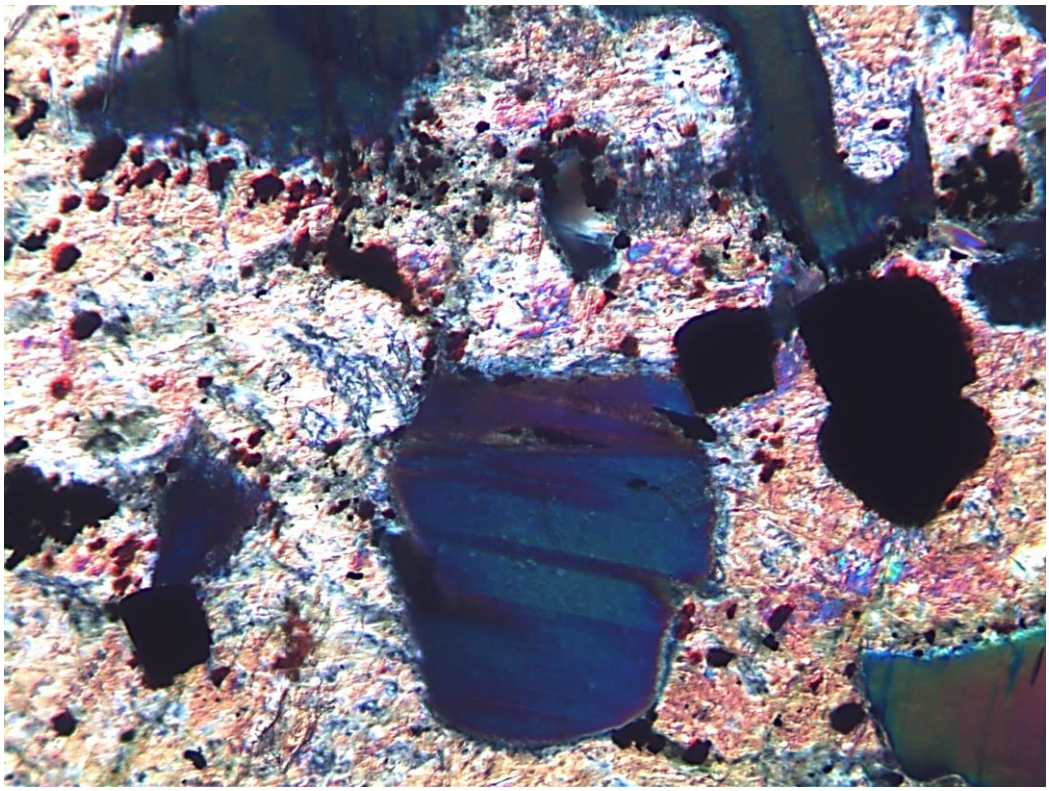

Figure 7. DD88LR20 – 165.2m. Phlogopite (blue) and carbonate (?)(coloured). Same field of view as Figure 6 with crossed nicols. WOF 820 microns.

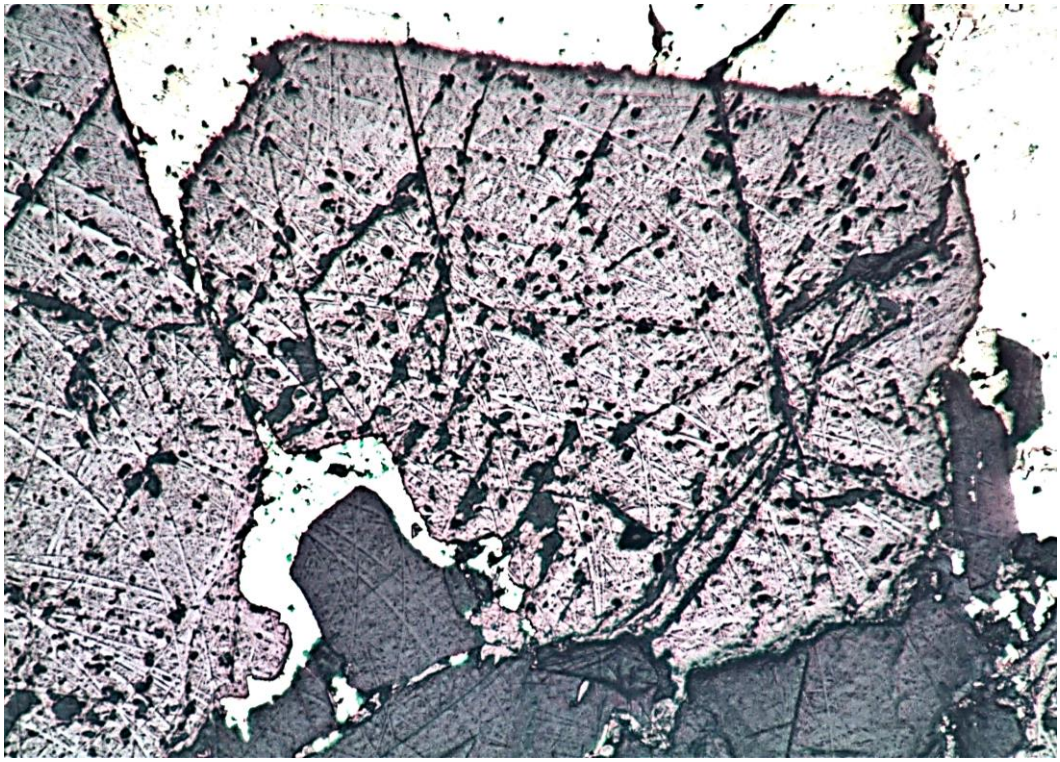

Figure 8. DD88LR20 – 165.2m. Stage 1 magnetite, centre of image, growing off fragment of host rock, with Stage 2 chalcopyrite (pale/white) crosscutting at left. WOF 2.2 mm.

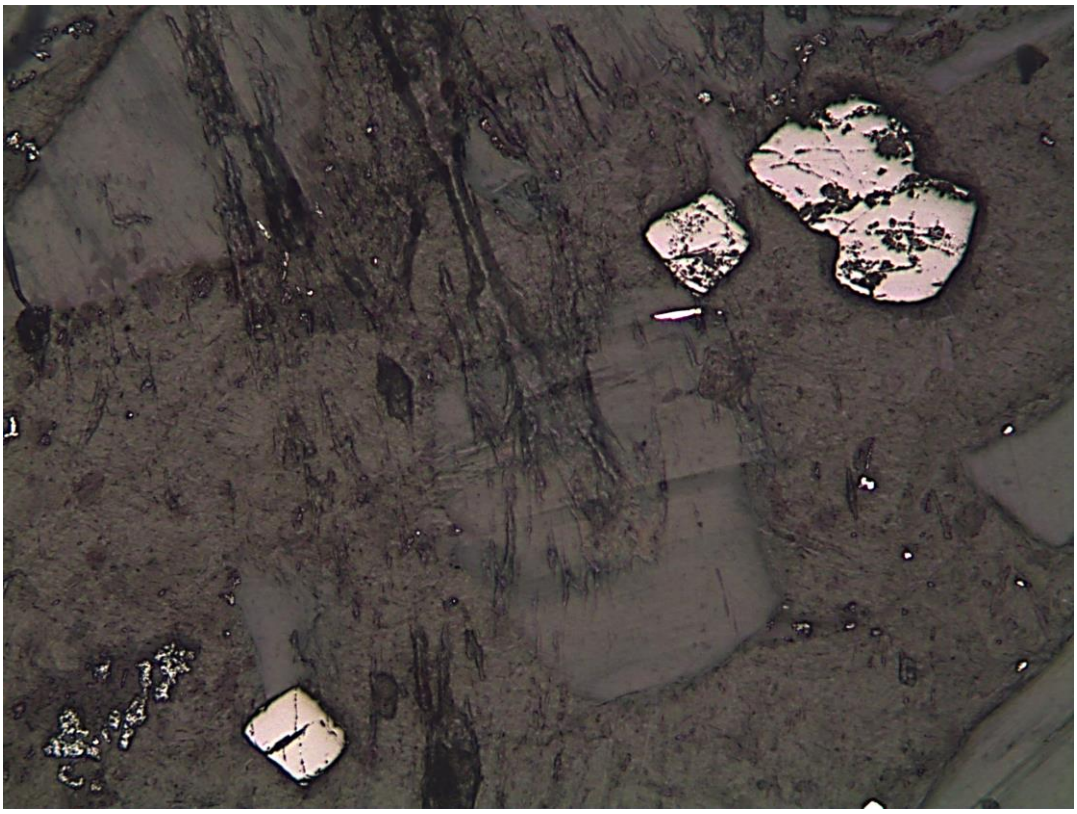

Figure 9. DD88LR20 – 165.2m. Magnetite alteration spots in host rock – carbonate. see Figure 5-6. WOf 2.2mm.

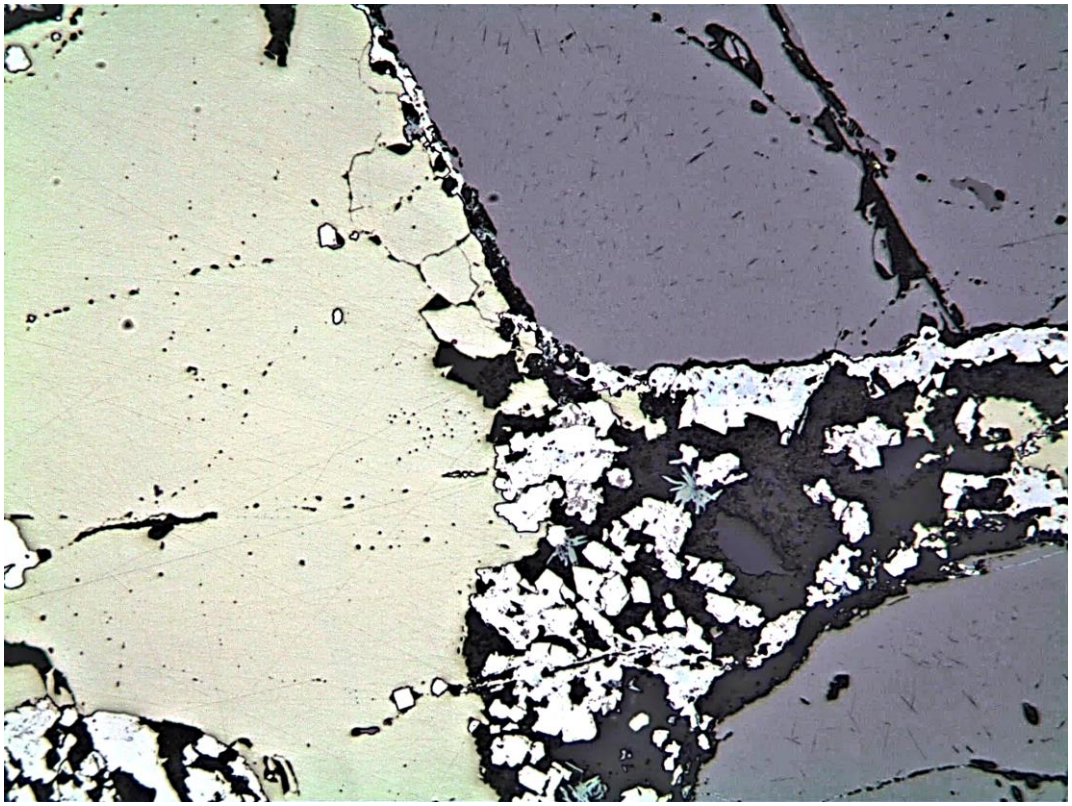

Figure 10. DD88LR20 – 165.2m. Stage 4 Vein Infill of pyrite- carbonate - hematite. Chalcopyrite at left, magnetite at right(grey).

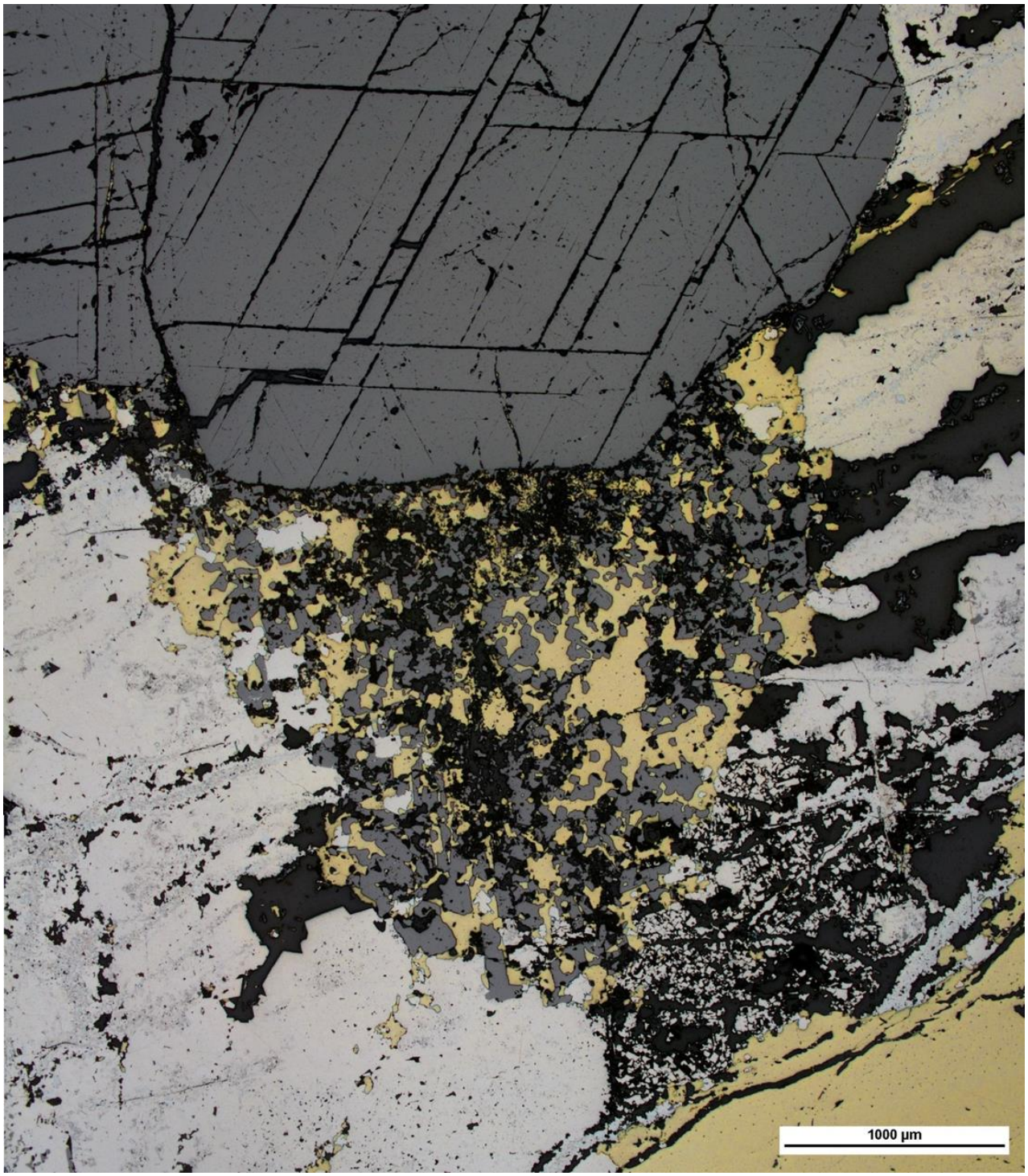

Figure 11. DD88LR20 – 165.2m. Fine grained magnetite in centre of image was initially interpreted as secondary magnetite. I would suggest the small magnetite grains are alteration spots formed originally in the host rock (See Figures 1, 2, 3). Subsequent chalcopyrite takes out the rest of the host rock to give the unusual chalcopyrite-magnetite assemblage. Pyrite alters any remaining rock. Image by Martin Hand.

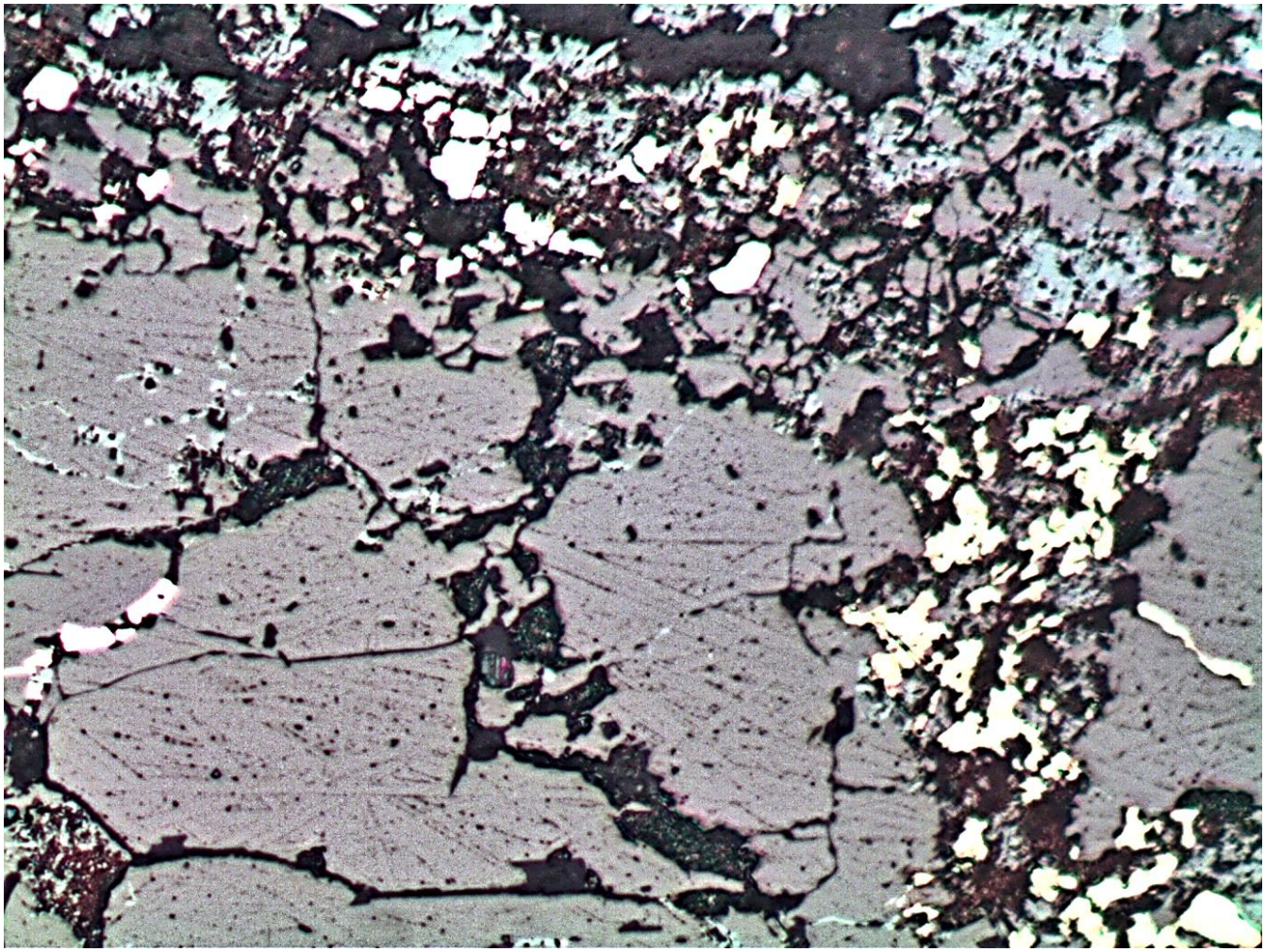

Figure 12. DD88LR20 – 165.2m. Two breccias; magnetite cut by chalcopyrite (lower right, yellow) then re-brecciated and overprinted by Stage 3/4 hematite (upper parts of image, blue), carbonate (black) and pyrite (white).

Figure 13. DD88LR20 – 165.2m. Stage 4-5 hematite crystals (acicular, grey) pyrite (white), chalcopyrite (pale yellow). WOF 200 microns Note the shapes, with reference to Figures 14 and 15.

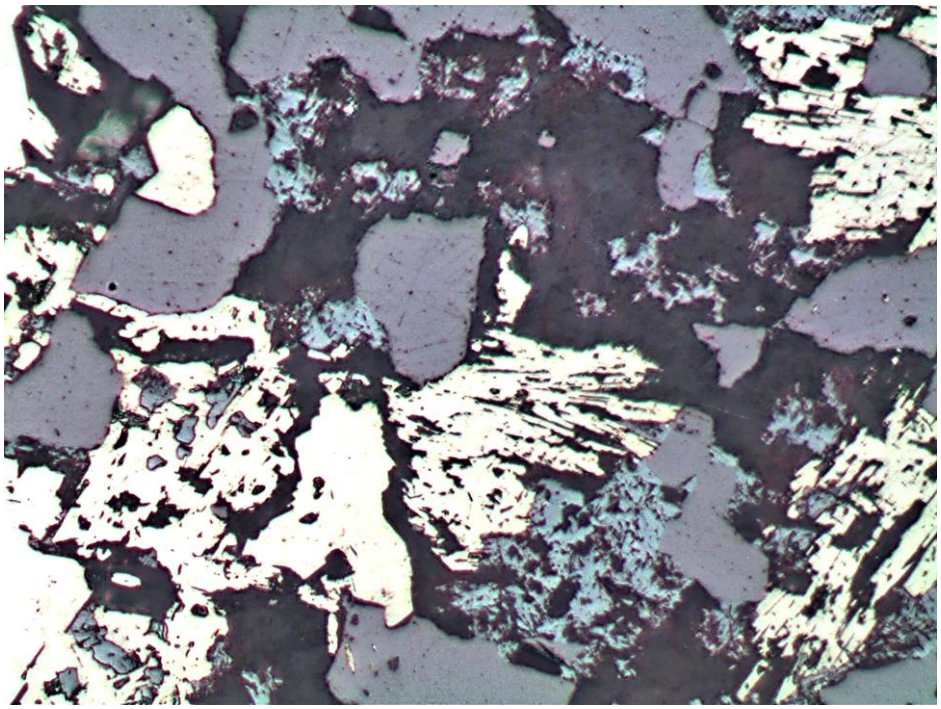

Figure 14. DD88LR20 – 165.2m. The slightly prismatic chalcopyrite (yellow) in this frame has been previously interpreted to be chalcopyrite pseudomorphing hematite. However, the shape is not the same as the usual hematite (Figure 12-13-15) and the hematite observed here (blue) is much smaller. There are also numerous place on the slide where cpy occurs with heamatite with no signs of replacement. (Note: the acicular textured chalcopyrite is restricted to a very small area of the slide)

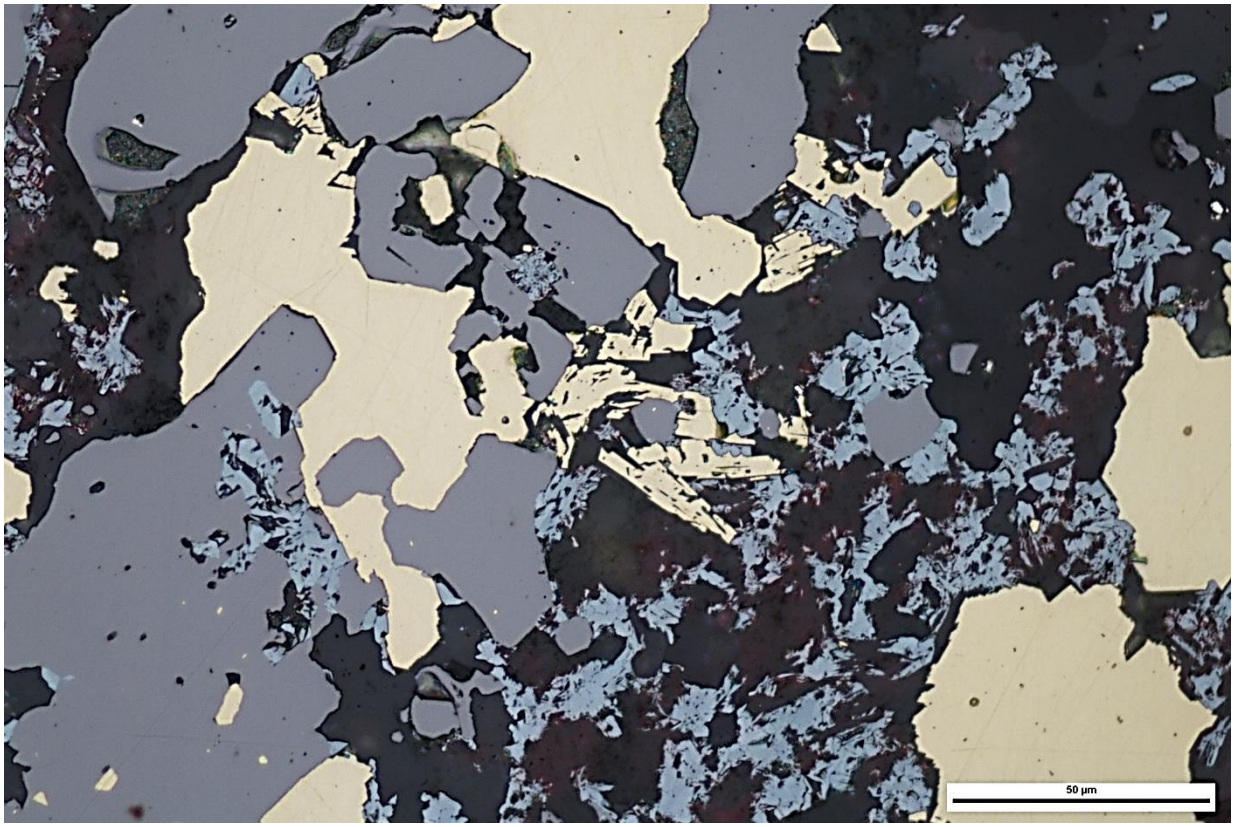

Figure 15. DD88LR20 – 165.2m. Another image of the unusual shaped chalcopyrite (centre of image). Given the size and shape of the (blue) hematite crystals surrounding it, the chalcopyrite seems too big and the wrong shape to be pseudomorphing the hematite. Image by Martin Hand.

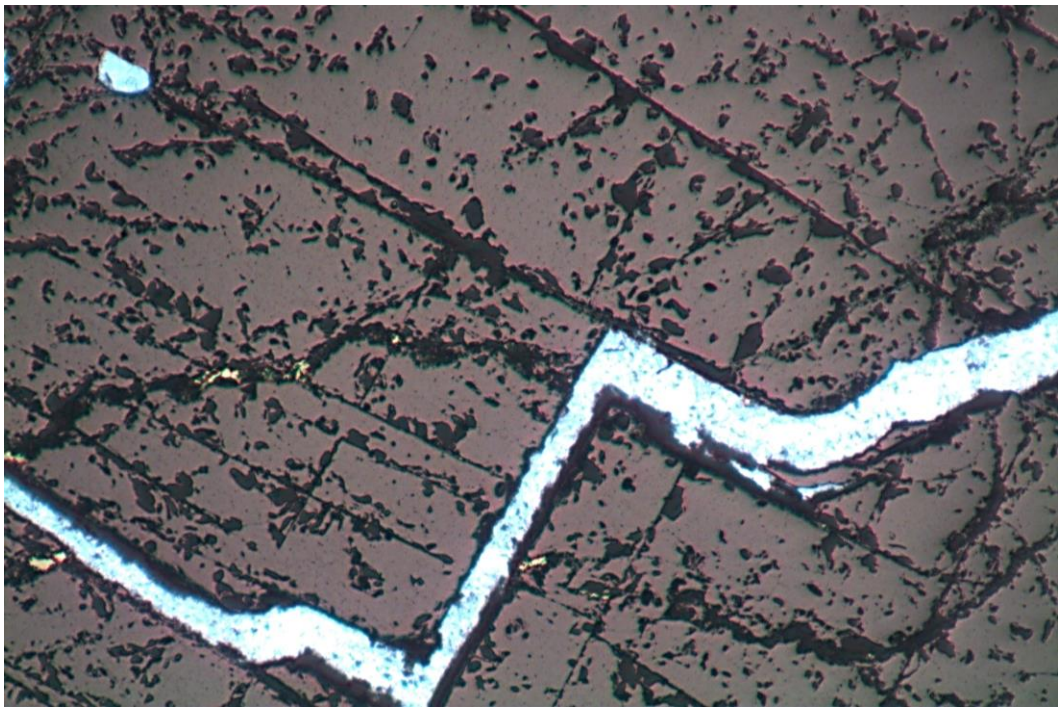
Figure 16. DD88LR20 – 165.2m. Stage 6, carbonate vein cuts magnetite WOF 2.2mm

Specimen DD88LR20-230.90m: Magnetite-pyroxene skarn

Composition:

• Magnetite -	Main cluster of grains is c10x20mm.	40-50%
• Phlogopite -	Cut by magnetite	
	Unusual green blue alteration	20-30%
• Pyroxene -	Some large crystals (6.0mm) (vug?)	
	Some magnetite alteration spots	20-30%
• Carbonate		~15%

Notes:
- Magnetite-overprints host minerals
- Minor blue green alteration of phlogopite?
- No images were collected from this sample as relationships are equally well illustrated in other samples.

Specimen DD88LR20-261.3m: Pyroxene-magnetite skarn

Composition:

• Phlogopite		30-40 %
• Carbonate -	Size variation (some recrystallisation?)	20-30 %
• Pyroxene -	Cracked with carbonate infill strings	20-30 %
• Magnetite -	Cracked: mostly irregular shapes	
	Disseminated: some sub crystalline shapes	
	Alteration spots in pyx and phlogopite	10-15%

Notes:
- Magnetite overprints all other minerals (alteration "spot" style)
- No images were collected from this sample as relationships are equally well illustrated in other samples.

Specimen DD88LR20-270.8m:
Magnetite-pyroxene skarn

Composition:

- Magnetite – Vaguely defined network of irregularly bordered grains/patches. Blebs of magnetite within phlogopite and along cleavage in pyroxene. ~50%
- Pyroxene - Some large grains have crystal shapes – possible vug infill, with magnetite surrounding pyx crystals (?) 20-30%
- Phlogopite 15-20%
- Carbonate ~3%

Notes:
- Magnetite alteration of host minerals—magnetite is post pyroxene
- Late carbonate veinlets.

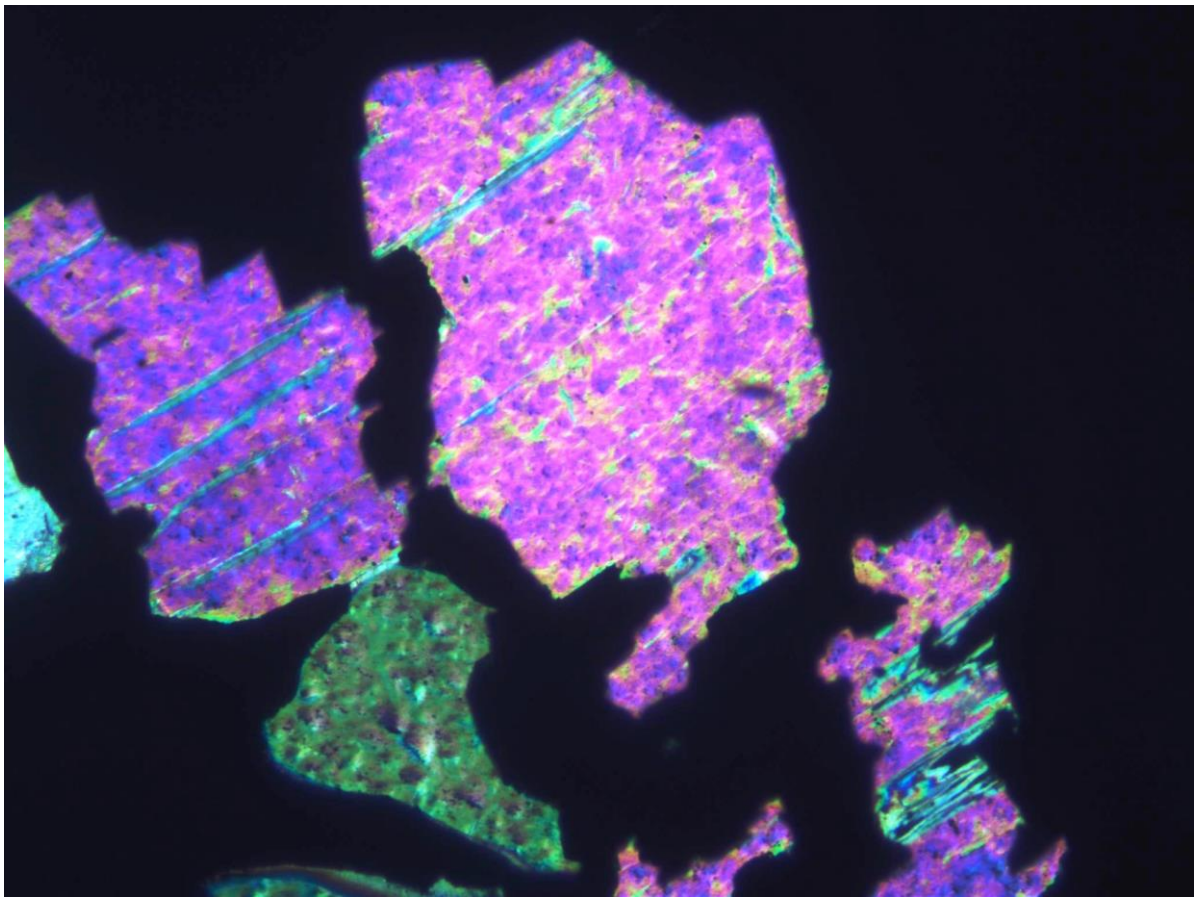

Figure 17. DD88LR20-270.8m. Pyroxene (disco coloured) cut and replaced by magnetite (dark). WOF 820 microns CN.

Specimen DD88LR21-113.00m:
Magnetite pyroxene skarn

Composition:

- Phlogopite - abundant-unusual order extinction in places, result of alteration (?). Minor indication of scapolite could be section preparation (could be checked with ion probe if thought significant) 40-50%
- Magnetite - abundant – irregular bordered discontinuous veins and blebs. Alteration blebs in pyroxene and observed replacing phlogopite 20-30%
- Pyroxene 20-30%
- Pyrite - irregular blebs and subhedral crystals replaces carbonate and phlogopite with alteration spots in pyroxene. Very tarnished slide – could be checked after repolish ~5%
- Carbonate - late stringer vein Trace
- Carbonate-host rock

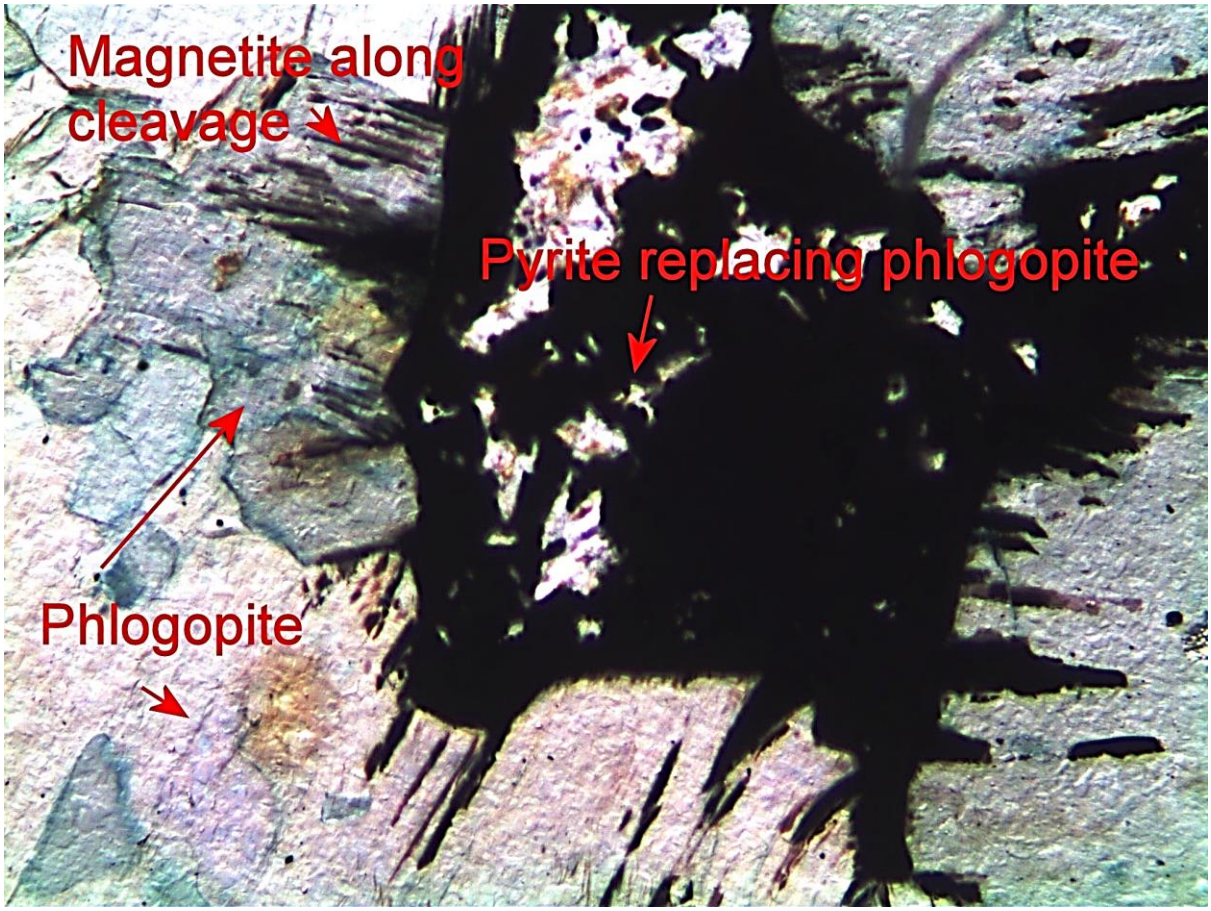

Figure 18. DD88LR21-113.00m. Pyrite and magnetite alteration of phlogopite (see also Figure 19). WOF 820 microns. OL.

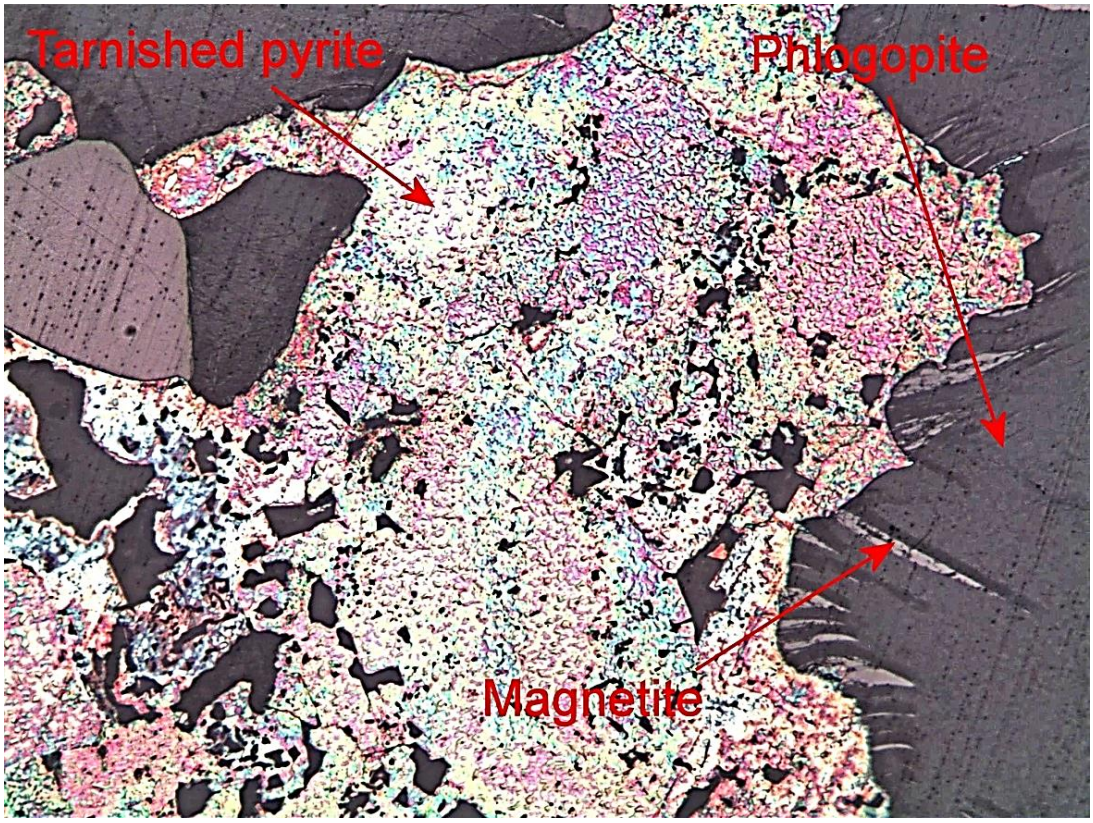

Figure 19. DD88LR21-113.00m. Tarnished pyrite around magnetite. Note relatively early magnetite along cleavage in phlogopite. Polished section (PS). RL. WOF 820microns (See also Figure 18).

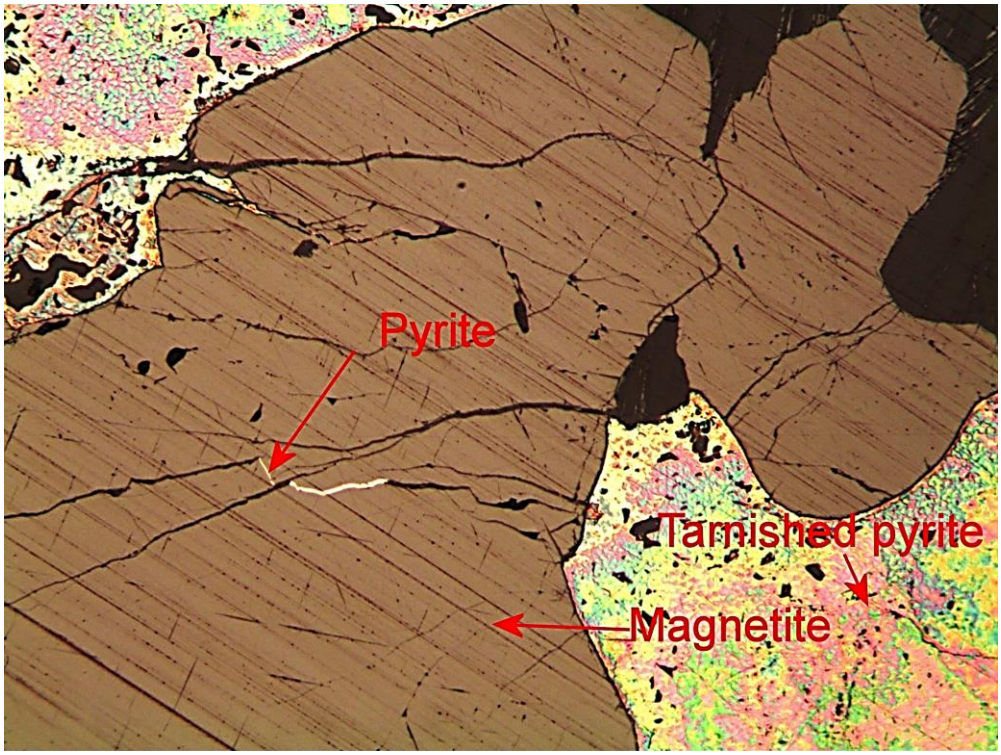

Figure 20. DD88LR21-113.00m. Magnetite with overprinting pyrite (tarnished) WOF 820microns. PS. RL.

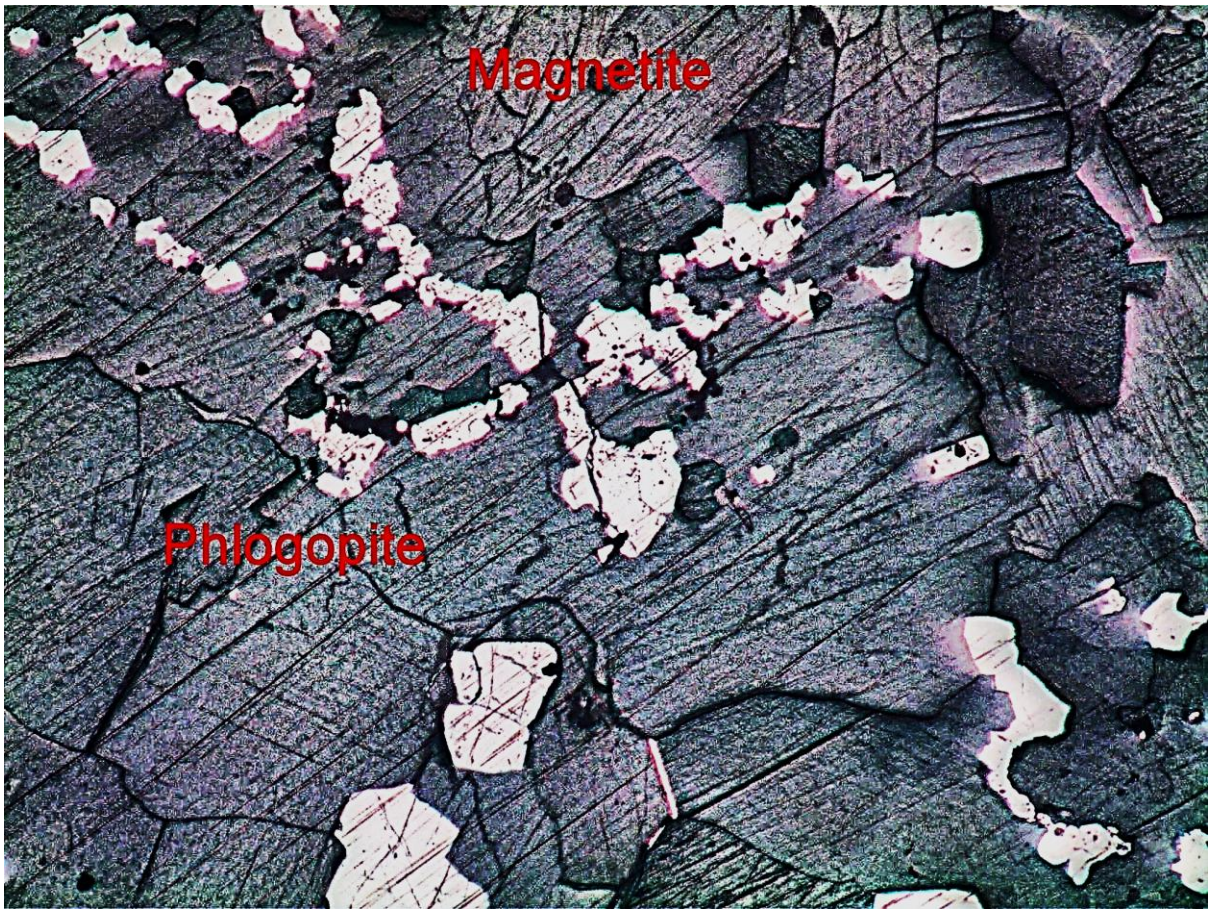

Figure 21. DD88LR20-113.0m. Magnetite overprinting phlogopite. WOF 2.2mm PS. RL

Specimen DD89LR21-122.30m
Forsterite (?) garnet carbonate skarn

Composition:

- Olivine (mostly serpentinised-suspected forsterite, but requires probe/geochemical confirmation of olivine species) 45-50%
- Carbonate 45-50%
- Garnet 2-3%
- Minor limonite with flecks of haematite Trace

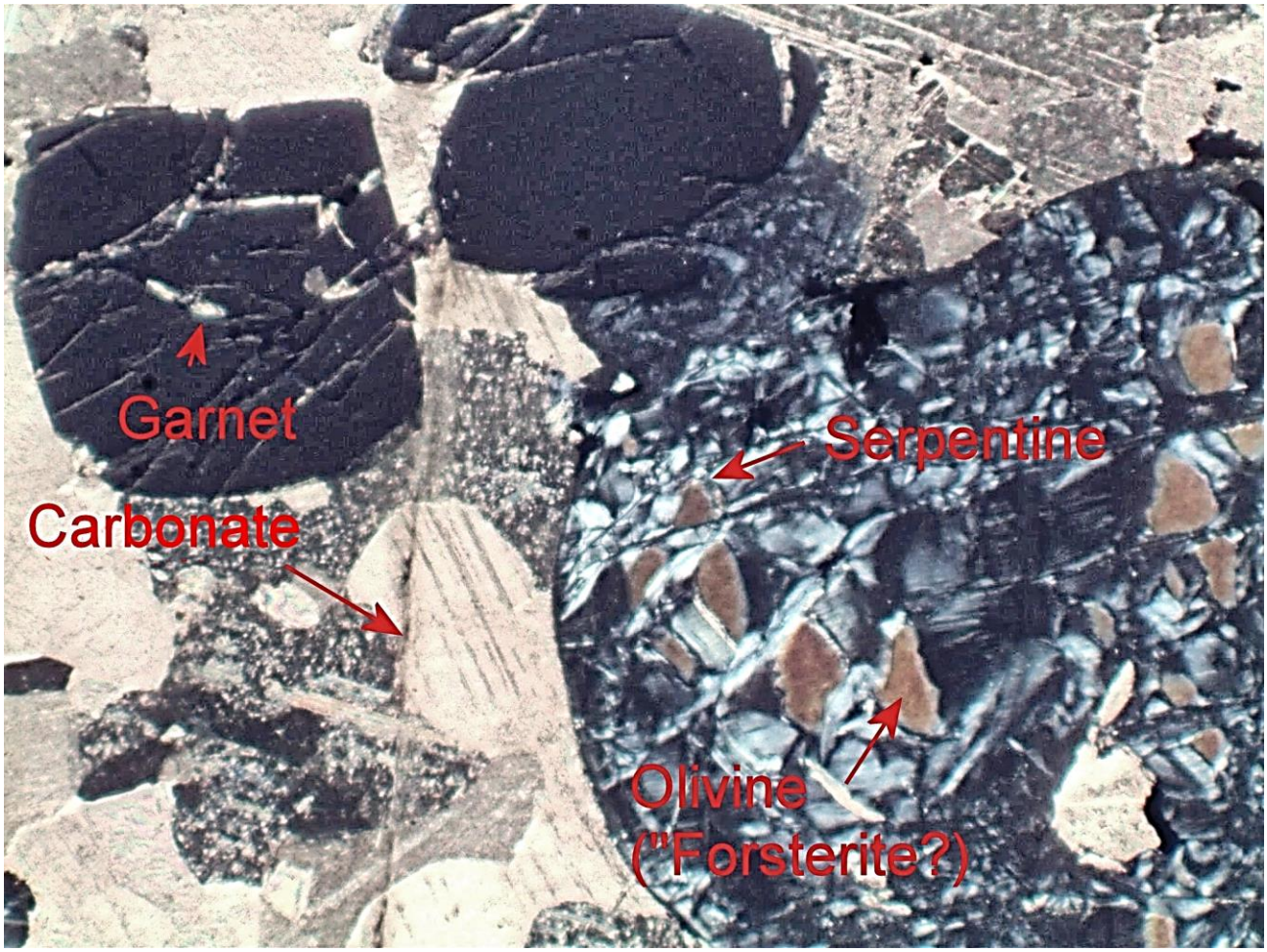

Figure 22. DD89LR21-122.30m. Olivine (forsterite?) with garnet in carbonate matrix. WOF 820 microns. Crossed nicols(CN).

Specimen DD89LR 21 242.00m
Gabbro (altered)

Composition:

- Plagioclase ± sericite alteration
- Pyroxene ± chlorite alteration, ± rutile, also minor sericite.
- Accessory magnetite-± hematite alteration
- Apatite –Trace
- Rutile -Trace as accessory

Also – discontinuous pyrite veinlet,1-3µm wide

Notes:
- Relative timing of sericite and chlorite alteration difficult to assess.
- Pyrite appears to be late
- No images were collected from this sample.

APPENDIX 4: GEOCHEMISTRY

Full geochemical analyses embedded as an .xlsx file.

APPENDIX 5: GEOCHRONOLOGY

Full geochronology measurements embedded as an .xlsx file.

Table 1: Summary of data points removed during signal processing in IOLITE. The main causes of bad data are inclusions or mineral misclassification.

Spot	Mineral	Reason
C1 MB031 - 3	Apatite	Lack of P signal
C1 MB031 - 101	Apatite	Lack of P signal
C1 MB031 - 103	Apatite	Lack of P signal
C1 MB031 - 9	Apatite	Lack of P signal
C1 MB031 - 87	Apatite	Lack of P signal
C1 MB031 - 88	Apatite	Lack of P signal
C1 MB031 - 89	Apatite	Lack of P signal
C2 MB031 - 14	Apatite	Highly variable P - potential inclusions
C2 MB031 - 29	Apatite	Highly variable P - potential inclusions
C2 MB031 - 75	Apatite	Highly variable P - potential inclusions
C2 MB031 - 89	Apatite	Highly variable P - potential inclusions
C2 MB031 - 97	Apatite	Highly variable P - potential inclusions
C2 MB031 - 103	Apatite	Highly variable P - potential inclusions
C2 MB031 - 106	Apatite	Highly variable P - potential inclusions
C2 MB031 - 108	Apatite	Highly variable P - potential inclusions
C1 MB063 - 23	Apatite	Lack of P signal
C1 MB063 - 24	Apatite	Lack of P signal
C1 MB063 - 42	Apatite	Lack of P signal
C2 MB063 - 1	Apatite	Lack of P signal
C2 MB063 - 3	Apatite	Lack of P signal
C2 MB063 - 4	Apatite	Lack of P signal
C2 MB063 - 5	Apatite	Lack of P signal
C2 MB063 - 7	Apatite	Lack of P signal
C2 MB063 - 9	Apatite	Lack of P signal
C2 MB063 - 14	Apatite	Lack of P signal
C5 MB063 - 9	Apatite	Lack of P signal
C5 MB063 - 10	Apatite	Lack of P signal
C5 MB063 - 11	Apatite	Lack of P signal
C5 MB063 - 33	Apatite	Lack of P signal
C5 MB063 - 38	Apatite	Lack of P signal
C5 MB063 - 39	Apatite	Lack of P signal
C5 MB063 - 58	Apatite	Lack of P signal
C5 MB063 - 64	Apatite	Lack of P signal
C5 MB063 - 66	Apatite	Lack of P signal
zircon - 29	Zircon	Large ^{204}Pb signal
zircon - 63	Zircon	Large ^{204}Pb signal
zircon - 53	Zircon	Large ^{204}Pb signal, large silica spike
zircon - 54	Zircon	Final 207/235 and 206/238 age signals are highly oscillatory
zircon - 76	Zircon	Signal drop-off
zircon - 73	Zircon	Inclusion or migration through different zoning
zircon - 38	Zircon	Large ^{204}Pb signal
zircon - 30	Zircon	Analysis quarantined, anomalously high REE (14,083 ppm compared to < 1000 for most analyses)

Table 2: Zircon grain descriptions, MM = Metamict, BR = Bright Rim, LL = Light Linear Zonation, DL = Dark Linear Zonation, OC = Oscillatory Core, PC = Patchy core.

Grain #	Spot #		Textural Description	Additional Notes	Textural Classification
	Core	Rim			
1	1	2	Patchy mildly metamict core with minor preserved oscillatory zoning	Bright rim, dark core	MM, BR
2	3, 4	-	Light linear zones separated by narrow dark lines	Very bright grain, darker lamellae	LL, LL
3	5, 6		Light linear zones separated by narrow dark lines	Well defined boundaries between lineations, linear zones ~ 25µm wide	LL, LL
4	7		Oscillatory core, minor bright rim	Small very bright inclusions	OC
5	8, 9		Oscillatory core	Bight paching along apparent fractures in core	OC, OC
6	10		Oscillatory core	Acicular crystal, dark patch through crystal interrupts oscillatory zoning	OC
7	11	12	Oscillatory core with a bright rim then further oscillatory overgrowth	Crystal has a central defect separating the darker core and brighter 'rim' type zircon that has replaced the old core material	OC, BR
8	14, 15	13	Bright oscillatory core which gets gradually darker with growth, dark rim.	Dark rim on oscillatory core is followed by a bright rim	DR, OC, OC
9	16, 17, 18		Oscillatory core with bright rim, dark zone at contact between bright rim and core	Good crystal preservation, small patchy bright spots within core. 18 overlaps the dark zone.	OC, OC, OC
10	19, 20		Structureless zircon, may be metamict.	Small dark inclusion avoided; inclusion is surrounded by a bright CL patch	MM, MM
11	21	22	Dark oscillatory core overgrown by a dark structureless rim	Small bright patches where the dark rim contacts the core	OC, DR
12	23, 24		Dark oscillatory core with a narrow bright rim	Missing fragment of the crystal has a bright border- possibly the site of an inclusion prior to crushing	OC, OC
13	26	25	Dark oscillatory core with a dark rim, apparent recrystallisation texture	Dark rim followed by a bright rim with fractures visible.	DR, OC
14	27		Structureless dark fragment with narrow light lamella	Tabular shape	DL
15	28		Oscillatory core	Small grain	OC
~~**16**~~	29		Oscillatory core	Grain too small, signal deleted	~~OC~~
17	30		Oscillatory core	Minor metamictisation?	OC
18	31		Structureless dark grain	Narrow line with small round bright patches	DL

Grain #	Spot #		Textural Description	Additional Notes	Textural Classification
19	32	33	Dark oscillatory core overgrowth by dark rim	Dark rim is not of uniform thickness and has a cauliflower texture.	OC, DR
20	34, 35		Dark and light linear zones	Internal dark patch, potentially a recrystallisation texture	DL, DL
21	36		Dark oscillatory core	Internal line of bright spots, minor bright spotting at core boundary,	OC
22	37	~~38~~	Slightly metamict core with subtle oscillatory zoning still present, darker 'rim'	Rim signal deleted for high 204Pb	OC, ~~DR~~
23	39, 40		Patchy texture with wavy light and dark zones	Similar appearance to 'DL/LL' classification	DL, LL
24	41	42	Dark scrambled interior texture, possibly slightly metamict, dark rim followed by further oscillatory zoning	Dark 'rim' is possibly a recrystallisation texture as it occurs where two fractures meet, this zircon has several internal fractures.	PC, DR
25	44	43	Dark oscillatory core with brighter recrystallisation/ overgrowth. Thick bright rim on one side of the grain	Narrow bright patches all around the rim of this crystal	OC, BR
26	45		Dark structureless crystal with discontinuous bright patching/rimming	Narrow bright lamella inside crystal	DL
27	46		Partially recrystallised core with small remnant oscillatory zoning, thin discontinuous bright rim	Targeted the patchy recrystallised zone	PC
28	47, 48		Dark oscillatory core	Oscillatory zoning gets darker with growth	OC, OC
29	49	50	Structureless core, possibly metamict bright rim	Bright rim has a darker area cross cutting it, this may be compositional variation or an SEM artifact	MM, BR
30	51		Dark oscillatory core with a bright rim	-	OC
31	52, ~~53~~		Patchy texture	Spot 52 is on a light patchy zone, 53 was removed due to high ^{204}Pb	PC, ~~PC~~
~~**32**~~	~~54~~		Structureless dark crystal with narrow discontinuous bright rim	Spot removed due to an unreliable signal	~~MM~~
33	56	55	Patchy core with a thick bright rim	-	BR, PC
34	57	58	Patchy recrystallised(?) core with a dark rim	-	PC, DR
35	59		Patchy core with screw disclocation (?)	This analysis may represent different zones due to small zone size and overlap	PC
36	60		Weakly patchy core with small dark zones and a bright rim	Possibly metamict or recrystallised	PC
37	61		Structureless grain with wavy darker/brighter zones	Similar to the appearance of DL/LL zircons	DL
38	62		recrystallised texture metamict (?) with a darker core surrounded by a structureless lighter rim	This analysis may cross a compositional boundary	MM

Grain #	Spot #		Textural Description	Additional Notes	Textural Classification
39	64	63	Dark oscillatory core with a thick discontinuous dark 'rim'. Recrystallisation or metamictisation at terminal end of the crystal	-	OC, DR
40	65		Dark metamict core with a darker rim.	Strongly fractured	MM
41	66		Light/dark linear zones	Spot located on the bright zone	LL
42	67		Well preserved oscillatory zoning, minor bright patches inclusions (?) along a lattice dislocation	-	OC
43	69	68	Oscillatory core with a bright rim	Core shows minor recrystallisation, spot hits the non-recrystallised area	OC, BR
44	70		Similar appearance to DL/LL grains, possibly metamictised, has a wavy interior structure	Bright patch at one end and an asymmetric narrow dark rim	DL
45	71		Possibly slightly metamict core or recrystallised with an oscillatory overgrowth rim	-	MM
46	~~72,~~ 73		Stubby dark crystal with bright interior zone	The bright patch is likely an SEM artefact, the reflected light image shows a crystal defect in this area	~~DL~~, DL
47	74		Oscillatory core with dark patchy texture possibly from recrystallisation	The recrystallised areas are rimmed by further oscillatory zoning	PC
48	75, ~~76~~		Patchy core with wavy light and dark zones surrounded by oscillatory zoning	Spot 76 removed due to bad signal	PC, ~~PC~~
49	77, 78		Patchy recrystallised (?) core with a lighter rim overgrowth	Spot sampled a fraction of the lighter rim and caught the edge of the core – may produce mixed signal	PC, PC
50	79		Dark structureless grain	Bright rim where the grain is damaged, possibly just an SEM artefact	DL
51	80		Dark oscillatory core	Well preserved	OC
52	82	81	Dark oscillatory core with a lighter fractured rim	Rim is strongly fractured	OC/MM, BR
53	83		Oscillatory and slightly recrystallised core, darker 'rim' which is also oscillatory	-	OC
54	84, 85		DL/LL type grain with a lighter recrystallised area	Fractured. Similar to grain 48.	PC, DL
55	86		Dark oscillatory grain, core appears patchy, re-crystallised (?)	Small grain	PC
~~**56**~~	~~87~~		Patchy recrystallised core with a brighter rim	Small grain	~~PC~~
57	88	89	Minorly recrystallised oscillatory zoned core with a bright rim	Core spot is located on a dark recrystallised (?) area	DL, BR

Grain #	Spot #		Textural Description	Additional Notes	Textural Classification
58	90, 91		Dark core with darker recrystallised area (?) and a narrow bright rim	Grain has some poorly preserved oscillatory zoning but has recrystallisation textures in the core	PC, PC
59	92		Bright elongate grain	Appears to have linear brighter/darker zones	LL
60	93		Dark recrystallised zone within an otherwise oscillatory zoned grain	-	PC
61	94		Elongate structureless dark grain	-	DL
62	95		Elongate structureless dark grain	-	DL
63	96		Dark central zone in an elongate grain	Fragmented grain	DL
64	97		Metamict(?) dark structureless core	-	MM
65	98		Dark oscillatory core	-	OC
66	99		Recrystallised core	-	PC
67	101	100	Dark recrystallised core with a brighter rim	-	PC, BR
68	102		Dark recrystallised core with some relict oscillatory zoning	Spot is on the dark recrystallised zone	PC
69	103		Dark recrystallised core with some relict oscillatory zoning	-	PC

Table 3: Calculated isotopic ratio ages, % discordance, associated error, and textural characteristics for each zircon analysis. MM = Metamict, BR = Bright Rims, LL = Light Linear Zonation, OC = Oscillatory Core, DR = Dark Rims, DL = Dark Linear Zonation, PC = Patchy Core, $\sigma_{\bar{x}}$ = Standard Error. T.conc = Concordia age (Vermeesch 2018).

Grain #	Analysis #	$^{207}Pb/^{235}Pb$	$^{207/235}$ $\sigma_{\bar{x}}$	$^{206}Pb/^{238}Pb$	$^{206/238}$ $\sigma_{\bar{x}}$	$^{207}Pb/^{206}Pb$	$^{207/206}$ $\sigma_{\bar{x}}$	T.Conc	conc $\sigma_{\bar{x}}$	Discordance	Core/Rim	Texture
1	1	767.5	42.5	624.95	4.97	1208	159	628.83	4.81	51.8	C	MM
	2	1708.1	67.2	1678.4	14.9	1745	154	1680.9	13.5	96.2	R	BR
2	3	1641.2	64.5	1559	16.2	1748	145	1562.3	16	89.7	C	LL
	4	1620.9	61	1603.4	15.1	1644	147	1605.3	13.2	98.2	C	LL
3	5	1682	65.4	1661	14.4	1708	149	1662.3	13.8	98.0	C	LL
	6	1664	64.5	1625	11	1713	149	1627.3	10.2	95.7	C	LL
4	8	1660.4	64.2	1591.87	5.54	1748	145	1593.37	5.33	91.2	C	OC
	9	1665.3	63.3	1608.46	7.79	1738	146	1611.84	6.63	92.6	C	OC
5	10	1644.9	64.3	1569.16	8.59	1743	146	1571	8.43	90.1	C	OC
6	11	1551	63.5	1426.09	7.75	1726	148	1428.36	7.65	82.9	C	OC
	12	1610.4	62.3	1480.1	13.3	1785	142	1484.9	13.1	83.1	R	BR
7	14	1730.5	64.6	1707.65	7.17	1758	144	1708.45	6.78	97.3	C	OC
	15	1695.7	66.1	1679.89	9.44	1715	149	1680.33	9.25	98.1	C	OC
	13	1383	56.7	1195.7	11.8	1685	143	1206.3	11.2	71.0	R	DR
8	16	1568.6	62.3	1447.24	8.5	1736	147	1452.77	7.9	83.4	C	OC
	17	1625.1	63.7	1565.63	8.6	1703	150	1569.51	7.3	92.0	C	OC
	18	1210.5	57.4	1025.9	11.8	1557	146	1019.1	11.7	65.9	C	OC
9	19	1612	61	1568.66	9.1	1669	144	1571.42	8.06	93.6	C	MM
	20	1571	66.8	1593.4	11.8	1541	157	1592.8	11.7	102.8	C	MM
10	21	1495.4	62.6	1505.68	7.15	1481	153	1505.39	6.91	101.9	C	OC
	22	1474.4	62.5	1492.9	11.8	1448	157	1491.8	11	103.2	R	DR
11	23	1524.7	58.1	1582.3	10.8	1446	147	1576.91	9.19	109.5	C	OC
	24	1169.2	53.5	1069.16	9.28	1360	155	1076.1	8.31	78.3	C	OC

Grain #	Analysis #	$^{207}Pb/^{235}Pb$	$^{207/235}\sigma_{\bar{x}}$	$^{206}Pb/^{238}Pb$	$^{206/238}\sigma_{\bar{x}}$	$^{207}Pb/^{206}Pb$	$^{207/206}\sigma_{\bar{x}}$	T.Conc	conc $\sigma_{\bar{x}}$	Discordance	Core/Rim	Texture
12	26	1556.6	62.3	1581.79	6.05	1523	149	1581.11	5.81	104.1	C	OC
13	27	1559.2	60.4	1572.7	8.33	1541	147	1571.8	7.15	101.7	C	DL
14	28	1560.3	61.9	1587.84	7.05	1523	149	1586.76	6.61	104.3	C	OC
15	30	479.7	31.3	396.88	3.03	898	164	395.14	2.96	44.2	C	OC
16	31	1576.8	60.5	1590.36	8.06	1559	146	1589.59	7.23	101.8	C	DL
17	32	1586.1	61	1602.43	7.54	1564	145	1601.75	7.07	102.6	C	OC
	33	1437.8	59.4	1371.6	7.82	1537	148	1373.84	7.52	89.4	R	DR
18	34	1559.8	65	1547.9	7.35	1576	154	1548.14	7.24	98.6	C	DL
	35	1601.8	65.8	1560.6	11.1	1656	155	1562.7	10.5	94.4	C	DL
19	36	1586.6	65.2	1588.84	8.06	1584	153	1588.8	7.95	100.6	C	OC
20	37	1644.5	64.6	1675.92	7.7	1605	151	1674.56	7.16	104.6	C	OC
21	39	1595.4	63.1	1601.4	11.3	1587	152	1600.94	9.89	100.4	C	DL
	40	1592.3	64.2	1597.4	11.3	1586	153	1597.1	10.7	100.8	C	LL
22	41	1258.9	58.5	1147.86	7.82	1454	156	1150.61	7.67	79.1	C	PC
	42	1335.4	60.6	1232.01	8.52	1505	151	1229.88	8.43	81.8	R	DR
23	44	1175	54.1	992.25	7.74	1529	149	997.15	7.57	64.7	C	OC
	43	1627.2	63.9	1623.01	9.77	1633	148	1623.15	9.54	99.7	R	BR
24	45	1612.4	64.8	1566.6	15.9	1673	153	1570.4	14.8	94.6	C	DL
25	46	1190.4	60.2	1049.47	6.85	1456	166	1053.38	6.6	72.1	C	PC
26	47	1585.7	60.8	1535.72	9.4	1653	146	1539.27	8.12	93.1	C	OC
	48	1015.6	54.8	858.2	10.4	1373	154	848.01	9.84	62.1	C	OC
27	49	1634	61.6	1605.45	7.29	1671	144	1606.97	6.39	96.1	C	MM
	50	1701.7	68.6	1689.3	23.3	1717	149	1689.8	23.2	99.2	R	BR
28	51	1641.8	61.7	1599.92	6.79	1696	142	1601.27	6.46	94.5	C	OC
29	52	1605.7	61.5	1541.82	6.6	1691	142	1543.49	6.38	91.2	C	PC

Grain #	Analysis #	$^{207}Pb/^{235}Pb$	$^{207/235}\sigma_{\bar{x}}$	$^{206}Pb/^{238}Pb$	$^{206/238}\sigma_{\bar{x}}$	$^{207}Pb/^{206}Pb$	$^{207/206}\sigma_{\bar{x}}$	T.Conc	conc $\sigma_{\bar{x}}$	Discordance	Core/Rim	Texture
30	56	1621.2	61.1	1569.67	7.33	1689	142	1572.03	6.69	92.8	C	PC
	55	1383.7	60.8	1191.42	9.38	1694	151	1197.3	9.15	70.2	R	BR
31	57	1305	62.8	1129.5	18.7	1606	151	1123.2	18.6	70.3	C	PC
	58	653.5	39.6	517.58	5.95	1156	164	519.92	5.91	44.9	R	DR
32	59	1598	62	1543.34	6.6	1671	144	1544.77	6.37	92.4	C	PC
33	60	1666.6	64.5	1695.3	20.1	1631	148	1692.8	19.2	104.1	C	PC
34	61	1553.9	60.5	1570.7	10.6	1531	148	1569.39	9.38	102.9	C	DL
35	62	1506.4	61.1	1501.6	7.92	1513	150	1501.81	7.37	99.1	C	MM
36	64	1261.7	55.9	1168.3	11.6	1425	149	1171.1	11.4	82.1	C	OC
	63	576.7	34.7	518.76	4.46	812	158	516.27	4.22	63.9	R	DR
37	65	1494	63.5	1516.39	9.17	1462	155	1515.83	9.03	103.8	C	MM
38	66	1576.5	65.3	1578.3	11.9	1574	154	1578.2	11.6	100.6	C	LL
39	67	1566.5	58.8	1576.7	12.9	1553	146	1575.6	10.6	102.1	C	OC
40	69	1515	61.7	1512.82	8.92	1518	150	1512.9	8.66	99.6	C	OC
	68	934.9	46.2	799.83	5.41	1268	153	805.87	4.9	62.5	R	BR
41	70	1580.6	62.3	1588.3	12.8	1570	154	1587.5	10.3	101.4	C	DL
42	71	1565.5	62.9	1580.78	8.83	1545	147	1580.78	8.83	101.7	C	MM
43	73	1569.2	61.9	1572.7	19.4	1564	155	1572.2	16.4	101.4	C	DL
44	74	1484	60.1	1449.81	8.49	1533	148	1451.31	8.03	94.2	C	PC
45	75	1565	61.7	1582.79	5.8	1541	147	1582.29	5.52	102.6	C	PC
46	77	1584.7	64.7	1572.7	6.06	1601	151	1572.84	6.01	98.3	C	PC
	78	1568.1	60.1	1572.2	9.09	1563	145	1571.94	8.24	100.8	C	PC
47	79	1571.2	63.9	1566.1	12.1	1578	153	1566.4	11.4	98.1	C	DL
48	80	911.8	52.3	777	12.6	1254	154	764.4	11.7	61.8	C	OC

Grain #	Analysis #	$^{207}Pb/^{235}Pb$	$^{207/235}\sigma_{\bar{x}}$	$^{206}Pb/^{238}Pb$	$^{206/238}\sigma_{\bar{x}}$	$^{207}Pb/^{206}Pb$	$^{207/206}\sigma_{\bar{x}}$	T.Conc	conc $\sigma_{\bar{x}}$	Discordance	Core/Rim	Texture
49	82	1496.7	60.8	1500.07	6.9	1492	152	1499.86	5.6	100.4	C	OC
	81	1563.3	59.1	1569.7	11.1	1555	146	1569.06	9.25	101.4	R	BR
50	83	1493.2	63.4	1506.19	9.19	1475	154	1505.96	9.11	102.2	C	OC
51	85	1553.6	63.7	1596.9	11.1	1495	152	1595.7	10.9	107.0	C	DL
	84	1344.7	56.4	1287.16	6.34	1437	147	1289.3	5.93	89.8	C	PC
52	86	1362.9	56.7	1319.81	5.52	1431	148	1321.69	4.85	92.0	C	PC
53	88	1552.4	62.9	1593.38	5.79	1497	152	1592.14	5.47	106.6	C	DL
	89	1492.1	60.7	1508.7	11.2	1469	155	1507.18	9.35	102.9	R	BR
54	90	1484.7	61.1	1497.5	10.7	1467	155	1496.48	9.35	102.0	C	PC
	91	956.6	50.4	838.44	5.09	1239	156	835.77	4.96	67.7	C	PC
55	92	1580.6	66	1588.3	14.6	1570	154	1588.1	14.4	100.8	C	LL
56	93	1532.7	61.6	1563.1	10.1	1491	152	1560.96	9.04	104.3	C	PC
57	94	1558.7	60.9	1598.4	10.3	1505	151	1594.88	8.55	106.5	C	DL
58	95	1543.9	63.3	1578.25	9.34	1497	152	1577.36	9.19	105.1	C	DL
59	96	1582.3	65	1582.8	17.9	1582	163	1582.7	14.4	102.1	C	DL
60	97	1482.3	59.8	1507.2	10.2	1447	146	1506.6	10.1	104.4	C	MM
61	98	1106.1	52.5	1023.1	14	1273	152	1026.5	13.9	80.5	C	OC
62	99	1257.2	57.1	1169.95	6.18	1410	150	1169.33	6.17	83.0	C	PC
63	101	864.2	46	720.19	6.05	1254	154	721.04	6.05	57.2	C	BR
	100	760.3	43.2	634.3	5.55	1151	165	638.94	5.27	55.4	R	PC
64	102	1567.5	61.2	1584.31	6.81	1545	147	1583.59	6.25	102.6	C	PC
65	103	1544.9	60.4	1555	10.6	1531	148	1554.24	9.49	101.7	C	PC

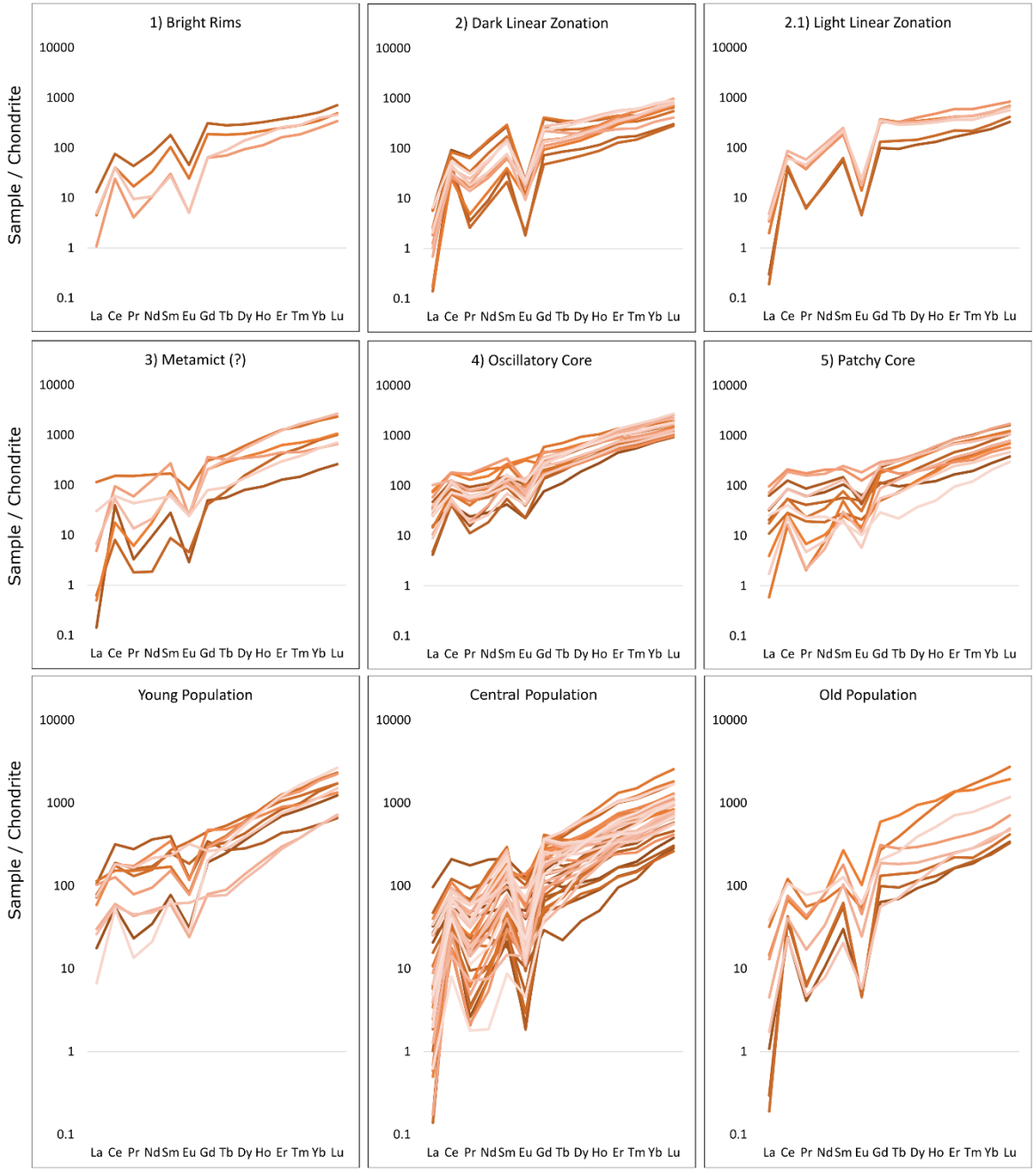

Figure 1: Zircon trace element distribution normalised to C1 chondrite values from McDonough and Sun (1995). Analyses are grouped by textural characteristics (1-5) and spots within three concordant age clusters. All groups have a negative europium anomaly, the anomaly is more pronounced in the central age population and the linearly zoned zircons. There are no distinct geochemical trends identified to discriminate between zircon populations.

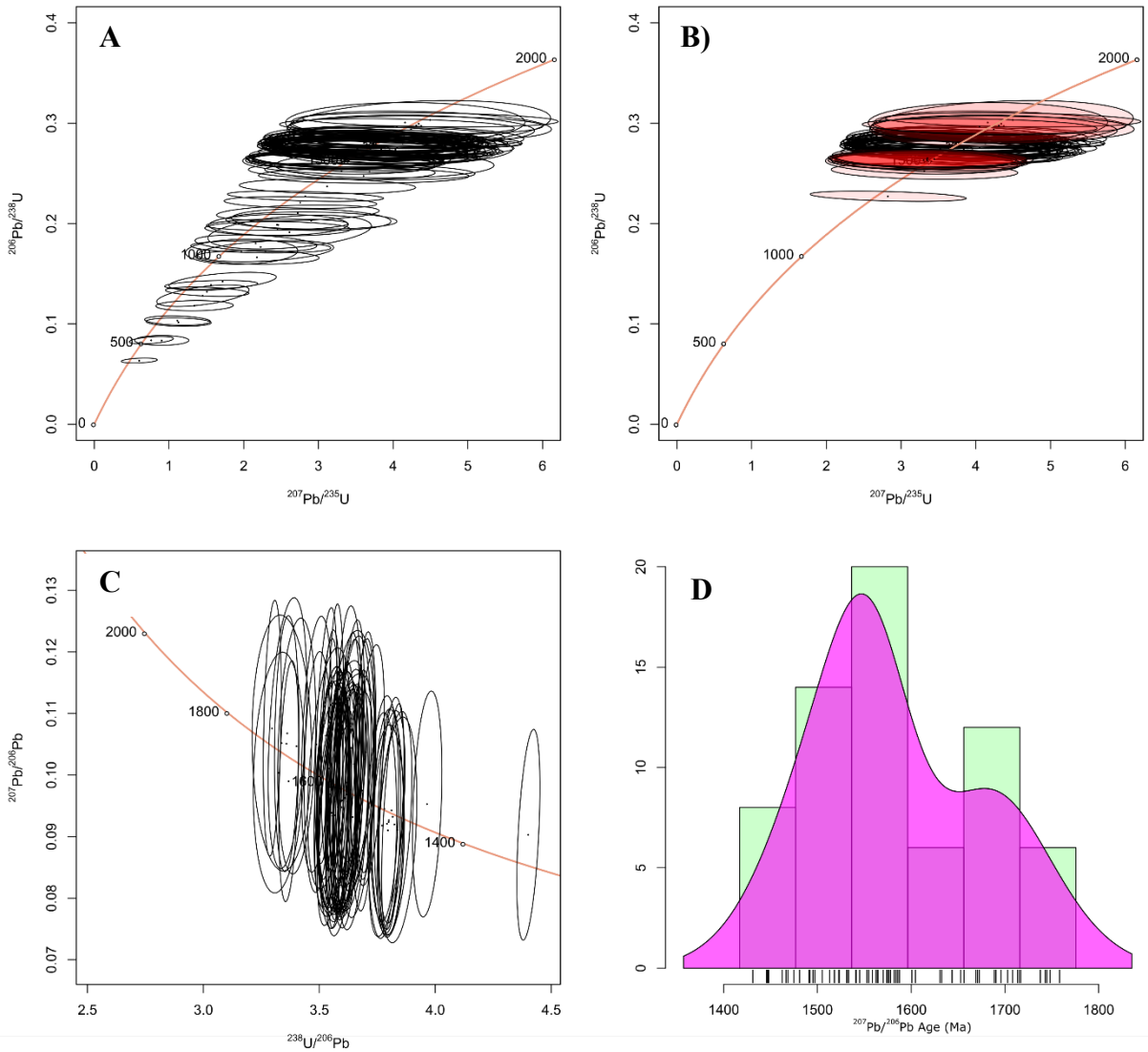

Figure 2: All zircon data (N=94 following bad signal removal). A) Zircon data with no processing plotted on a Wetherill concordia plot, B) data showing locations of old and young clusters, C) All zircon data plotted on a Tera-Wasserberg plot which better shows the separation of the three proposed groups, D) $^{207}Pb/^{206}Pb$ KDE plot of ±10% concordant data points (N=66), the $^{207}Pb/^{206}Pb$ KDE plot was not used in the main text as the chronometric power of $^{207}Pb/^{206}Pb$ in comparison to $^{206}Pb/^{238}Pb$ changes at 1500 Ma (Spencer *et al.* 2016) where the youngest concordant cluster appears to be.

Method for attempting to Identify lead loss trends from geochemically similar populations

Discordant analyses were compared to the maximum and minimum values of elemental concentrations, and various discriminating elemental ratios (U/Th, Gd/Yb, Eu*, Ce*, Total REE, $(Pr/Yb)_N$, $(Sm/La)_N$, and La/Y) to generate a large number of comparisons of similarity for each analysis past just trace and major element concentrations. The total number of times each discordant analysis fell within the compositional range of one of the three proposed concordant populations a point of similarity was counted. The sum of all points of similarity of each discordant analysis was used to compare the total similarity of the discordant point to each individual age group. By sorting discordant analyses by their similarity to the different populations it was possible to identify points which were within 25%, 50% and 75% similarity to the compositional range of the concordant group. Numerous points were within 75% similarity of all populations, for instance point 57 was within 75% similarity to the youngest population, 50% similarity to the oldest population, and 25% similarity to the middle population, in this case the point was allocated to the middle population. Points that were captured by the same similarity bracket in two or three populations were removed as their origin was indistinguishable, points that fell outside of the 75% similarity of any population were also removed. Using this method, a total of 18 of the 28 analyses were able to be attributed to one of the populations. Ten discordant points were identified as likely to have come from the youngest population, five points from the middle population, and three points from the oldest population (Table 4). However, theoretically the lead loss trends should converge on a similar lower intercept, the youngest and oldest ages are still ~30 Ma apart which suggests this approach is not robust.

Table 4: Table of discordant analyses (spot number) filtered by total similarity to each concordant age population.

Similarity	Youngest	Central	Oldest
75%	11, 13	44	3
50%	16, 33, 42, 48, 58	46, 64, 68	57, 80
25%	91, 100, 101	99	

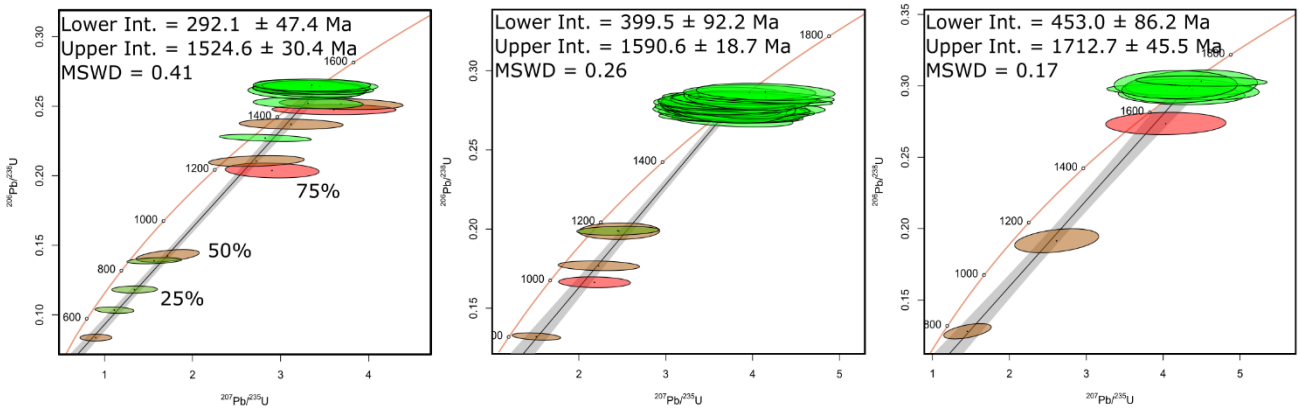

Figure 3: Discordant analyses plotted with their most likely original concordant population prior to isotopic disturbance based on compositional similarity.